THESIS FOR THE DEGREE OF DOCTOR OF PHILOSOPHY

# Microstructural investigation of CVD TiAlN, TiN and WN coatings

REN QIU

Department of Physics

CHALMERS UNIVERSITY OF TECHNOLOGY

Gothenburg, Sweden 2021

Microstructural investigation of CVD TiAlN, TiN and WN coatings
REN QIU

Department of Physics
Chalmers University of Technology
SE-412 96 Gothenburg
Sweden
Telephone + 46 (0)31 772 10 00

Cover:

Scanning electron microscopy (SEM) and electron backscattered diffraction (EBSD) are used to explore the rotational growth of TiAlN grown by chemical vapour deposition (CVD). Top left is a plan view SEM micrograph of a TiAlN coating. Top middle is an EBSD misorientation angle map on the plan view section of a TiAlN grain (red – high misorientation, blue – low misorientation). Top right is the EBSD map of misorientation rotation axes. Bottom left is a schematic illustration of the 3D geometry of a TiAlN grain, while the figure at the bottom middle and right show the 111 pole figures of the same grain.

**Microstructural investigation of CVD TiAlN, TiN and WN coatings**

Ren Qiu
Department of Physics
Chalmers University of Technology

**Abstract**

High speed machining of workpiece materials puts extreme thermal and pressure loads onto the cutting tool inserts, which thus must possess both high hardness and good toughness. Nowadays, most cutting tools are made of cemented carbide substrates that are coated with wear-resistant coatings. Chemical vapour deposition (CVD) is a widely used industrial method for producing the wear-resistant coatings, and has advantages like conformal coverage of irregular shapes and high purity of the deposited materials. However, CVD is a complex process and the coating growth is therefore not fully understood.

This thesis focuses on examining topics of relevance to increase the understanding of hard nitride coatings synthesized by CVD. The main research methods are analytical transmission and scanning electron microscopy (TEM and SEM), with complementary X-ray diffraction (XRD), atom probe tomography (APT) and simulations. Three types of CVD coatings were studied in this work: TiAlN coatings, TiN coatings and WN coatings.

The work on TiAlN coatings: (i) First, the growth facets and texture were revealed. (ii) Second, an effect of precursor gas flow on the growth of the coating was studied, including the correlation between the formation of a nanolamella structure and the rotating precursor gas supply, and a microstructural inhomogeneity relevant to the varying gas environment. (iii) In addition, the full chemical composition of the TiAlN coating was studied via APT and electron microscopy. (iv) Finally, an intra-grain misorientation that forms in TiAlN during the CVD growth, and the formation of relevant dislocations, was studied. The work on TiN coatings: (i) The microstructure of the CVD TiN coatings deposited on a CoCrFeNi multi-principal elemental alloy (MPEA) substrate was studied, and (ii) the etching effect of the corrosive gas environment on the MPEA substrate was evaluated. The work on WN coatings: The microstructure and grain morphology of WN deposited on a (0001) sapphire substrate, especially the influence of deposition temperature on the microstructures, were studied.

In conclusion, the results presented in this thesis provide insights into the detailed microstructures of TiAlN, TiN and WN coatings, which will increase the understanding of the growth mechanisms for these CVD coatings.


**Keywords:** CVD, TEM, SEM, XEDS, EBSD, APT, coating growth, TiAlN, TiN, WN

# List of Appended Papers

This thesis is based on the work presented in the following six appended papers:

**Paper I**

**Ren Qiu**, Olof Bäcke, Dirk Stiens, Wiebke Janssen, Johannes Kümmel, Thorsten Manns, Hans-Olof Andrén, Mats Halvarsson

CVD TiAlN coatings with tunable nanolamella architectures.

*Surface & Coatings Technology 413 (2021) 127076.*

**Paper II**

**Ren Qiu**, Axel Forslund, Olof Bäcke, Mohammad Sattari, Anand. H. S. Iyer, Wiebke Janssen, Thorsten Manns, Johannes Kümmel, Andrei Ruban, Dirk Stiens, Hans-Olof Andrén, Mats Halvarsson

Effects of gas flow on detailed microstructure inhomogeneities in LPCVD TiAlN nanolamella coatings.

*Materialia 9 (2020) 100546.*

**Paper III**

**Ren Qiu**, Hisham Aboulfadl, Olof Bäcke, Dirk Stiens, Hans-Olof Andrén, Mats Halvarsson

Atom probe tomography investigation of 3D nanoscale compositional variations in CVD TiAlN nanolamella coatings.

*In manuscript.*

**Paper IV**

**Ren Qiu**, Olof Bäcke, Dirk Stiens, Hans-Olof Andrén, Mats Halvarsson

Grain rotation during growth of CVD TiAlN.

*In manuscript.*

**Paper V**

Katalin Böör, **Ren Qiu**, Axel Forslund, Olof Bäcke, Henrik Larsson, Erik Lindahl, Mats Halvarsson, Mats Boman, Linus von Fieandt

Chemical vapor deposition of TiN on a CoCrFeNi multi-principal element alloy substrate.

*Surface & Coatings Technology 393 (2020) 125778.*

**Paper VI**

Johan G. Hulkko, Katalin Böőr, **Ren Qiu**, Olof Bäcke, Mats Boman, Mats Halvarsson, Erik Lindahl

Kinetics of the low-pressure chemical vapour deposited tungsten nitride process using tungsten hexafluoride and ammonia precursors.

*Under review of Journal of Vacuum Science and Technology.*

## Statement of Contribution

My contribution to the papers listed above:

**In paper I**: As the principal author, I prepared the samples, performed the microscopy experiments, analyzed results, and wrote the paper under the supervision of my advisors.

**In paper II**: As the principal author, I prepared the samples, performed the microscopy experiments, analyzed results, and wrote the paper under the supervision of my advisors.

**In paper III**: As the principal author, I performed the microscopy experiments, prepared samples for atom probe analysis, analyzed results together with my co-authors, and wrote the paper with my co-authors under the supervision of my advisors.

**In paper IV**: As the principal author, I planned the study, performed the sample preparation, microscopy experiments, result analysis, and wrote the paper under the supervision of my advisors.

**In paper V**: As the second author, I prepared the samples for the microscopy study, performed microscopy experiments, analyzed results and wrote the experimental methods and results of the electron microscopy and the corresponding discussions in the paper together with my co-authors.

**In paper VI**: As the third author, I prepared the samples for the microscopy study, performed microscopy experiments, analyzed results and wrote the experimental methods and results of the electron microscopy and the corresponding discussions in the paper together with my co-authors.

# Preface

The work presented in this thesis was performed at the Division of Microstructure Physics, Department of Physics, Chalmers University of Technology, Sweden, collaborating with Uppsala University, the Royal Institute of Technology, Sandvik Coromant and Walter AG, during the period 2017-2021. The work was performed under the supervision of Prof. Mats Halvarsson. This research was funded by the Swedish Foundation for Strategic Research (SSF program *CVD 2.0*, contract RMA15-0048) and Walter AG.

<div align="right">

Gothenburg, 16th August 2021
Ren Qiu

</div>

*Patience is a virtue*

耐心是一种美德

x

# List of Acronyms

| | |
|---|---|
| AE | Auger Electrons |
| APCVD | Atmospheric Pressure Chemical Vapour Deposition |
| APT | Atom Probe Tomography |
| BF | Bright Field |
| CBED | Convergent Beam Electron Diffraction |
| CFD | Computational Fluid Dynamics |
| CVD | Chemical Vapour Deposition |
| DF | Dark Field |
| DFT | Density Functional Theory |
| EBSD | Electron Backscattered Diffraction |
| EELS | Electron Energy Loss Spectroscopy |
| FCC | Face Centered Cubic |
| FEG | Field Emission Gun |
| FFT | Fast Fourier Transform |
| FIB | Focused Ion Beam |
| HAADF | High Angle Annular Dark Field |
| HRSTEM | High Resolution Scanning Transmission Electron Microscopy |
| LACVD | Laser Assisted Chemical Vapour Deposition |
| LAGB | Low Angle Grain Boundary |
| LPCVD | Low Pressure Chemical Vapour Deposition |
| MBE | Molecular Beam Epitaxy |
| MPEA | Multi-Principal Element Alloy |
| PVD | Physical Vapour Deposition |
| SAED | Selected Area Electron Diffraction |
| SEM | Scanning Electron Microscopy |
| STEM | Scanning Transmission Electron Microscopy |
| TACVD | Thermally Activated Chemical Vapour Deposition |
| TEM | Transmission Electron Microscopy |
| TKD | Transmission Kikuchi Diffraction |
| XEDS | X-Ray Energy Dispersive Spectrometry |
| XRD | X-Ray Diffraction |

# Table of Contents

# 1 Introduction

This thesis is mainly concerned with topics of relevance for developing the understanding of the microstructures of wear-resistant (Ti, Al)N (denoted 'TiAlN'), TiN and WN coatings produced by chemical vapour deposition (CVD). These coatings have been widely used to increase the wear resistance of cemented carbide tools in the cutting tool industry. However, much research remains to fully understand the growth mechanism and microstructural details of these CVD coatings.

## 1.1 Background of cutting tool and wear-resistant coating materials

High-speed metal machining generates extreme pressures and thermal loads, and thus requires cutting tool materials with both good hardness and fracture toughness [1]. Typical hard materials used in cutting tools are illustrated in Figure 1.1. It is clear that the best hardness and the best toughness cannot be obtained simultaneously. Nowadays cutting tool inserts are often made of cemented carbides (WC-Co based hard materials), to obtain a good cutting performance [2].
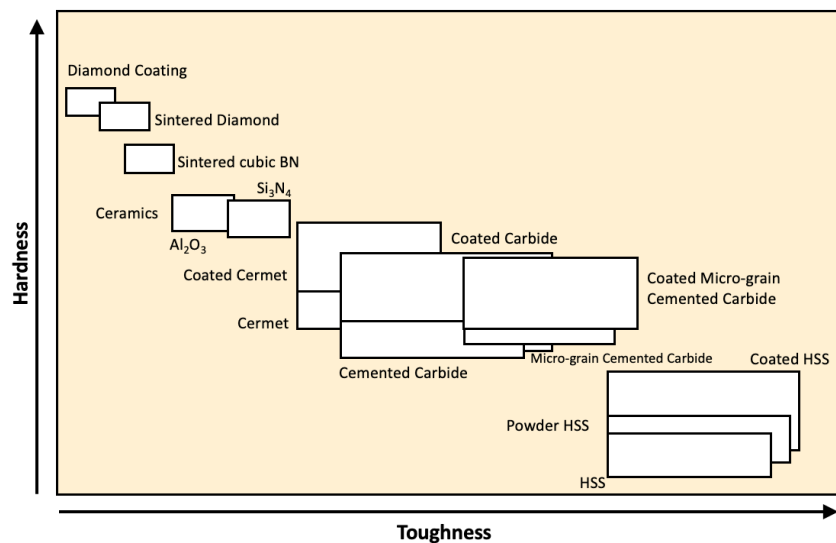


Figure 1.1. Hardness and toughness of typical cutting tool materials. Cermet and HSS denoted in the figure are 'ceramic metal' and 'high speed steels', respectively. Reproduced from [3].

To further improve the cutting performance, the cutting tools are usually coated with thin wear-resistant coatings with higher hardness than the cemented carbide. Depending on the large variety of workpiece materials to be machined, and the corresponding different cutting conditions, a wide range of coating materials has been developed since the 1970's. The wear-resistant coating directly contacts the workpiece materials and is subjected to

extreme machining conditions. Thus, the wear-resistant coatings must exhibit superior properties, such as excellent hot hardness (hardness at high temperatures), oxidation resistance, adhesion to the substrate material and chemical stability. The hardness is one of the most essential properties of coatings that influences the cutting performance. Hardness values of typical coating materials are presented in Figure 1.2. Diamond coatings exhibit the highest hardness [4]. However, the application of CVD diamond coatings is limited by their inferior adhesion to the cemented carbide substrate. This is caused by the significant residual stress formed during the CVD process [5]. In addition, the wear performance of diamond coatings is influenced by dissolution of carbon from the coating into workpiece materials such as steels. Therefore, the most frequently used hard CVD coating materials are $Al_2O_3$, TiN, TiAlN, TiCN and c-BN [6–9].
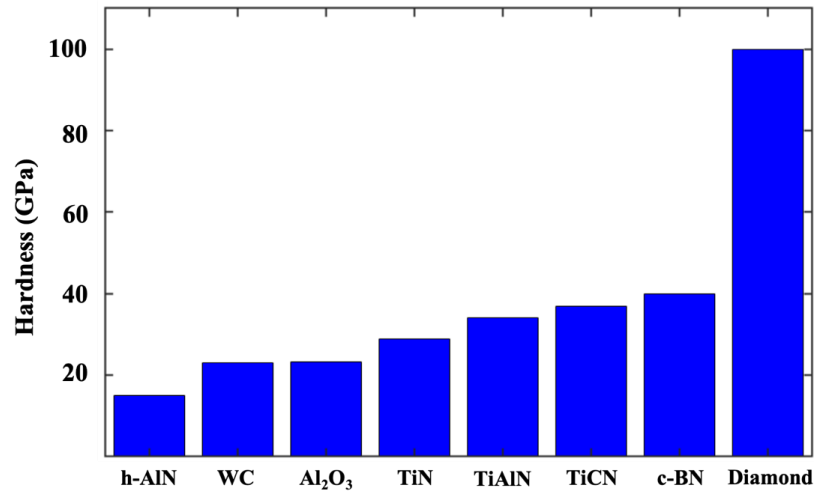


Figure 1.2. Hardness of various coating materials. Values for hexagonal AlN (h-AlN) [10,11], WC [12], sapphire ($\alpha$-$Al_2O_3$) [13], TiN [14,15], TiAlN [14,15], TiCN [8], cubic BN [16], and diamond [4] coatings are shown.

The mechanical performance can often be improved by using textured coatings or designing the architecture of the coating, as in multi-layered coatings [17–19]. In the appended Papers I, II, III and IV, the study is focused on TiAlN coatings. In Paper V the study is focused on TiN coatings, while Paper VI is mainly concerned with WN coatings.

## 1.2   Microstructural investigations

The research presented in this thesis is mainly concerned with understanding the growth of the CVD coating materials. Detailed studies of the coating microstructures have therefore been performed. To study the phase content and the texture of coatings, X-ray

diffraction (XRD) was used. Scanning electron microscopy (SEM) plan-view and cross-sectional imaging was used to reveal the grain morphologies in the CVD coatings. SEM based electron backscattered diffraction (EBSD) and transmission Kikuchi diffraction (TKD) were extensively used to understand grain orientations. Analytical electron microscopy, combining imaging with X-ray energy dispersive spectrometry (XEDS) and electron energy loss spectroscopy (EELS) in (scanning) transmission electron microscopy (STEM/TEM), enabled microstructural investigations with high spatial resolution, providing both crystallographic and chemical information. To study the defects in the coating, especially growth dislocations, TEM bright and dark field (BF/DF) imaging associated with electron diffraction were performed. To determine the chemical composition (especially the N content) of a TiAlN coating with a nanolamella structure in three dimensions (3D), atom probe tomography (APT) was performed. Since the microstructural study was a central part of this work, details of the techniques used and the corresponding applications will be described in the chapters below.

## 1.3   Scope of thesis

This thesis is concerned with hard TiAlN, TiN and WN coatings synthesized by CVD, and the understanding of coating growth through systematic microstructural studies. The following research topics are addressed in this thesis:

- The effect of precursor gas flow on the growth of CVD TiAlN coatings. This includes (i) the correlation between a rotating gas supply and the formation of an internal nanolamella structure (Paper I), and (ii) a compositional and structural inhomogeneity influenced by the spatial variation in the gas environment (Paper II).

- The chemical composition of the TiAlN phases and its 3D variation within the nanolamella structures (Papers I – III).

- The growth of the TiAlN grains, including the geometry of the internal nanolamella structure, the growth facets, and their relationship with the growth orientations and textures (Papers I and IV).

- The capability of a CoCrFeNi multi-principal elemental alloy (MPEA) as a substrate for CVD TiN coatings, including the etching effect of the corrosive gas environment on the substrate and the corresponding coating microstructures (Paper V).

- The morphology and microstructure of WN coatings synthesized by low pressure chemical vapour deposition (LPCVD) on a (0001) sapphire substrate (Paper VI).

This thesis is structured in the following way: Chapter 2 describes basic theories of CVD synthesis of coatings/thin films. Chapter 3 describes materials studied in this work, such as the TiAlN, TiN and WN phases. In Chapter 4, the experimental techniques used in this work are described. In Chapter 5, basic theories of dislocations relevant to coating growth are introduced. Finally, the main results and conclusions are presented in Chapter 6, and an outlook is given in Chapter 7. Part of the work presented in this doctoral thesis has previously been presented in a licentiate thesis by the same author [20].

# 2 Chemical vapour deposition of thin films

The thin films investigated in this work were prepared via CVD. It is, therefore, necessary to introduce the basic principles of CVD in order to study the growth of these coatings.

## 2.1 Basic principles of CVD

CVD is an important technology for synthesizing wear resistant protective thin films on cutting tools with good adhesion [21–30]. CVD has been intensively used to produce various metals, non-metallic element materials, oxides, nitrides and carbides [31]. In CVD synthesis, gaseous precursors, usually metal halides with reducing agents, react at high temperature to form a solid phase. CVD reactions can happen homogeneously in the gas phase and form particles that fall down onto the substrate, which yields inferior coatings with porosity and poor adhesion to the substrate. Ideally, precursors should react heterogeneously at the substrate surface to form coatings with good quality. The undesired homogeneous nucleation in CVD can be avoided by heating the substrate, and choosing reactant species that exhibit strong chemisorption to the substrate and need thermal activation to react [32]. The growth of CVD coatings is governed by thermodynamics that controls the driving forces of the chemical reactions, and by reaction kinetics that determines the coating growth rate.

Most of the CVD synthesis processes involve endothermic chemical reactions that need energy input to be activated. There are several approaches for activating the gaseous reactants and lowering the reaction temperatures. The activation energy can be lowered by exciting the gaseous precursors with a plasma to create reactive intermediate products, called plasma enhanced CVD (PECVD) [33]. The substrate surface is heated locally by a laser beam to activate the surface reaction in laser assisted CVD (LACVD) [34]. LACVD is also applied to stimulate the gaseous precursors to excited states by illuminating with characteristic light wavelengths, which lowers the decomposition energy of reactant chemicals and thus the deposition reaction temperature. Another approach is thermally activated CVD (TACVD), which is implemented by heating the entire chamber (hot wall CVD), heating the substrate (cold wall CVD), or activating the gas phase through a heating filament (hot filament CVD).

The CVD process includes several events happening in sequence (and in parallel) [31,35], as graphically illustrated in Figure 2.1. The gaseous reactant molecules are transported towards the substrate to be deposited by the main gas stream in the reactor. The reactant molecules diffuse through a stagnant layer, which is formed by the gas flowing above the substrate surface [31]. The reactant molecules get adsorbed/dissociated on the substrate surface, where the binding strength influences the mobilities of the molecules on the

surface. Reactant molecules diffuse on the surface to find sites with steps and kinks that form more stable bonds with the molecules. The surface reactions of reactant molecules form a deposited solid phase, where also byproduct molecules are created. These byproducts get desorbed and diffuse from the surface through the stagnant layer, and are transported away from the deposition area by the gaseous flow.
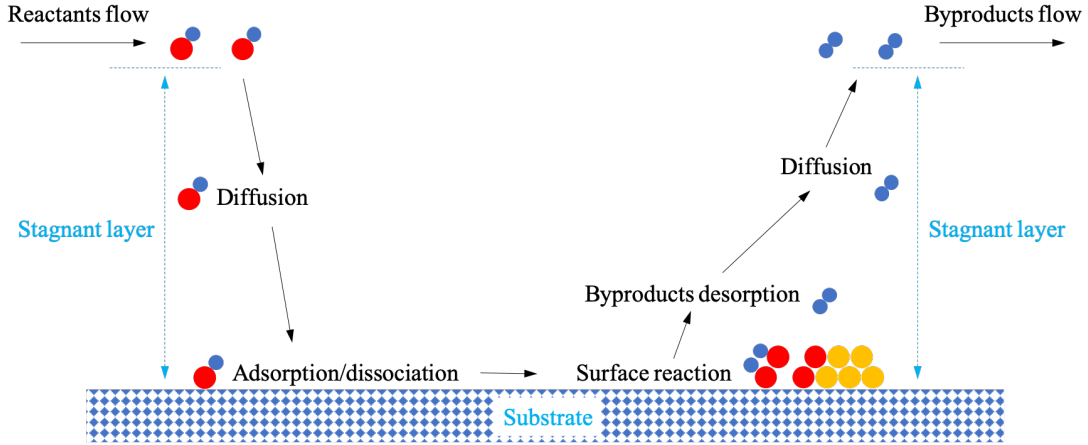


Figure 2.1. Schematics of the sequence of events during a CVD process.

However, stable coating growth is not always obtained due to the complexity of the CVD process. The surface reactions and deposition rates are influenced by several factors, including types of the precursor species, deposition temperature and mass transport rate. To obtain a stable, predictable coating growth, it is therefore essential to understand and control the kinetics of the CVD process.

## 2.2   *Limiting factors of CVD growth rate*

The deposition rate in CVD is mainly controlled by (i) the mass transport of reactants through the stagnant layer by diffusion, and (ii) the surface reaction kinetics of the reactants. The CVD coating growth rate $v$ (ms$^{-1}$) can be analyzed by a reactants diffusion - surface reaction balancing model [36,37], according to:

$$v = \frac{k_S\, h_G}{k_S + h_G} \frac{C_G}{N} \tag{2.1}$$

where $k_s$ is the surface reaction rate (ms$^{-1}$), $h_G$ is the mass transfer coefficient (ms$^{-1}$), $C_G$ is the specie concentration in the gaseous phase in terms of number of atoms (m$^{-3}$), and $N$ is the number of atoms of the species per unit volume in the solid film (m$^{-3}$).

If the surface reaction rate is much lower than the mass transport rate ($ks \ll h_G$), the CVD reaction is within the surface reaction control regime, and the deposition rate is mainly limited by the surface reaction rate $k_s$. Equation (2.1) becomes:

$$v_s = k_s \frac{C_G}{N} \qquad (2.2)$$

If the surface reaction rate is much higher than the mass transport rate ($ks \gg h_G$), the CVD reaction is within the mass transport control regime, and the deposition rate is mainly limited by the mass transfer coefficient $h_G$. Equation (2.1) becomes:

$$v_G = h_G \frac{C_G}{N} \qquad (2.3)$$

Equation (2.3) can be reformulated according to fluid dynamic theory [38], to be:

$$v_G \propto \frac{C_G}{N} D_G (u\rho)^{1/2} \qquad (2.4)$$

where $D_G$ (m$^2$s$^{-1}$) is the diffusivity of the gas molecules, $u$ is the gas flow speed (ms$^{-1}$), and $\rho$ is the gas density (kgm$^{-3}$). According to Equation (2.4), the coating growth rate of the mass transport-controlled deposition increases with higher precursor diffusivity, higher gas density and faster gas flow.


## 2.3 Low pressure CVD and gas flow

Low pressure CVD (LPCVD) is a commonly used CVD technique that applies low pressures (tens to thousands of Pa) of the gaseous precursors, which is much lower compared to that (1 atm = 101325 Pa) of the atmospheric pressure CVD (APCVD). LPCVD has been widely used in the semiconductor industry for deposition of a wide range of thin film materials, including polycrystalline silicon, oxides, and nitrides [39–41].

In the APCVD process, the surface reaction rate is usually much lower than that of the mass transport, and it is therefore difficult for the precursor molecules to reach equilibrium for the reactions on the substrate. In LPCVD, the pressure is lowered to reduce the mass transport rate of the reacting chemicals onto the substrate surface. According to Equation (2.4), the rate of CVD deposition limited by the mass transport decreases with lower gas flow velocity and lower density of gaseous precursors. A low-pressure gaseous environment in LPCVD thus provides lower gas densities and therefore reduces the mass transport through stagnant layer diffusion. The suppressed mass

transport (and reduced coverage of reactant molecules on the substrate surface) in LPCVD boosts the surface reaction kinetic zone, and enables a slower surface reaction (than that of the APCVD) of the precursor molecules that are very reactive. Another advantage of LPCVD is that it helps to deposit coatings with good uniformity and homogeneity. However, a disadvantage of LPCVD can be lower coating growth rates compared to that of APCVD.

The LPCVD synthesis of TiAlN coatings is very sensitive to mass transport and the local gas flow rate. TiAlN coatings are commonly deposited in industrial scale CVD reactors with a cylindrical geometry and a rotational gas supply of precursors [42]. In this type of CVD set-up, there are two kinds of gas flow variations: (i) a temporal variation of local gas environment in the vicinity of each insert, correlated to the precursor gas supply rotating with a certain frequency; (ii) a spatial variation of local gas flow around each insert, and between inserts placed at different locations in the reaction zone of the CVD reactor.

As mentioned above, the growth rate of the coatings is mainly limited by the mass transport of the precursor molecules (from the gas stream through the stagnant layer to the substrate), and/or the reaction kinetics on the substrate surface. It is worth noting that a difference exists between the surface reaction kinetics for the incorporation of the Ti and Al atoms in the LPCVD synthesis of TiAlN coatings. It has been reported that the CVD reaction for the titanium chlorides generally requires a temperature around 800 °C, but the temperature needed for the surface reaction of the aluminium chlorides is usually around 1000 °C and sometimes even above 1400 °C [43,44]. The LPCVD synthesis of the TiAlN coatings is usually performed at relatively low deposition temperatures (650 - 800 °C) [42]. The low deposition temperature limits the surface reaction rate of the aluminium chlorides more than that of the titanium chlorides. Thus, the process of incorporating Ti atoms into the TiAlN phase is in the mass transport controlled regime, while the incorporation of Al atoms into the TiAlN phase is in the surface kinetics controlled regime. A (temporal and spatial) varying gas flow would cause a (temporal and spatial) variation of the mass transport, which influences the incorporation of the Ti atoms relative to that of the Al atoms, and thus changes the chemical composition and the coating microstructure.

## 2.4   Competitive growth of polycrystalline film: texture and facets

TiAlN, TiN and WN coatings grown on cemented carbide substrates by CVD are usually polycrystalline, textured and faceted. A general background of competitive growth of polycrystalline materials, especially the formation of texture, growth facets of the grains, and their correlation, is given and discussed below.

Thin film formation on a substrate comprises a number of steps, including nucleation and growth of seeds (into islands), film formation by islands coalescence, and thickening of the film [45]. Crystalline thin films sometimes exhibit texture. It means that there is a preferred crystallographic orientation for the coating material relative to the substrate. The causes for the formation of a growth texture mainly include [46]:

- **Preferred orientation for the initial nucleation with respect to the substrate.** For the epitaxial growth on a single crystal substrate, the crystal seeds preferably nucleate with a particular orientation. This is common for, e.g. the growth of single crystal thin films in semiconductor industries [47,48]. For polycrystalline substrates that have a certain texture, the deposited film would grow with a preferred crystallographic orientation influenced the substrate texture. This also happens in the synthesis of multilayered coatings [6,49,50].

- **Preferred direction for the film thickening.** Even for seeds nucleating with random orientations on the substrate, a so-called competitive growth (or evolutionary selection) process could still cause a preferred growth texture during the film thickening [46]. During the competitive growth, grains with crystallographic orientations that grow faster vertically (parallel to the substrate surface normal) are more likely to survive. This is common for deposition of polycrystalline films with fibre textures. Fibre texture means that a particular crystallographic orientation of the film grains is preferred to be perpendicular to the substrate surface, but the crystallographic orientations are random parallel to the substrate surface. A van der Drift model was proposed to explain the competitive growth, by correlating the faceted growth with the fibre textures [46].

Faceted growth often happens in CVD of polycrystalline materials where a grain boundary forms when facets of neighbouring grains meet [45,46,51]. For a faceted grain it is worth noting that the growth rate of corners (and edges) between neighbouring facets is often higher than that of the facets [51,52]. Therefore, the growth rate of a grain with a corner (or edge) pointing along the coating growth direction (parallel to the substrate surface normal) is higher than that of its neighbouring grains. This faster growing grain would then win the growth competition, and become columnar with a certain texture.

# 3 CVD coating materials

The coating materials studied in this thesis include the cubic structures of the TiAlN, TiN and WN phases, and the AlN phase with a hexagonal structure (h-AlN). In this chapter, basic information, such as crystal structures, coating morphologies and applications of these materials synthesized by CVD will be introduced.

## 3.1 *Titanium nitride*

TiN is a refractory material with rock salt crystal structure (B1), and contains a Ti sublattice and a N sublattice with face centered cubic (FCC) structure, as shown in Figure 3.1 (a). The lattice parameter of TiN is 4.242 Å (PDF 00-038-1420). TiN has been widely used in various applications, such as diffusion barriers [53], corrosion protective films [7] and wear-resistant coatings [54], due to its superior hardness, thermal stability, corrosion and wear resistance. TiN coatings can be synthesized by both physical vapour deposition (PVD) [55,56] and CVD [57].
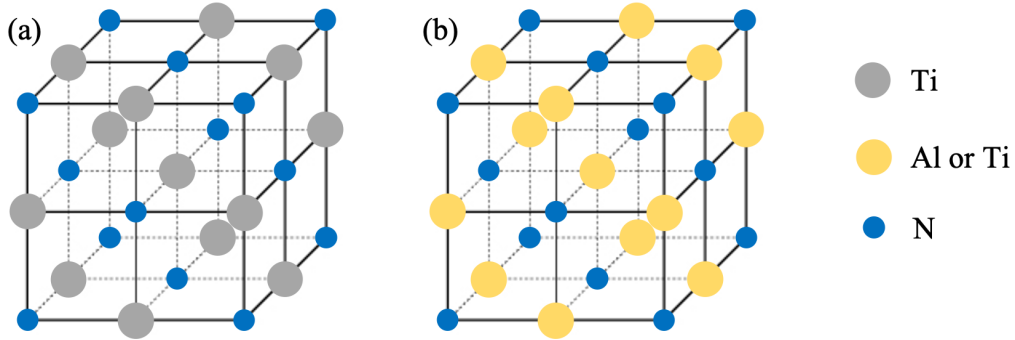


Figure 3.1. Schematics of the crystal structures of TiN and TiAlN. (a) TiN where Ti and N atoms form two FCC sublattices; (b) TiAlN where Al atoms partly replace the Ti atoms in the Ti FCC sublattice in the TiN crystal structure. The Al content is represented by the occupancy $x$ in $Ti_{1-x}Al_xN$. Vacancies of Ti, Al or N are not shown.

Previous studies have shown that the CVD TiN coatings can be deposited with good adhesion on different substrate materials, such as alumina, Si and Co [6,57,58]. For CVD synthesis of TiAlN coatings, a TiN coating is usually deposited as an intermediate layer between the cemented carbide substrate and the TiAlN coating (see Figure 3.3 in Section 3.2). This is done because the CVD TiN films have good adhesion to both the cemented carbide substrate and the TiAlN coating. It is, however, worth noting that TiN coatings exhibit less prominent oxidation resistance. Oxidation starts from 550 °C, which is much lower than common cutting operation temperatures [14].

## 3.2 Titanium aluminium nitride

The $Ti_{1-x}Al_xN$ (TiAlN) phase exhibits a rock salt (B1) structure and thus has an FCC lattice. As shown in Figure 3.1 (b), the ternary alloy $Ti_{1-x}Al_xN$ (TiAlN) forms by randomly replacing Ti atoms in the TiN crystal with Al atoms ($x$ represents the occupancy of Al atoms on the metal lattice), and can be seen as a solid solution of TiN and cubic AlN (with B1 structure). The lattice parameter of TiAlN depends on the Al content, and can be estimated by interpolation according to the lattice parameters of the cubic TiN and AlN phases. As mentioned in Section 3.1, the lattice parameter of the TiN phase is 4.242 Å. The lattice parameter of the cubic AlN phase is 4.045 Å (PDF - 00-046-1200) [59]. Usually, the lattice parameter can be estimated by the linear interpolation (Vegard's law [60]), and in this way the lattice parameter of the TiAlN phase ($a$) with known Al content (the x value) can be predicted as:

$$a = x \cdot 4.045 \text{ Å} + (1 - x) \cdot 4.242 \text{ Å} \qquad (3.1)$$

However, it is worth noting that a small deviation from the Vegard's law was reported for the lattice parameters of the TiAlN coatings, where a non-linear relationship between the lattice parameter and the Al and Ti contents could be identified [9], although this difference is negligible and does not matter for the XRD analysis used in this work.

The TiAlN phase has been reported to show better mechanical properties and chemical inertness, such as hardness, hot hardness and oxidation resistance, compared to that of the TiN phase, through the increased Al content [14,61].

The TiAlN phase is thermodynamically metastable, and has a miscibility gap (containing spinodal and binodal regions) for a wide range of the Al content [62–64] as shown in Figure 3.2. For compositions within the miscibility gap, the TiAlN phase tends to decompose into TiN (or a Ti-rich phase) and h-AlN. The asymmetric miscibility gap (narrower at higher Al content) of the TiAlN phase implies that phase separation (into Al-rich and Ti-rich phases) tends to happen at a higher Al content [62–64]. In addition, the miscibility gap gets narrower at higher temperatures. Thus, the TiAlN phase would also decompose if the material is heat treated at a high enough temperature for a sufficiently long time [65–69].

Both PVD and CVD methods can be used for synthesis of TiAlN coatings. PVD was originally used, yielding restricted Al contents in the cubic TiAlN phase up to x ~ 0.65 [70,71]. A higher Al content in PVD TiAlN coatings results in the formation of the h-AlN phase. However, in recent years cubic TiAlN coatings with higher Al contents (x ≥ 0.9) have been synthesized by LPCVD [61]. The LPCVD TiAlN coatings have higher (hot) hardness and better oxidation resistance than the PVD TiAlN coatings due to the

higher Al content, and also show a good thermal stability where the cubic phase remains stable after annealing for one hour at temperatures up to ~ 1000 °C[61,72].
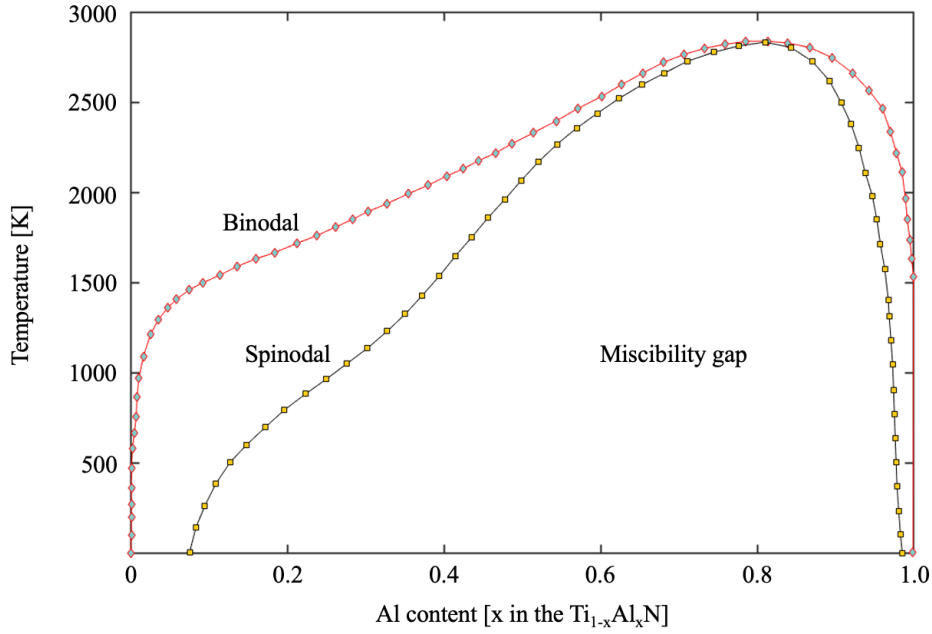


Figure 3.2. The simulated phase diagram of the TiAlN phase. Data taken from [62,63].

A typical LPCVD TiAlN coating on a cemented carbide cutting tool insert is shown in Figure 3.3. The TiAlN grains have a pyramidal surface shape with three-fold rotational symmetry, as shown by the plan view SEM micrograph in Figure 3.3 (a). Figure 3.3 (b) shows the cross-section of one of the corners of the insert, which is coated by TiN/TiAlN coatings with an even thickness (around 6 $\mu$m). The thin (less than 1 $\mu$m) TiN film serves as a bonding film to increase the adhesion between the cemented carbide substrate and the TiAlN coating. Figure 3.3 (c) shows the microstructures of the TiN/TiAlN coatings in cross-section. The TiAlN coating consists of columnar grains. Figure 3.3 (d) is an SEM in-lens secondary electron (SE) micrograph and shows the internal structure of the TiAlN grains, where a nanolamella structure is seen.
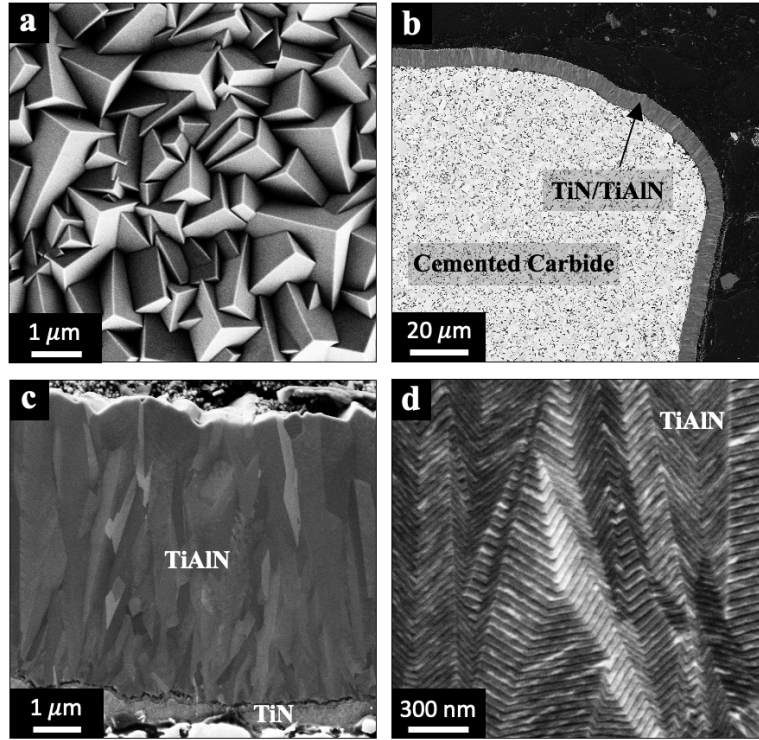
Figure 3.3. Plan view and cross-sectional SEM micrographs of a cemented carbide cutting tool insert coated with TiN and TiAlN coatings. (a) SEM SE image of the pyramidal shape surface morphology of a CVD TiAlN coating. (b) SE image of the cross-section of one of the corners of the coated cutting tool insert. (c) SE cross-section image of the columnar structure of the coating. (d) In-lens SE micrograph of the internal lamella structure of the coating grains.

## 3.3   *Aluminium nitride*

h-AlN is a typical III-V semiconductor material with a wurtzite (B4) structure ($a$ = 3.12 Å, and $c$ = 4.98 Å). h-AlN has a wide direct band gap of 6 eV [73]. With such a large band gap, h-AlN has been intensively used in opto-electronic devices, such as light emitting diodes, laser diodes and photodetectors. The h-AlN is also used in high-temperature electronic devices because of its high melting temperature [74]. The h-AlN is also widely used in electronic industries for semiconductor packages due to its high thermal conductivity at elevated temperature and a good thermal expansion match with silicon [75].

The h-AlN phase was found co-growing with the cubic TiAlN phase during the LPCVD synthesis process, which is believed to influence the mechanical performance of the hard coating. The h-AlN has a high hardness (~ 15 GPa) [10,11], which is however still much lower than that of the cubic TiAlN (~ 30 GPa) [61]. As mentioned above, the metastable TiAlN phase tends to decompose and form the h-AlN phase which thus influences the mechanical performance of the coating, usually in a negative way. In PVD TiAlN

14

coatings, the formation of the h-AlN phase (when x > 0.65 in $Ti_{1-x}Al_xN$) has been reported. A mixture of TiAlN and a noticeable amount of h-AlN was found to result in the disappearance of the TiAlN columnar grain morphology [70,76].

## 3.4 Tungsten nitride

Among the $WN_x$ (WN) phases that have been reported [77–81], it is mainly the cubic $\beta$-$WN_x$ that is of interest in this work. The cubic $\beta$-$WN_x$ phase has a rock salt structure (XRD: JCPDF 00-025-1257), and the lattice parameter varies from 4.11 Å to 4.30 Å [77,82–85]. The atomic ratio between the W and N atoms in cubic $\beta$-WN was believed to be 2:1 (with a chemical formular $\beta$-$W_2N$), where the sites in the W sublattice are fully occupied while the 50% of the N sites are vacant [77,80,81]. However, Mehl, *et al.* proposed, by theoretical simulation, that a rock salt $\beta$-WN phase with a chemical content as $W_2N$ is not stable. The $\beta$-WN phase is only stable when the W sublattice has vacancies [86]. It is worth noting that a wide range of chemical compositions of the WN phases ($x$ = 0.5 ~ 2.0 in $WN_x$) have been reported, and $x$ in the rock salt $\beta$-$WN_x$ structure can be changed between 0.83 and 1.21 through PVD [77–81].
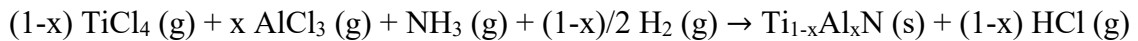
# 4 Experimental methods

The main part of the work presented in this thesis is concerned with electron microscopy, which is a powerful set of techniques for materials characterization. It provides the possibility for combining high resolution imaging with crystallographic and chemical information. In this research, both SEM and TEM have been used for the microstructure investigations. Basic theories of electron microscopy are discussed in this chapter. APT has been used for 3D analysis of the chemical composition of the nanolamella architectured TiAlN phase, and thus the basic theories of APT are also introduced in this chapter. In addition, XRD has been used to analyze phase contents and coating textures. A brief introduction to XRD and some used modelling techniques are included as well. Apart from the microstructural characterization methods, the CVD experiments for coating synthesis carried out at Walter AG and Uppsala University are described.

## 4.1 CVD experiments for coating synthesis

For the synthesis of the TiAlN coatings studied in Papers I – IV, the deposition was performed in an industrial scale hot wall CVD equipment heated by a hood-type furnace. This CVD reactor has a cylindrical geometry and a reaction zone (where the substrates are placed) that is 750 mm in height and 275 mm in diameter. The precursors and carrier gases are supplied through an inlet pipe (at the centre of the reaction zone) that can rotate with different frequencies. The substrate material was cemented carbide (94 wt.% WC and 6 wt.% Co). Before depositing the TiAlN coating, the substrates were pre-coated with a thin TiN layer, which was deposited at 850 °C and 150 mbar, with $TiCl_4$, $N_2$ and $H_2$ as precursors, according to the reaction:

$$TiCl_4 \text{ (g)} + 1/2 \, N_2 \text{ (g)} + 2 \, H_2 \text{ (g)} \rightarrow TiN \text{ (s)} + 4 \, HCl \text{ (g)}$$
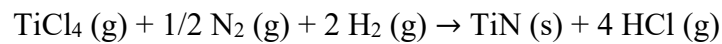
where stoichiometry between the Ti and the N atoms is assumed. The TiAlN coatings were grown on the TiN pre-coated cemented carbide substrates. As discussed in Section 3.2, the TiAlN phase is metastable and may decompose at elevating temperatures. The CVD temperature for synthesis of the TiAlN phase was, thus, low and in the range from 650 to 800 °C. At a low temperature, the surface reaction rate of the relatively non-reactive precursor molecules ($N_2$) is low. Therefore, in order to improve the surface kinetics limited deposition rate, more reactive precursors, like $NH_3$, were used in the LPCVD synthesis of the TiAlN. The corresponding chemical reaction is:

$$(1\text{-}x) \, TiCl_4 \text{ (g)} + x \, AlCl_3 \text{ (g)} + NH_3 \text{ (g)} + (1\text{-}x)/2 \, H_2 \text{ (g)} \rightarrow Ti_{1\text{-}x}Al_xN \text{ (s)} + (1\text{-}x) \, HCl \text{ (g)}$$

where stoichiometry between the metal (Ti and Al) and N atoms is assumed. A low deposition pressure between 5 and 25 mbar was used. After the CVD reaction, the carrier gases and by-products were evacuated by the vacuum pump system through the gas outlets at the periphery of the reactor. For more details of the film synthesis, see Papers I and II, and patent [42].

The TiN coating discussed in Paper V was deposited on a CoCrFeNi multi-principal element alloy (MPEA) substrate. The substrate materials were prepared through arc melting of pellets of Co, Ni, Fe, and Cr, and was remelted several times for homogenization. The arc melted piece was cut into discs that were heat treated at 1200 °C under flowing Ar for 36 h in order to obtain equiaxial grains [87,88]. The substrate material was polished on SiC paper and by diamond paste slurries before the deposition. The polished substrates were coated in an industrial hot wall CVD reactor at different temperatures ranging from 850 °C to 900 °C, and at a pressure of 40000 Pa. The gas precursors used in the deposition were $TiCl_4$, $H_2$, and $N_2$, and the CVD reaction is identical to that for the formation of the TiN inner layer of the TiAlN coatings.

The WN coatings discussed in Paper VI were deposited in a lab-scale horizontal tube hot-wall CVD reactor. Single crystal $\alpha$-$Al_2O_3$ wafers with a flat basal plane (0001) surface was used as substrate material. The gaseous precursors were $WF_6$, $NH_3$, and $H_2$, and the CVD reaction that results in the WN coatings is [89]:

$$2\ WF_6\ (g) + (6\text{-}3/2x)\ H_2\ (g) + x\ NH_3\ (g) \rightarrow W_2N\ (s) + 12\ HF\ (g) + (x\text{-}1)/2\ N_2$$
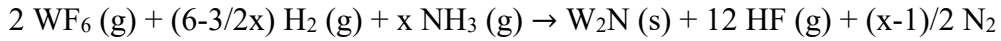
where a non-stoichiometric $\beta$-$W_2N$ phase is assumed to form, as proposed in references [77,80,81]. The deposition was performed with pressures between 3 – 40 Pa, and at temperatures ranging from 300 to 600 °C.

## 4.2   X-ray diffraction

In this thesis work, XRD was used to examine the phase contents and coating textures [90,91]. As schematically illustrated in Figure 4.1, an X-ray source generates an incident beam to illuminate a polycrystalline or powder specimen, and the incident X-rays are diffracted by the crystal structure according to Bragg's law: $\lambda = 2d_{hkl} \sin\theta$, where $d_{hkl}$ is the interplanar distance between (*hkl*) atomic planes, $\lambda$ is the wavelength of the X-rays, and $\theta$ is the Bragg angle.
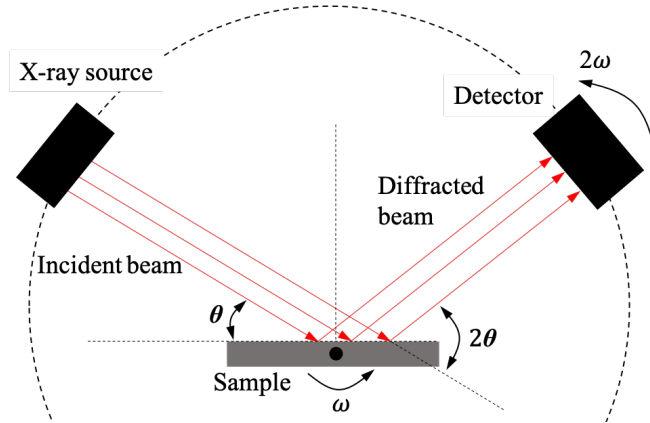
Figure 4.1. Schematic illustration of an X-ray spectrometer set-up for a θ - 2θ scan.

The diffracted beam is detected by an X-ray detector, and the angle between the incident beam and the diffracted beam is $2\theta$. During a $\theta$ - $2\theta$ scan, the sample and the detector rotate with an angular speed of $\omega$ and $2\omega$, respectively, and the intensity $I$ at the detector position is registered. The intensity $I$ as a function of $2\theta$ is then presented as an X-ray diffractogram [90].

Figure 4.2 shows a typical X-ray diffractogram, obtained from a CVD TiAlN coating deposited on a cemented carbide substrate pre-coated with a TiN film. In this X-ray diffractogram, peaks from the substrate phases (WC and $W_6Co_6C$) and the TiN phase (the inner layer) can also be identified. An intense 111 peak and a strong 222 peak can be identified from the TiAlN phase, indicating a strong 111 growth texture of the CVD TiAlN coating.
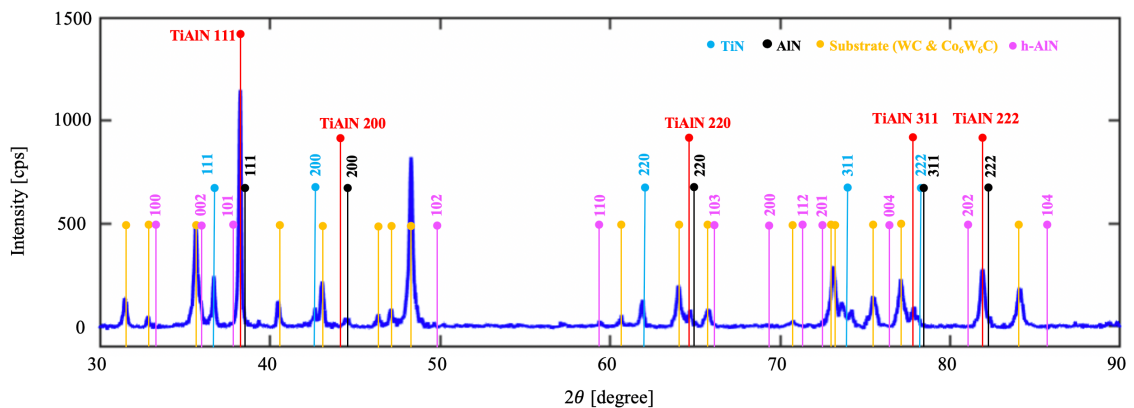


Figure 4.2. X-ray diffractogram from a CVD TiAlN coating deposited on a cemented carbide substrate pre-coated with a TiN layer. The marked phases are (cubic) TiN (PDF 01-074-8388), (cubic) AlN (PDF 00-046-1200), WC (PDF 01-089-2727), and $Co_6W_6C$ (PDF 00-022-0597). Location of peaks from h-AlN (PDF 00-025-1133) are marked for reference.

## 4.3    Scanning electron microscopy

SEM is a widely used electron microscope technique for characterization of the microstructure of materials. In an SEM, electrons are emitted from an electron source, usually a thermionic gun or a field emission gun (FEG). The stream of emitted electrons is accelerated by an anode below the gun, to an energy typically ranging from 2 to 30 keV. The electron beam is then converged by one or multiple electromagnetic condenser lenses and focused into a fine probe. The focused probe on the specimen surface is a demagnified image of the electron source. The convergence angle of the electron probe is determined by the objective aperture. By a beam shifting function using the scanning coils, the focused electron probe scans through a rectangular raster over the sample surface area of interest. The focused electron beam hits the sample surface and interacts with the specimen by elastic and inelastic scattering within a so-called interaction volume. Within the interaction volume, signals are generated, and may travel to the specimen surface, depending on where in the interaction volume the signal is generated. The signals emitted from the surface are detected by various detectors. Typical signals include Auger electrons (AEs), secondary electrons (SEs), backscattered electrons (BSEs) and characteristic X-rays. The detector signals will be processed by a computer that also controls the scanning circuit to control the position of the focused probe.

The interaction volume starts from the sample surface and expands into the sample interior for a certain depth depending on an integral effect of the specific material composition and acceleration voltage. However, the escape depths of signals depend on their mean free paths within the specimen. SEs are generated by the inelastic scattering of the incident electrons, which excites the outer shell electrons of the specimen. SEs exhibit low energies (0 ~ 50 eV) and are easily absorbed within the specimen, which means that the SE signal captured by the detector is usually very localized, emitting from a volume that extends only a few nm below the specimen surface. An SE detector and an in-lens detector positioned within the objective lens collect SEs, yielding micrographs of surface topographic information with high spatial resolution and sharp surface morphology contrast [92]. BSEs are incident electrons scattered by the nuclei of specimen atoms, with higher energies than the SEs. The BSEs are emitted from a larger part of the interaction volume, thus giving a lower spatial resolution compared to the SE signal. BSEs collected by an BSE detector provide image contrast depending on the local average atomic number, since the probability of elastic scattering increases with the atomic number, which means that an area with heavier elements generates more BSEs and yields a brighter contrast than an area with lighter elements.

Upon illumination by the primary electron beam, sufficient energy can be transferred to a core-shell electron that is excited outside the strong field of the nucleus, which is called ionization [93]. Once ionized, the excited atom can decay to the ground state where an outer shell electron fills the core hole, emitting excess energy. This transition energy can either create characteristic X-rays or AEs. These AEs are emitted from a few top layers

of atoms of the specimen surface; however, the signal intensity is too low to be detected by regular SEM detectors. Characteristic X-rays are emitted from a larger part of the interaction volume, and can be collected by a diode-type Si detector to perform XEDS. The SEM XEDS provides both qualitative and quantitative information about the chemical composition of the probed area, but with lower spatial resolution than the electron signals. The XEDS analysis is mainly performed in this thesis during STEM mode, and more details of STEM XEDS will be discussed in Section 4.6.4.

SEM imaging has been heavily used for plan view and cross-sectional imaging of the CVD coatings characterized in this work. The SEM results were acquired using Zeiss Supra 40VP Ultra 55 and Crossbeam 540 systems with in-lens and standard SE detectors.

## 4.4 Electron backscattered diffraction and transmission Kikuchi diffraction

EBSD is a technique implemented in the SEM, where the BSEs are Bragg scattered and form Kikuchi bands onto an EBSD detector. The collected Kikuchi band patterns are then processed, including frame averaging and background subtraction. The processed Kikuchi band patterns are then indexed, through which local phases and orientations of areas of interest can be identified [94]. As shown in Figure 4.3, in EBSD experiments, the bulk sample surface is tilted by around 70º to face the detector. The spatial resolution of EBSD depends on the size of the interaction volume that Bragg diffracted BSEs escape from, where a spatial resolution of 20 ~ 50 nm can be achieved. The working distance between the scanned area on the sample surface and the polepiece in EBSD measurements is usually around 15 mm.
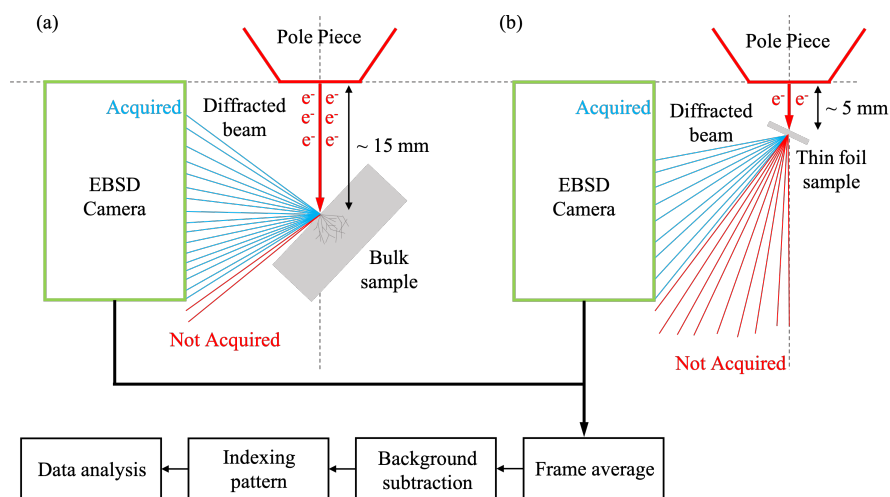


Figure 4.3. Schematics showing the basic geometries of the (a) EBSD and (b) TKD experimental setups. Reproduced from [95].

TKD technique is another SEM-based technique, where a thin foil sample is mounted with a 20° tilt, and the transmitted electrons that are first scattered sideways and then Bragg diffracted are collected by the EBSD detector. The working distance between the scanned area on the sample surface and the polepiece in TKD measurements is usually around 5 mm. Due to the small interaction volume in the transmission mode, the spatial resolution of TKD is higher than that of EBSD, and diffraction data from domains less than 10 nm can be achieved [96]. Due to larger interaction volumes for bulk samples, the BSEs undergo more inelastic scattering events and therefore exhibit broader energy spread in EBSD experiments. The broader distribution of energies and wavelengths of BSEs makes the Kikuchi patterns blurry and deteriorates signal to background ratio. However, in TKD the transmitted electrons undergo fewer inelastic scattering events within the small interaction volumes, and the recorded signal has less energy spread and a higher signal to background ratio. Therefore, TKD can provide Kikuchi patterns of higher quality than EBSD [96].

In this work, EBSD and TKD have been used to analyze the crystallographic orientation of the grains, the growth texture of the CVD coatings, and the rotation of grains (axis and angle). The EBSD and TKD data were processed with the HKL Channel 5 software from Oxford Instruments, and MTEX, a free MATLAB tool box [97].

## 4.5   Focused ion beam technique

The focused ion beam – scanning electron microscope (FIB-SEM) consists of an electron column for SEM functions, and an ion column mounted at an angle (usually 52°) with respect to the electron column [98]. In a FIB-SEM instrument, the sample is placed on a coincidence point were the electron and ion probes meet. The working distance between the coincidence point and the polepiece of the electron gun is usually around 10 mm. The ion column contains a Ga liquid ion metal source that emits $Ga^+$ ions, which are focused into a probe onto the specimen surface by an optical system of a similar design as in a SEM. The electron beam is used for imaging the specimen as in regular SEMs. The $Ga^+$ ion beam can be used for milling away material by interaction between the $Ga^+$ ions and the material (sputtering), and SEs generated during the interaction and can be used for imaging. Deposition of a Pt-containing protective layer can be performed by introducing a Pt containing organometallic compound in gas form into the chamber in the vicinity of the sample surface. This gas interacts either with the electron or $Ga^+$ ion beam that scans over the area of interest, and a Pt containing layer, typically $20\ \mu m \times 2\ \mu m \times 2\ \mu m$, is deposited onto the sample surface. The Pt deposition is widely used for protecting site specific TEM lift-out samples, and to weld the sample to a micromanipulator or a TEM specimen grid. The recipe details for preparing the TEM lift-out thin foil specimens are described in references [99,100].

In this thesis work, an FEI Versa 3D FIB-SEM equipped with a micromanipulator has been used for preparing site-specific TEM lift-out specimens and polished coating cross-sections for EBSD measurements, and the preparation of tip specimens for APT analysis.

## 4.6    Transmission electron microscopy

The electron microscopy characterization in this work was mainly done by transmission electron microscopy, in both the TEM and STEM modes. TEM is a powerful instrument that enables high spatial resolution imaging together with the acquisition of chemical and crystallographic information. In this section, the regular configuration of a TEM instrument, and the principles of the TEM/STEM operations used in this research are presented.

### 4.6.1    Instrument configurations

The configurations of TEM differ slightly depending on each instrument, therefore this section will be focused on the instrument used in this research. In this work, TEM/STEM characterization was performed using an FEI Titan 80-300 TEM/STEM instrument, and the basic configuration is schematically shown in Figure 4.4. A TEM mainly consists of three systems: the illumination system, the image formation system, and the projection and image recording system.

In the illumination system, the primary electrons are emitted from an electron gun. In this research, a Schottky FEG is used. It exhibits higher brightness than the thermionic gun, which enables a smaller probe size and a higher spatial resolution, as the source size can be significantly demagnified without severe loss of primary beam current [101]. The emitted electrons are then accelerated by an anode, and the microscope is mainly operated at 300 kV in this research. The condenser system is located below the electron gun. A strong C1 lens first collects electrons from a large solid angle and forms a demagnified image of the source. The electron beam current is mainly controlled by the C1 aperture and by tuning the C1 lens strength. The second condenser lens (C2) projects the demagnified image of the source formed by C1 onto the specimen, where the illumination area is controlled by C2 and the beam convergence angle by the C2 aperture. In older TEMs, the illumination area and convergence angle cannot be tuned independently by only the C2 lens and the C2 aperture. In newer TEMs, this is realized by introducing another condenser lens (C3) and a corresponding aperture (C3 aperture).
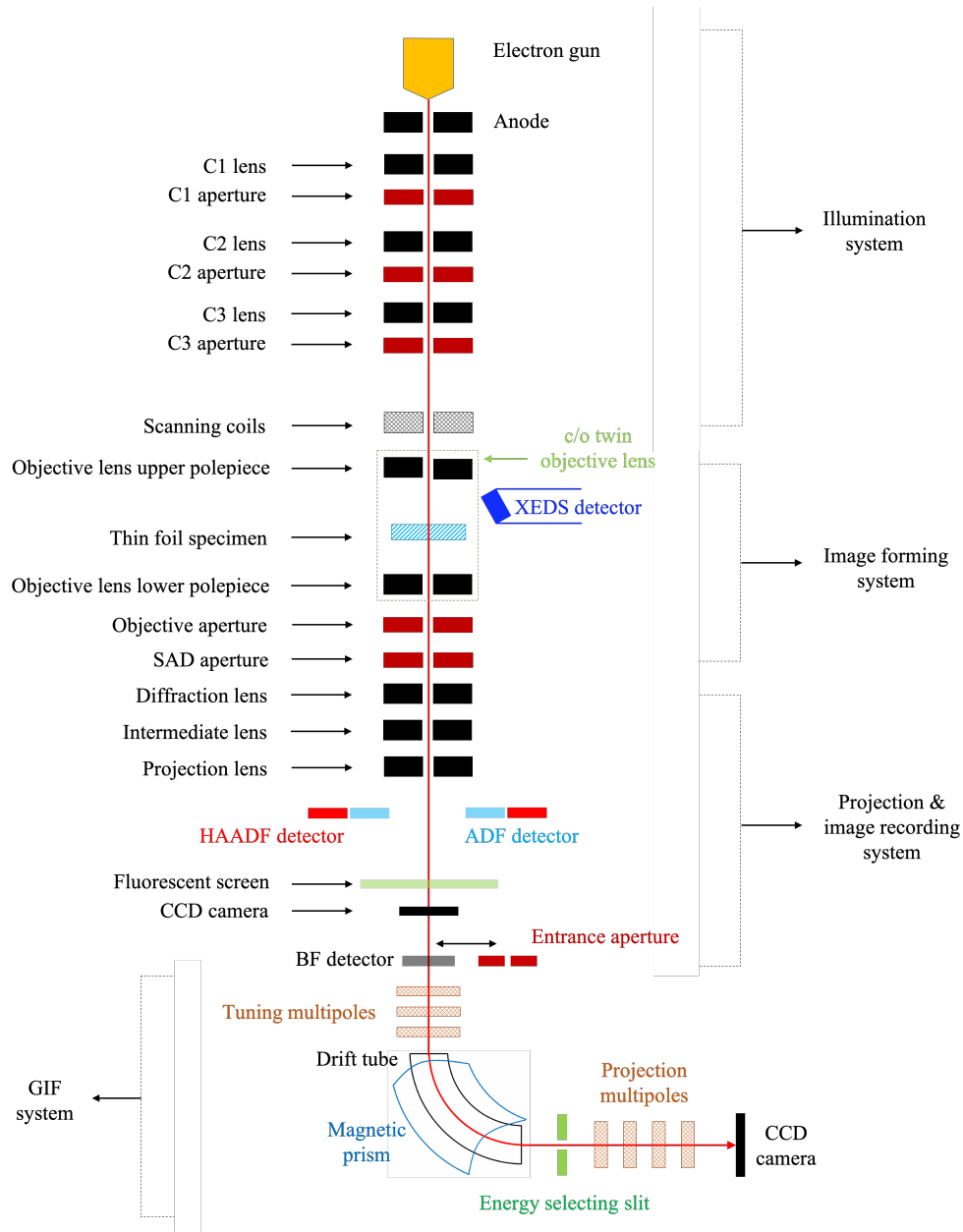
Figure 4.4. Schematics of basic TEM configurations. The TEM is mainly composed of the illumination system, image forming system, projection and image recording systems and the GIF system.

The image forming system is a critical part of a TEM, mainly consisting of the objective lens and objective aperture. The objective lens is a critical component of a TEM as it determines the resolving power of the microscope in TEM mode. The thin foil sample is usually immersed into the strong magnetic field created between the upper and lower polepieces of the objective lens. A solid-state Si XEDS detector made of a reverse-biased p-i-n diode ('p-doped' – 'intrinsic' – 'n-doped') is mounted close to the sample in order

to obtain a large solid angle for collection of characteristic X-rays. The transmitted electrons are collected to form an image in the objective lens image plane and a diffraction pattern in the objective back focal plane. The objective aperture in the objective back focal plane can be used for BF and DF imaging. A selected area electron diffraction (SAED) aperture can be inserted in the image plane to choose a specific area for electron diffraction.

The image or diffraction pattern formed by the image forming system is then collected by the projection and image recording system. This system consists of several lenses, including a diffraction lens, an intermediate lens, and a projection lens. High angle annular dark field (HAADF) and annular dark field (ADF) detectors are placed in the diffraction plane to collect transmitted electrons with different scattering angles for STEM imaging. The final image or diffraction pattern can be viewed on a fluorescent screen or recorded on a charge coupled device (CCD) detector. A Gatan image filter (GIF) system is mounted below the CCD camera for EELS and energy filtered TEM (EFTEM) operations. It consists of an entrance aperture, a magnetic prism, pre- and post-prism multipoles (tuning multipoles, and projection multipoles), an energy selecting slit and another CCD camera.

### 4.6.2   TEM mode

In TEM mode, a (nearly) parallel primary electron beam illuminates the thin foil specimen, which is typically around 100 nm thick. The high energy electrons scatter elastically and inelastically inside the specimen within a narrow interaction volume, as illustrated in Figure 4.5. Backscattered signals, such as characteristic X-rays, SEs and BSEs, are emitted. Characteristic X-rays can be collected by the XEDS detector, closely mounted above the thin foil specimen. However, SE and BSE detectors are usually not implemented in TEM due to size restriction of the objective lens. TEM micrographs are formed by collecting electrons that are transmitted by the thin foil specimen.

BF imaging in the TEM is realized by inserting the objective aperture in the back focal plane of the objective lens, only allowing the direct beam to pass. The BF micrograph exhibits mainly mass-thickness contrast and diffraction contrast [93]. The mass-thickness contrast depends on the average atomic number $Z$ and local specimen thickness $t$, where areas with greater $Z$ and $t$ scatter more electrons and therefore appear darker in the BF micrograph. For diffraction contrast, the BF micrographs appear darker at areas where the crystal orientation is closer to a Bragg condition with respect to the incident electron beam. In the present work, TEM BF imaging has been used to study grain morphology and growth dislocations inside the grains.
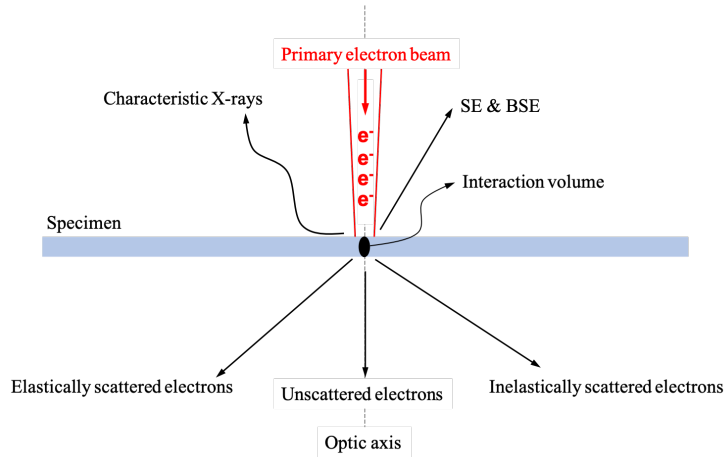
Figure. 4.5. Schematics of TEM signals originating from the interaction between the high energy electron beam and the thin foil sample.

Figure 4.6 shows the TEM BF imaging of the CVD TiAlN coatings. According to the diffraction contrast in the TEM BF micrographs, one can differentiate grains grown with different orientations, and thus study the grain morphologies. Figure 4.6 (a) shows a cross-section of the TiAlN coating, and the grains are found to be columnar. Figure 4.6 (b) shows a plan view morphology of the TiAlN grains.

The elastically scattered electrons are deflected from the incident direction resulting in Bragg diffraction according to Bragg's law. TEM DF imaging is realized by inserting the objective aperture in the back focal plane of the objective lens, and only allowing the electron beam of a certain diffracted angle range to pass. The DF micrographs mainly exhibit diffraction contrast, where areas closer to the Bragg conditions appear brighter [93]. In this thesis, the TEM DF imaging is used to study the dislocations in the grains of the CVD TiAlN coatings.

Standard TEM imaging techniques include both the unscattered and the scattered electrons. High resolution TEM (HRTEM) is performed by using a large objective aperture (or no objective aperture), and these images exhibit phase contrast with atomic spatial resolution due to interference between the direct beam and diffracted beams [101]. HRTEM has been used in this work to reveal crystal orientation, atomic arrangement and phase content in regions of interest.

The inelastically scattered electrons have lost energy through various inelastic scattering events, e.g. bulk plasmon excitation, inter- and intra-band excitation or core shell ionization [93]. The inelastically scattered electrons can be recorded by a GIF system and employed for EELS and EFTEM measurements, which provide information regarding the chemistry and electronic structure of the specimen [93,102].
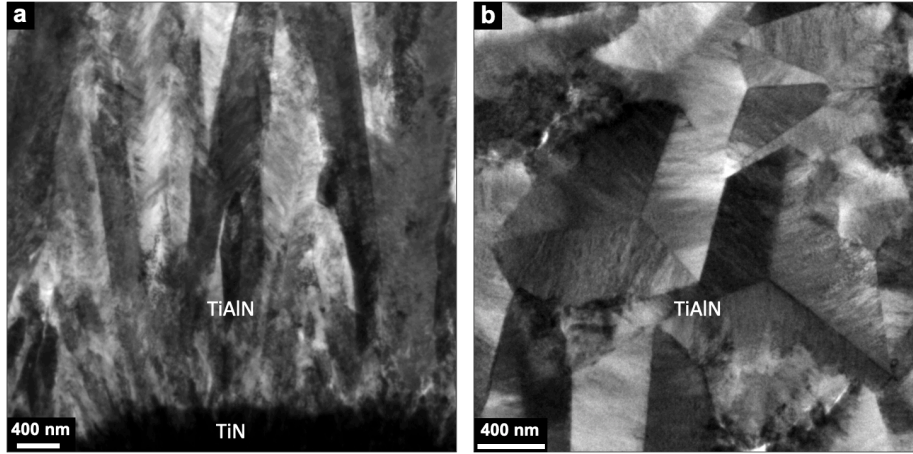
26

Figure. 4.6. TEM BF imaging from CVD TiAlN coatings. (a) Cross-sectional imaging; (b) plan view imaging.

### 4.6.3 STEM mode

In STEM mode, information is recorded by serial acquisition, where a rectangular area of the thin foil specimen is scanned by a convergent electron beam that is focused into a fine probe by the condenser lenses. Due to the much smaller illumination area compared to the TEM mode, the interaction volume in STEM mode is much smaller, which therefore enables high spatial resolution for various signals, as shown in Figure 4.7. Characteristic X-rays from the narrow interaction volume can be recorded and form an XEDS spectrum image, which is a data set where each pixel of the image contains an XEDS spectrum. SEs and BSEs are usually not used in TEM for imaging, although high resolution SE imaging was reported being implemented by using an SE detector in an aberration-corrected STEM instrument [103]. However, normally STEM imaging is realized through collecting transmitted electrons with different scattering angles by detectors mounted in a conjugate back focal plane of the objective lens, below the projection lens. As shown in Figure. 4.7, the STEM BF mode is performed by collecting transmitted electrons that are unscattered (or scattered less than 10 mrad from the optical axis) using a BF detector. Similar to the TEM BF imaging, STEM BF imaging shows mass-thickness contrast and diffraction contrast. ADF imaging is performed using a concentric detector to collect transmitted electrons that are scattered from the optical axis between approximately 10 and 50 mrad, which contribute to mass-thickness contrast and diffraction contrast. To exclude the Bragg diffracted electrons and only collect incoherent elastically scattered electrons, a larger concentric HAADF detector is used. STEM HAADF imaging collects transmitted electrons with a scattering angle higher than 50 mrad, which is similar to unscreened Rutherford scattering, where the scattering cross-section increases with $Z^2$. However, due to the screening effect by the electron cloud, the Z dependence varies between $Z^{1.7}$ and $Z^{1.9}$ depending on the inner collection angle [104]. In this work, STEM

HAADF imaging has been used to study the distribution of elements, especially at the atomic scale.
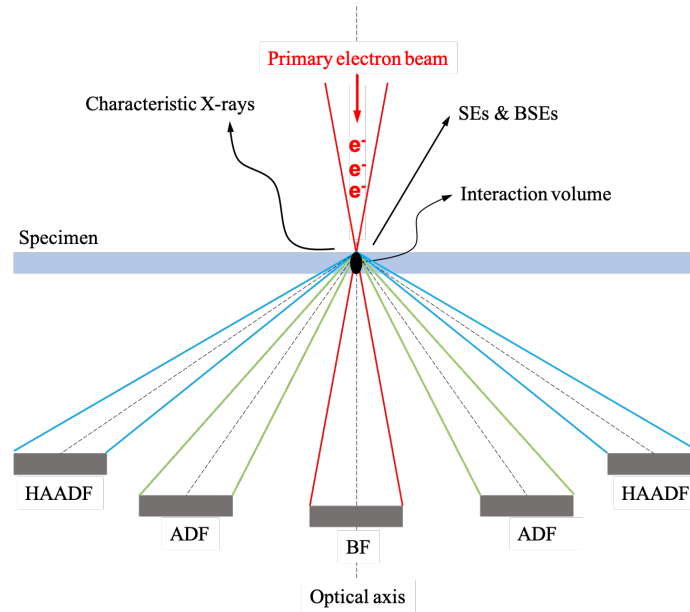


Figure 4.7. Schematics of the STEM signals and detectors for various operating modes.

### 4.6.4  X-ray energy dispersive spectrometry

Analytical STEM XEDS is intensively employed in this study, which gives high spatial resolution for chemical analysis for a given region of interest. Atoms can be ionized by the high energy primary electron beam, where an inner shell electron is excited to the vacuum state leaving an inner shell hole. The relaxation to the ground state through transferring an outer shell electron to the inner shell hole can lead to the emission of characteristic X-rays with an energy unique to the atom. The innermost electron shell is called the K shell, the next is the L shell, and the next M, and so on. During the penetration of primary electrons through the specimen, their momenta change substantially due to Coulomb interaction with nuclei, which emits the so-called Bremsstrahlung X-rays. The incident electrons can lose any amount of energy to produce Bremsstrahlung X-rays from zero to the primary beam energy, which therefore yields a continuous background in the XEDS spectra. X-rays emitted from the specimen are recorded by semiconductor detectors. The X-ray photons entering the detector can excite the semiconductor electrons from the valence band to the conduction band and cause electron-hole pairs. The energy for this process in Si is on average around 3.8 eV at liquid $N_2$ temperature. The X-ray energy is thus quantified by the number of electron-hole pairs. The energy resolution achieved by such type of detector is around 135 eV [93].

Both identification and quantification of chemical elements can be done from XEDS spectra. The elements in the specimen are typically identified by the location of their characteristic X-ray peaks in the spectrum, although the poor energy resolution (peak overlap) is sometimes a limit. For quantification of different elements, the Bremsstrahlung background of the XEDS spectrum needs to be subtracted. This background subtraction may, for example, be done through defining several background windows where no characteristic X-ray peaks exist, where the background is fitted by polynomial functions and extended to the remaining regions. Once the background is subtracted, the intensities of certain X-ray peaks for each element are integrated. Assuming $I_A$ and $I_B$ are the integrated peak intensities of elements A and B present in the specimen, the *Cliff - Lorimer* equation allows quantification of the ratio of these two elements as:

$$\frac{C_A}{C_B} = k_{AB} \frac{I_A}{I_B} \qquad (4.1)$$

where the $C_A$ and $C_B$ are the concentrations of elements A and B in the specimen, the $k_{AB}$ is the Cliff-Lorimer factor calibrated by standard samples [93].
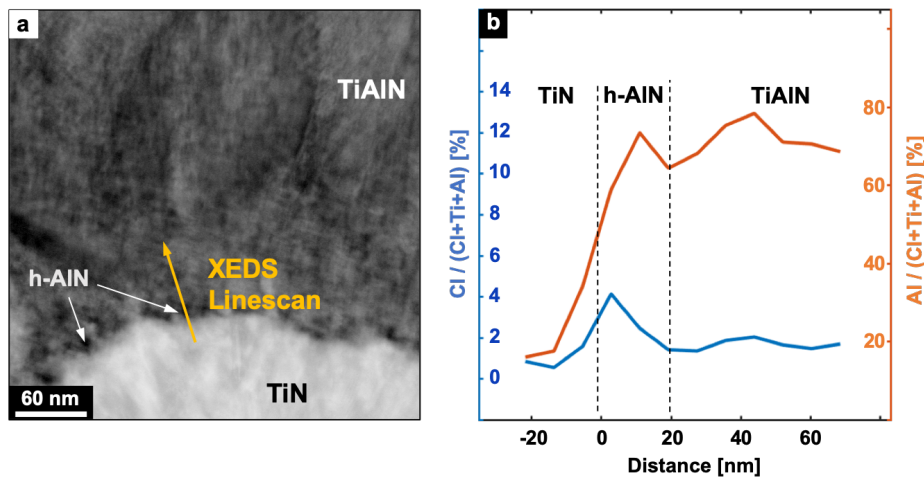


Figure 4.8. Example of STEM XEDS analysis of the TiN/TiAlN interface. (a) STEM HAADF imaging of the TiN/TiAlN interface. An XEDS linescan is collected as illustrated by the yellow arrow. (b) Variations of the Cl and Al ratios along the linescan shown in (a), obtained from the XEDS data.

In this research, XEDS quantification has been widely employed to determine the ratio of various elements. The data processing is implemented by the XEDS software packages. An example of STEM XEDS analysis is shown below. An XEDS linescan is acquired across a TiN/TiAlN interface, as illustrated in Figure 4.8 (a). Using the XEDS data, the

spatial variations of Al and Cl are displayed, see Figure 4.8 (b). The peaks of Al and Cl at the TiN/TiAlN interface indicate a co-enrichment of the Al and Cl, which is further discussed in the appended Paper I.

### 4.6.5 Electron energy loss spectroscopy

STEM EELS is used in this study for element identification requiring both high spatial and high energy resolution that XEDS cannot achieve. Electrons may undergo various inelastic scattering events within the specimen. The energy of the transmitted electrons is recorded, and electron counts as a function of energy loss is displayed by the GIF system as an EELS spectrum. A typical EELS spectrum contains a narrow zero loss peak (ZLP), a low loss regime, and a core loss regime. The ZLP contains electrons that lose no (or very little) energy when penetrating the specimen, and the width of the peak defines the energy resolution of the recorded EELS spectrum [93,102]. The low loss region extends from the ZLP to $50 \sim 100$ eV, which mainly contains plasmon peaks. The low loss spectra can be used to determine the sample thickness and to exclude the contribution of plural inelastic scattering to the ionization edge intensity for absolute element quantification [93,102]. After the low loss area is the core loss region, where the inner shell ionizations are shown as edges of the corresponding elements. The energy resolution of < 1 eV of EELS makes it possible to differentiate the Ti $L_{23}$ edge (456 eV) from the N K edge (401 eV), which is used in the appended Paper I to identify the presence of elements to identify the various phases.

### 4.6.6 STEM probe size and imaging resolution

The spatial resolution of STEM imaging is mainly limited by the size of the convergent electron probe scanned across the specimen. According to Rayleigh's theory, the electron probe converged by an aperture is designated as an Airy pattern, assuming the primary beam is solely diffraction limited [101]. The probe radius limited by the illumination aperture effect, is given as:

$$r_d \approx 0.61 \frac{\lambda}{\alpha} \tag{4.2}$$

where $r_d$ is the radius of the focused electron probe limited by diffraction, $\lambda$ is the wavelength of the incident electron beam, and $\alpha$ is the convergence angle (in radians) of the incident beam. According to equation (4.2), the focused probe size decreases with shorter wavelength of incident electrons and with larger convergence angle. However, the imperfections of electromagnetic lenses also limit the size of the electron probe where the spherical aberration is the main factor and given by:

$$r_s \approx \frac{1}{4} C_s \alpha^3 \tag{4.3}$$

where $r_s$ is the radius of the focused electron probe limited by spherical aberration and $C_s$ is the coefficient of the spherical aberration. According to equation (4.3), the electron probe size increases with a larger convergence angle. The STEM probe size is also influenced by the chromatic aberration and the effective source size, which however are negligible compared to the diffraction limit and the spherical aberration. As decreasing the size of illumination aperture suppresses the spherical aberration but leads to more diffraction effects, there is an optimal illumination aperture size that gives the optimal convergence angle $\alpha_{opt}$ for the smallest probe size and highest spatial resolution:

$$\alpha_{opt} \approx \left( \frac{4\lambda}{C_s} \right)^{1/4} \tag{4.4}$$

The spherical aberration cannot be corrected for by electromagnetic lenses, since no concave magnetic lenses exist. It thus has to be corrected by $C_s$ correctors that contain a complex arrangement of multiple hexapoles, or octupoles, and quadrupoles [101]. Using the $C_s$ corrector suppresses the spherical aberration, which allows a larger illumination aperture ($C_2$ aperture) and thereby suppresses the diffraction effect. The microscope used in this research is equipped with a spherical aberration corrector for the condenser lens, which gives an ideal spatial resolution of around 1 Å that enables atomic scale HRSTEM imaging, which is used in this research to reveal the atomic arrangement, phase identity and crystal orientation in the sample.

### 4.6.7 Beam broadening and spectrometry/spectroscopy resolution

The spatial resolution of XEDS and EELS depends on the size of the interaction volume within the thin foil specimen, as shown in Figure 4.9. In STEM mode, the convergent beam is a focused probe with a diameter of $d$. The beam propagating through the specimen broadens and exits the bottom surface with diameter of $R_{max}$. The spatial resolution $R$ for spectroscopy analysis is defined as the smallest distance between two interaction volumes that give independent spectra [93]:

$$R = \frac{(d + R_{max})}{2} = (d^2 + b^2)^{1/2} \tag{4.5}$$

where $b$ is the electron beam broadening within the specimen (in m) and can be calculated as [93]:

$$b = 8 \times 10^{-12} \frac{Z}{E_0} (N_v)^{1/2} t^{2/3} \qquad (4.6)$$

where $t$ is the thickness of specimen (in m), $E_0$ is the energy of primary electron beam (in keV), $N_v$ is the number of atoms per unit volume (in m$^{-3}$), and $Z$ is the atomic number.
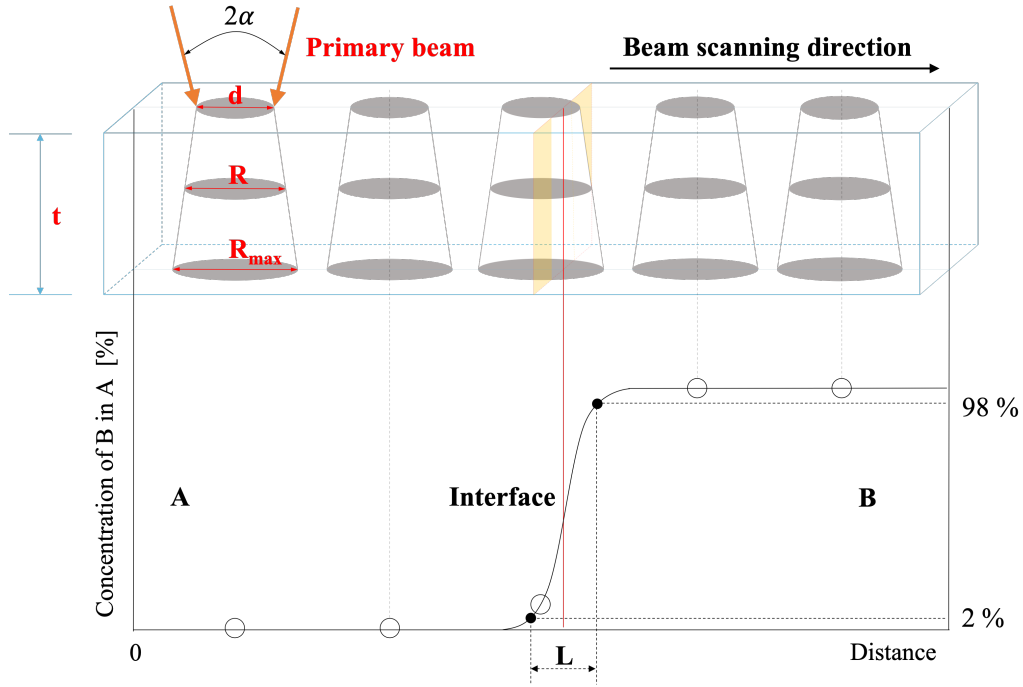


Figure 4.9. Schematic diagram illustrating the influence of the beam broadening effect on the spatial resolution of the STEM XEDS and EELS analysis.

In STEM XEDS/EELS experiments, the spatial resolution is mainly limited by the beam broadening, which is typically $5 \sim 10$ nm, instead of the nominal probe size. Therefore, higher current with larger probe size (few nm instead of Å) can be used to obtain more incident electrons to get a higher signal to noise ratio. For STEM XEDS analysis, a thicker sample provides higher X-ray counts for better statistics, which is essential for quantification. However, the beam broadening effect increases with specimen thickness and therefore lowers the spatial resolution of the analysis.

The intensity of XEDS and EELS signals should also be considered for the actual spectroscopic studies. As illustrated in Figure 4.10, the characteristic X-ray photons are emitted uniformly in all space. A collection solid angle $\pi \rho^2$ for X-ray photons usually only allows capturing of $0.01\% \sim 1\%$ of the emitted characteristic X-ray photons,

although the XEDS detector is mounted as close to the specimen as possible and the take-off angle $\varphi$ is optimized to maximize the collection efficiency. Therefore, higher beam currents and/or thicker specimens may be used in XEDS acquisition for an increased number of counts, which however deteriorates the actual spectroscopic spatial resolution due to larger probe size and more beam broadening.
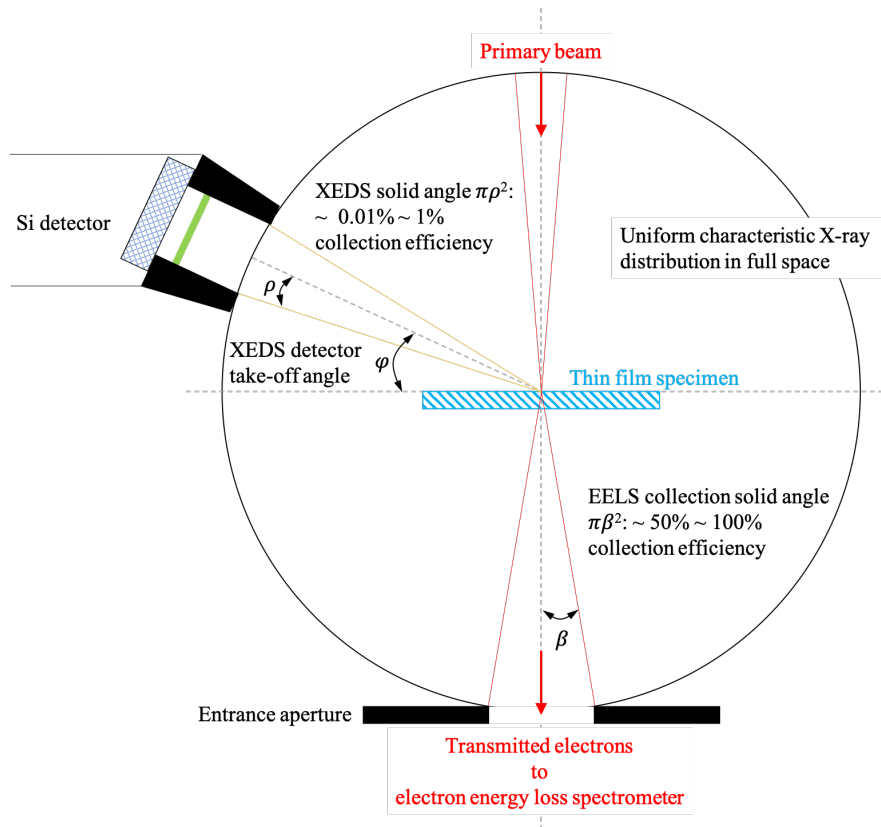


Figure 4.10. Schematic illustration of collection efficiencies of STEM XEDS and EELS. The characteristic X-ray photons are almost uniformly emitted in space. The energy loss electrons are strongly forward scattered and can be collected with high efficiency with a small collection angle.

The inelastically scattered electrons are significantly forward scattered. A 50 ~ 100 % collection efficiency of the EELS signal may, hence, be obtained with a small collection solid angle $\pi\beta^2$ (limited by the entrance aperture of the electron energy loss spectrometer). A low beam current and a thin specimen may then yield a sufficient number of counts for EELS acquisition with high spatial resolution.

## 4.7   Atom probe tomography

APT is a destructive method for characterization of chemical composition in 3D on the nanoscale with a few parts per million (ppm) chemical sensitivity. The technique provides valuable insights on local compositions and segregations to interfaces [105]. In addition, 3D variations in nano-chemistry, hidden in the 2D projection of electron micrographs, may be revealed within APT reconstructions. In APT, a needle shaped specimen is prepared from the interesting area of the material.  Typically, the needle has a tip radius less than 50 nm. During the APT measurement, the needle is subjected to a high positive DC voltage. Then a process called field evaporation happens, where a voltage or a laser pulse is applied on the needle tip in an ultra-high vacuum environment ($\sim 10^{-9}$ Pa) and at a cryogenic temperature (20 – 100 K). This will cause a controlled ionization of atoms located at the surface of the tip. The evaporated ions will leave the tip surface and be accelerated through a circular counter electrode, and then be detected by a position sensitive detector. The type of ion complex may be determined from the time of flight, i. e. the time it takes for the ion to reach the detector after the application of the voltage or laser pulse. The positions on the detector that the evaporated ions hit could be used to reconstruct the atom locations in the tip specimen in 3D.

In this thesis work, APT was performed to determine the 3D distribution of the Ti, Al, and N atoms in the nanolamella architectured TiAlN synthesized by LPCVD. In Figure 4.11 (a), the full APT mass spectrum is displayed in logarithmic scale. A potential problem influencing the compositional accuracy is the overlap of the thermal tail of the $Al^{2+}$ peak (13.5 Da) with the $N^+$ peak (14 Da) in the APT mass spectrum. Nevertheless, the mass resolution could be improved by decreasing the local heating effect during the field evaporation. This is accomplished through polishing the APT tips with a wider shank angle, improving the heat conductivity. As seen in Figure 4.11 (b), an enlarged local mass spectrum, the $Al^{2+}$ peak (13.5 Da) and the $N^+$ peak (14 Da) are well separated, and consequently the compositional error contributed by the $Al^{2+}$ thermal tail to $N^+$ is in the range of 0.1 at.%.
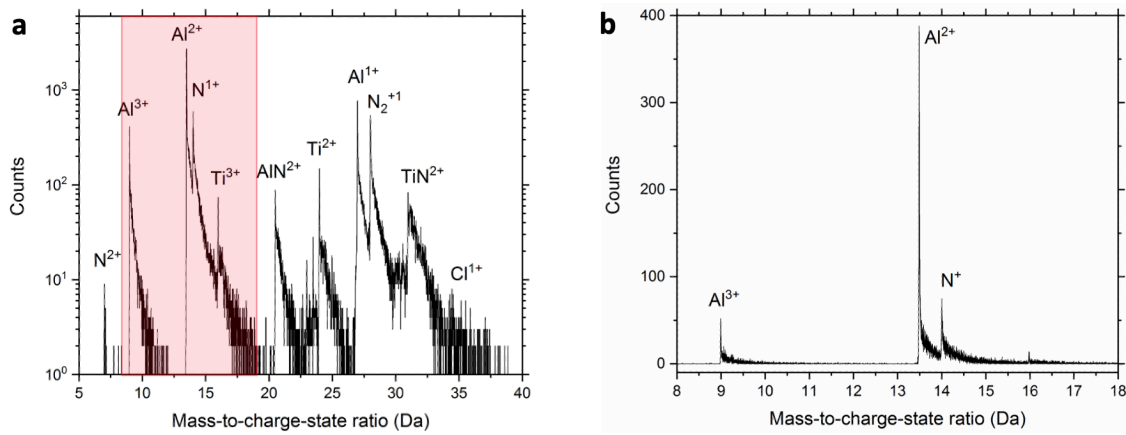
Figure 4.11. APT data. (a) Full mass spectrum of the APT measurement, where counts (number of ions) are shown in logarithmic scale. (b) An enlarged local mass spectrum showing the $Al^{3+}$, the $Al^{2+}$, and the $N^+$ peaks (in linear scale), for the area marked by the red background in (a). Reproduced from paper III.

## 4.8    Modelling considerations

### 4.8.1    Computational fluid dynamics

Computational fluids dynamics (CFD) simulations solve problems regarding the flow of fluids (liquids and gases), where various physical properties of the fluids including pressure, temperature and velocity are considered for simulating the heat and mass transport. A 3D model of the system is built and meshed, where each mesh consists of fluid cells for fluid flow analysis and solid cells for heat conduction analysis. The mass transport is calculated by numerically solving the Navier-Stokes equations for the fluid cells, and the heat transfer is calculated for the solid cells by solving the heat equation derived from the Fourier's law [106].

In Paper II, the microstructural inhomogeneities in the TiAlN coating are found to be influenced by the precursor gas flow rate. Therefore, to correlate the microstructures of different locations on the cutting tool insert to the corresponding local gas flow rate, a CFD simulation was performed by Walter AG, Germany, using a Solidworks Flow Simulation software, to determine the gas flow patterns during the LPCVD process for the deposition of TiAlN coatings in a hot wall CVD reactor.

### 4.8.2   Density functional theory

Density functional theory (DFT) is a first-principle method to understand the physical properties of condensed matter, where the electronic structures are calculated based on Schrödinger's equation. In theory, it is possible to derive all properties of a system by determining the many-body wave function, which is a function of all the coordinates of electrons and nuclei in the system. This turns out to be impossible in reality due to the limited computing power, and thus approximations must be made to simplify the problem. The first common approximation is the Born-Oppenheimer approximation, which treats all nuclei as fixed [107]. However, solving directly the Schrödinger's equation of a system with $n$ electrons requires to determine a many-body wave function with $3n$ variables that involve the three coordinates of each electron, and it becomes intractable for more than a handful of electrons. To solve this problem, the Hohenberg-Kohn theorems were proposed, stating: (a) all properties of the system are uniquely determined by the ground state electron density; (b) an energy functional of the electron density exists, and the ground state electron density can be determined according to the minimum of the energy functional [108]. The Hohenberg-Kohn theorems therefore simplify the problem of solving the many-body wave function with 3n variables into a problem of determine the ground state electron density with 3 variables, which is tractable for a system with hundreds of electrons. More technique details of the DFT simulations can be found in reference [108].

In this work, DFT simulations were performed by colleagues from the Royal Institute of Technology, Sweden, using the Vienna *ab-initio* simulation package (VASP) [109]. In Paper II, a co-growth of h-AlN onto the Ti(Al)N lamellae with a specific crystallographic orientation relationship was found by electron microscopy. DFT modelling was performed to calculate the interface energies of the h-AlN/Ti(Al)N and the h-AlN/Al(Ti)N interfaces, which helped to explain the formation of the h-AlN in the TiAlN coatings. In addition, the adsorption energies of the reacting gas species (aluminium chlorides and titanium chlorides) onto the cubic TiN, $Ti_{0.5}Al_{0.5}N$, $Ti_{0.1}Al_{0.9}N$, and AlN phases were calculated, to help to understand the surface kinetics of the Al and Ti deposition.

### 4.8.3   Thermodynamic modelling

In thermodynamic modelling, a phase is usually considered as a mixed solution of several solutes of the constitute elements. The Gibbs energy of a phase is usually expressed as a collection of polynomials consisting of the initial Gibbs energies of pure solutes, the Gibbs energies caused by mixing, and extra terms that describe the interactions of elements in a certain phase. The Gibbs free energy of each phase is a function of temperature, pressure, and composition. The phase diagram calculation is to predict the

existence and the compositions of the corresponding phases in a system, by minimizing the total Gibbs energy of the system at each given temperature and pressure. For thermodynamic modelling, it is essential to know the Gibbs energy polynomials of the studied phases, which are implemented in thermodynamic databases [110].

In Paper V, phase diagrams were calculated by colleagues from the Royal Institute of Technology, Sweden, using the Thermo-Calc software [111]. The thermodynamic calculations predict the existence of stable phases that contain the components of the CoCrFeNi substrate, and the fraction of metal chlorides formed during the CVD process at different temperatures. The STEM XEDS measurements together with the thermodynamic simulation indicate that Cr would deplete in the substrate and diffuse into the coating.

# 5 Grain misorientation and dislocations

Thin film growth is influenced by the formation of grown-in dislocations. This has been observed for various materials that are synthesized by CVD, e.g. semiconductor materials like GaN, diamond and metals like silver, copper and aluminium [47,112–124]. Revealing the formation mechanism of these dislocations is important in order to understand the growth of thin films by CVD. Relevant theories of dislocations, especially the typical dislocations in epitaxially grown thin films, are therefore introduced in this chapter.

## 5.1 *Intra-grain misorientation*

The dislocations formed during the CVD process can cause a continuous development of a crystallographic misorientation (local rotation), see Paper IV. In this section, basic principles of misorientation, rotation and bending of crystals, and their relationship with the formation of dislocations, are described.

The concept of misorientation is used to describe the difference in crystallographic orientations between different areas (with a same crystal structure) within a same specimen frame (the coordinate system to describe the geometry of the specimen). The amount of misorientation relates to the necessary transformation to move one crystal frame (the crystal coordinate system) into the orientation of another crystal frame, and is usually described in three different ways that are, however, related mathematically:

- **Euler angles**: the misorientation of one crystal (crystal A) with respect to another (crystal B) can be defined as three successive rotations about specific axes (usually the axes in the Cartesian coordinates) and angles. Euler angles are usually defined in the ZXZ axes system to be $\varphi_1$, $\Phi$, and $\varphi_2$, which means the crystal A needs to rotate in three steps to have the same orientation as the crystal B: (i) first rotate about the Z axis by an angle $\varphi_1$; (ii) then rotate about the X axis by an angle $\Phi$; and (iii) finally rotate about the Z axis by an angle $\varphi_2$. In addition, Euler angles are also used to describe the orientation of a specific crystal frame with respect to the defined specimen frame, and is commonly used in EBSD and XRD pole figures. The angles are defined as the necessary rotation for rotating the crystal frame for each measured spot (pixel) to be aligned with that of the specimen frame.

- **Rotation matrix**: for an arbitrary crystal orientation, one can transfer it into two orientations in the specimen frame corresponding to two crystallites (A and B). The two orientations in the specimen frame for the crystals A and B can be represented by two vectors. Misorientation between these two vectors in the

specimen frame is thus described by a rotation matrix that is necessary to transfer one vector into the other.

- **Rotation axis and angle**: the necessary rotation needed to transfer crystal A into crystal B can be described by a rotation axis and a rotation angle about this axis. The rotation axis can be represented either in the crystal frames of A and B, or in the specimen frame. The rotation axis and angle are commonly used in our analysis for the rotational growth of the TiAlN grains.

The rotation of the crystals (grains) can be correlated to the dislocations formed during the CVD growth. To help understand the dislocation formation correlated to the growth of the TiAlN grains (Paper IV), basic theories of dislocations, and two types of growth dislocations in epitaxially grown thin films (interfacial dislocation and threading dislocation), are described in the following sections.

## 5.2   Basics of dislocation theory

Dislocations are one-directional (line) defects that exist in crystalline materials, and accommodate a displacement between two parts of a crystal or a grain. Gliding of dislocation allows plastic deformation under a low shear stress level, where adjacent atomic planes are shifted by the shear stress through successively breaking the atomic bonds along the dislocation line. In this case, the dislocation is seen as the boundary between the slipped and the unslipped part of the deformed crystal. The amount and the direction of the displacement between the two parts of the crystal is characterized by a vector $b$, called Burgers vector. If the Burgers vector is a lattice vector of the crystal, the dislocation is called a perfect dislocation. In this case, no change of atomic arrangement can be seen after the gliding of such a dislocation. If the Burgers vector is smaller than a lattice vector, the corresponding dislocation is called a partial dislocation. In this case, the stacking sequence of the crystal changes after the dislocation movement. Dislocation lines could be linear or curved. If the dislocation line direction is parallel to the Burgers vector, the dislocation is a screw dislocation. If the dislocation line is perpendicular to the Burgers vector, the dislocation is an edge dislocation. A mixed dislocation is defined as one having a Burgers vector that is neither perpendicular nor parallel to the dislocation line.

The TiAlN phase has a rock salt structure and thus an FCC lattice. Therefore, we only consider the dislocations in FCC crystals in this thesis. The energy of a dislocation depends on the length of the dislocation line and the magnitude of the Burgers vector. For perfect dislocations in FCC lattice, the Burgers vectors are generally a/2 <110> vectors, where a is the lattice parameter. To reduce the dislocation energy, one perfect dislocation could split into two partial dislocations. In FCC crystals, an example of this reaction could be represented as:

$$\frac{a}{2}[110] \rightarrow \frac{a}{6}[211] + \frac{a}{6}[12\bar{1}]$$

where a/6 [211] and a/6 [12$\bar{1}$] are Burgers vectors of the split dislocations that are called Shockley partial dislocations. Together with the splitting of dislocation, a stacking fault is produced between the Shockley partial dislocation lines. The Thompson tetrahedron is a useful tool to note the Burgers vectors in FCC crystals. As illustrated in Figure 5.1, the four faces of the Thompson tetrahedron belong to the {111} planes, and the six edges are along <110> directions. The center of each face is denoted by Greek letters $\alpha$, $\beta$, and $\gamma$, thus <112> directions can be denoted by vectors from the tetrahedron corners to the centers of the planes.
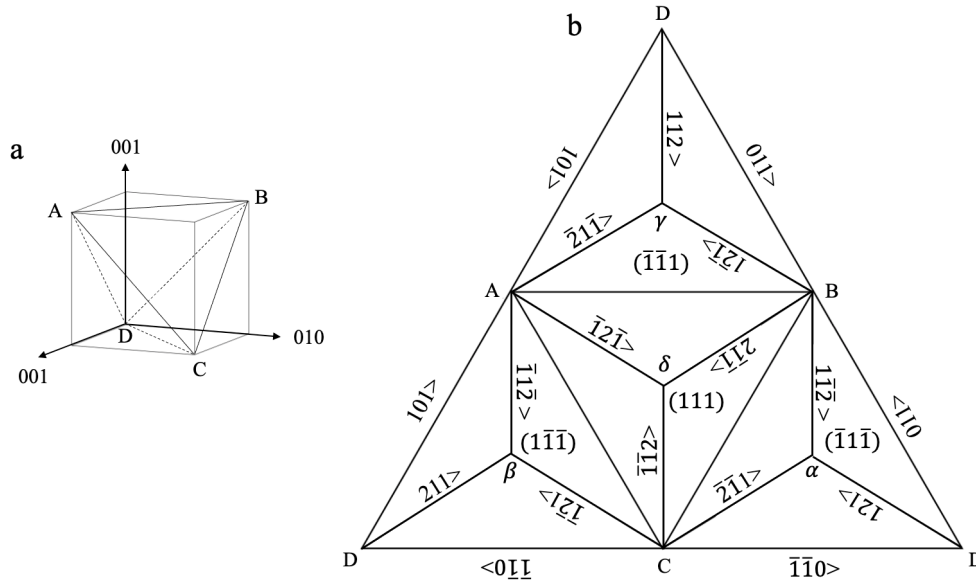


Figure 5.1. Thompson tetrahedron in FCC crystal. (a) Cubic unit cell and the Thompson tetrahedron (ABCD). (b) Unfolded Thompson tetrahedron.

## 5.3 Interfacial dislocations

Lattice mismatch exists in the heteroepitaxial growth (where the film grows on a substrate of a different material) between the grown thin film material (adlayer) and the substrate, either as a difference of atomic spacings or a difference of structure symmetries of the adlayer and the substrate. Generally, the lattice mismatch is accommodated by the lattice strain or through forming strain relieving defects at the interface, e.g. interfacial dislocations. A model by Matthews has been widely used to describe the heteroepitaxial growth process of thin film materials [112]. The adlayer has a bulk lattice parameter as $a_{ad}$, and the bulk lattice parameter of the substrate is $a_{sub}$, and the lattice mismatch is

defined as: $f = |a_{ad} - a_{sub}|/a_{ad}$. In the Matthews model, the adlayer is expected to start with a so-called pseudomorphic growth, where the lattice of the adlayer is strained relative to the substrate instead of forming any strain relieving defect. The pseudomorphic growth maintains until a critical thickness $h_c$ of the grown adlayer is reached. Above $h_c$, the energy cost of forming an interfacial dislocation is lower than that cost of the elastic straining of the adlayer, and the epitaxial growth is associated with strain relaxation via formation of defects at the interface, typically as misfit dislocations [112,117–119].

The Matthews model has been shown to be applicable for various metal-metal heteroepitaxy systems, such as nickel grown on copper substrate [112,120], silver grown on copper substrate [121], platinum grown on gold substrate, gold grown on copper [122]. According to the Matthews model, the critical thickness for the maximum pseudomorphic growth depends on the lattice mismatch $f$ between the adlayer and the substrate. For a small mismatch ($f < 2\%$), pseudomorphic growth can happen up to a larger layer thickness (10 – 200 Å). For a larger mismatch ($f > 10\%$), pseudomorphic growth can only happen at a small layer thickness (1 Å). However, it is worth noting that the Matthews model is a continuum model, ignoring details of the atomic structure of the interface between the adlayer and substrate. Therefore, the Matthews model has been found to be in disagreement with the phenomena found in some heteroepitaxy systems, especially those associated with closed packed interfaces [113,114,124].

## 5.4  *Threading dislocations*

Threading dislocations are important structural defects in both homoepitaxial and heteroepitaxial film growth, and widely exist in various semiconductor materials grown by CVD, PVD, and molecular beam epitaxy (MBE). Treading dislocations usually originate from the imperfection of the growth at the substrate interface [116]. There are mainly two types of imperfections that cause the threading dislocations:

- The first type of imperfection is the lattice mismatch (*f*) between the substrate and the adlayer in a heteroepitaxial growth [47]. For the heteroepitaxial system with a relatively large lattice mismatch (*f*), a small misorientation is expected when neighbouring nucleated islands coalesce, and this misorientation is accommodated by forming a low angle grain boundary (LAGB) that contains an array of dislocations. During the film growth, these dislocations are expected to be maintained at the LAGB, and penetrate through the whole film as threading dislocations. If the rotation between the neightbouring islands is along an axis normal to the interface between the substrate and the adlayer, threading dislocations with pure edge characters form. If the rotation is along an axis parallel to the interface, threading dislocations with pure screw characters form. If the rotation is

neither parallel nor normal to the interface, threading dislocations would form with mixed characters.

- The second type of imperfection is the distortion of the substrate surface, including structural distortion like stacking faults, and morphological distortion such as atomic scale roughness (steps and edges), contaminations [125–128]. If the substrate surface contains stacking faults, threading dislocations can be generated by a dissociation of Shockley partials that bound the stacking faults [126,128]. The morphological distortion (such as roughness and contaminations) of the substrate surface can cause misorientation and associated LAGB between neighbouring nucleated islands and form threading dislocations on the LAGB as described above. The threading dislocations with pure screw and mixed characters are more likely to form due to the steps and edges of atomic scale on the substrate. A typical example is the Burton – Cabrera – Frank (BCF) theory for dislocation driven growth [129]. In BCF theory, screw dislocations form along the film growth direction and create a step edge on the adlayer, and the energy barrier thus is lowered for adatoms to be absorbed at the edge location. Therefore, the thin film grows in a spiral manner around the screw dislocation. This type of screw dislocations has been widely observed in various materials [130–135].

## 5.5   Dislocation trace analysis and Burgers vector analysis

In order to describe a dislocation and correlate it to the growth of the thin film, one has to know the direction of the dislocation line in 3D and its Burgers vector. Usually, these are determined by tedious TEM imaging methods. In this section, the basic principles of Burgers vector determination and trace analysis of dislocations using TEM are described.

First, to determine the dislocation line direction, a so-called trace analysis has to be performed. TEM micrographs only contain 2D projected information. Therefore, to know the actual orientation of a dislocation line in 3D, one has to image the dislocation at different viewing angles. The procedures are: (i) tilt the grain to a zone axis, and obtain one projection of the dislocation line; (ii) obtain the diffraction pattern of this zone axis, and index the diffraction pattern; (iii) obtain a perpendicular direction of the projected dislocation line according to the diffraction pattern; (iv) plot the stereographic projection, and draw a great circle (a trace) that is normal to this perpendicular direction. The possible direction of the dislocation line is along this trace; (v) tilt the grain to another zone axis, and repeat (ii ~ iv) to get another trace in the stereographic projection; (vi) find the intersection of the two traces in the stereographic projection, and the corresponding direction is the solution of both cases (the dislocation direction in 3D). The images required for trace analysis may be obtained using any imaging mode that provides enough

diffraction contrast from dislocations, such as the TEM BF, STEM BF and STEM ADF modes.

Second, the Burgers vector $b$ of a dislocation is determined using a $g \cdot b$ analysis, where $g$ is the diffraction vector used for the dislocation imaging. In principle, the diffraction contrast of a dislocation becomes faint or even zero if $g \cdot b = 0$, (the dislocation is (almost) invisible). Thus, the Burgers vector $b$ can be determined by the cross product of two $g$ vectors that make the dislocation invisible. For dislocations with edge components faint residual contrast may exist even if $g \cdot b = 0$, when $g \cdot b_e \neq 0$ or $g \cdot b \times u \neq 0$, where $b_e$ and $u$ are the edge component of the dislocation and the line vector of the dislocation line, respectively.

# 6 Results and discussion

This thesis focuses on microstructural studies of hard CVD coating materials, including TiAlN, TiN and WN, in order to reveal the growth of these coatings during the CVD process. Six papers are appended to this thesis. Papers I to IV are about TiAlN coatings, Paper V is about TiN coatings, while Paper VI deals with WN coatings.

Paper I presents the formation of a nanolamella structure in the CVD TiAlN grains. This structure forms because of a rotational precursor gas supply, and reveals the growth facets and the texture of the TiAlN grains. Paper II studies how the microstructure in a TiAlN coating is influenced by the precursor gas flow, and reveals a co-growth of the h-AlN phase with the cubic TiAlN phase. Paper III studies the chemical composition (including N) of the nanolamellar TiAlN coatings in 3D using APT and complementary electron microscopy. A 3D fluctuation in the chemical composition was revealed. Paper IV studies the rotational growth of CVD TiAlN grains resulting in significant intra-grain misorientation, and correlates this peculiar phenomenon to the formation of dislocations during the CVD process. Paper V studies the microstructures of TiN coatings deposited on a CoCrFeNi MPEA substrate, as well as the etching effects on the substrate. Paper VI studies the microstructural details of CVD WN coatings deposited at different temperatures. The microstructures are correlated to the kinetics of the coating growth.

Important results of the appended papers will be discussed in the following sections, while more details are given in the papers.

## 6.1 Growth of CVD TiAlN coatings

### 6.1.1 Growth facets and texture

The CVD TiAlN coatings studied in this work have a strong 111 texture, as shown by the XRD pole figure in Figure 6.1 (a). The TiAlN grains have a pyramidal surface shape with a three-fold rotational symmetry, as shown in Figure 6.1 (b). As discussed in Paper I, the facets were revealed to be {001} crystallographic planes. Thus, the facets formed on the {001} planes of the 111 textured grains, leading to a pyramidal surface morphology. The development of the TiAlN grain morphology and texture during CVD could be well explained by the theory of competitive growth/evolutionary selection [51]; the formation of the strong 111 fibre texture is driven by the faceted growth of {001} crystallographic planes.
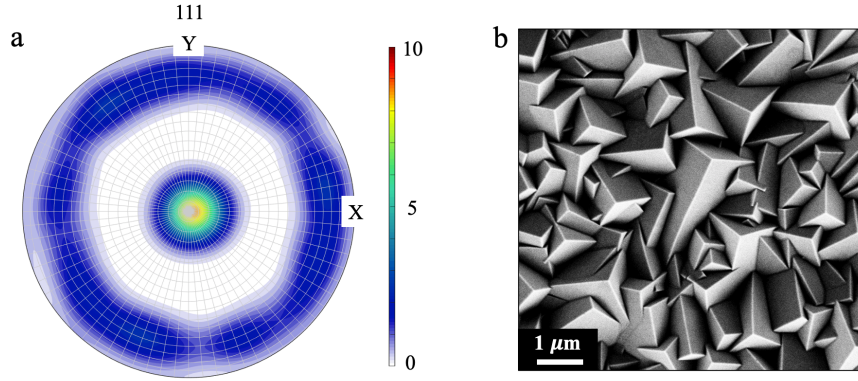
Figure 6.1. Texture and grain morphology of a CVD TiAlN coating. (a) XRD 111 pole figure viewed along the coating growth direction. X and Y are horizontal directions perpendicular to the coating growth direction. (b) SEM SE image of the pyramid shape surface morphology of a CVD TiAlN coating. Reproduced from Paper I.

### *6.1.2    The Qiu-Halvarsson pyramid*

To more easily describe the crystallographic orientations of the pyramidal TiAlN grains in 3D (geometrical relationship between the {001} facets and the 111 texture), we designed a new type of pyramid, called the Qiu-Halvarsson ('Q-H' for short) pyramid, named after Ren Qiu and Mats Halvarsson. As illustrated in Figure 6.2, different from the Thompson tetrahedron (see Section 5.2), the Q-H pyramid is composed of three {001} planes (the ADB, ADC and BDC planes) and the (111) plane (the ABC plane). In Figure 6.2 (a), the three {001} planes are colored with red (ADB), blue (BDC) and purple (ADC), respectively, to help distinguish the three growth facets of a pyramidal TiAlN grain. The (111) plane (ABC) is colored in gray, as shown in Figure 6.2 (b). Middle points of AB (the $[0\bar{1}1]$ direction), BC (the $[\bar{1}10]$ direction), and CA (the $[10\bar{1}]$ direction) are marked as $\gamma$, $\alpha$, $\beta$, respectively, and the central point of ABC [the (111) plane] is marked as $\delta$. Figure 6.2 (c) is a SEM micrograph showing one pyramidal TiAlN grain, where the three {001} facets are marked by the red, blue and purple used in the Q-H pyramid. The unfolded Q-H pyramid is shown in Figure 6.2 (d).

An intra-grain misorientation of the CVD TiAlN grains is discussed in Paper IV. The Q-H pyramid is very useful for correlating rotation axes (of the intra-grain misorientation), to the geometries of relevant dislocation lines and Burgers vectors, as will be shown in Sections 6.1.7 and 6.1.8.
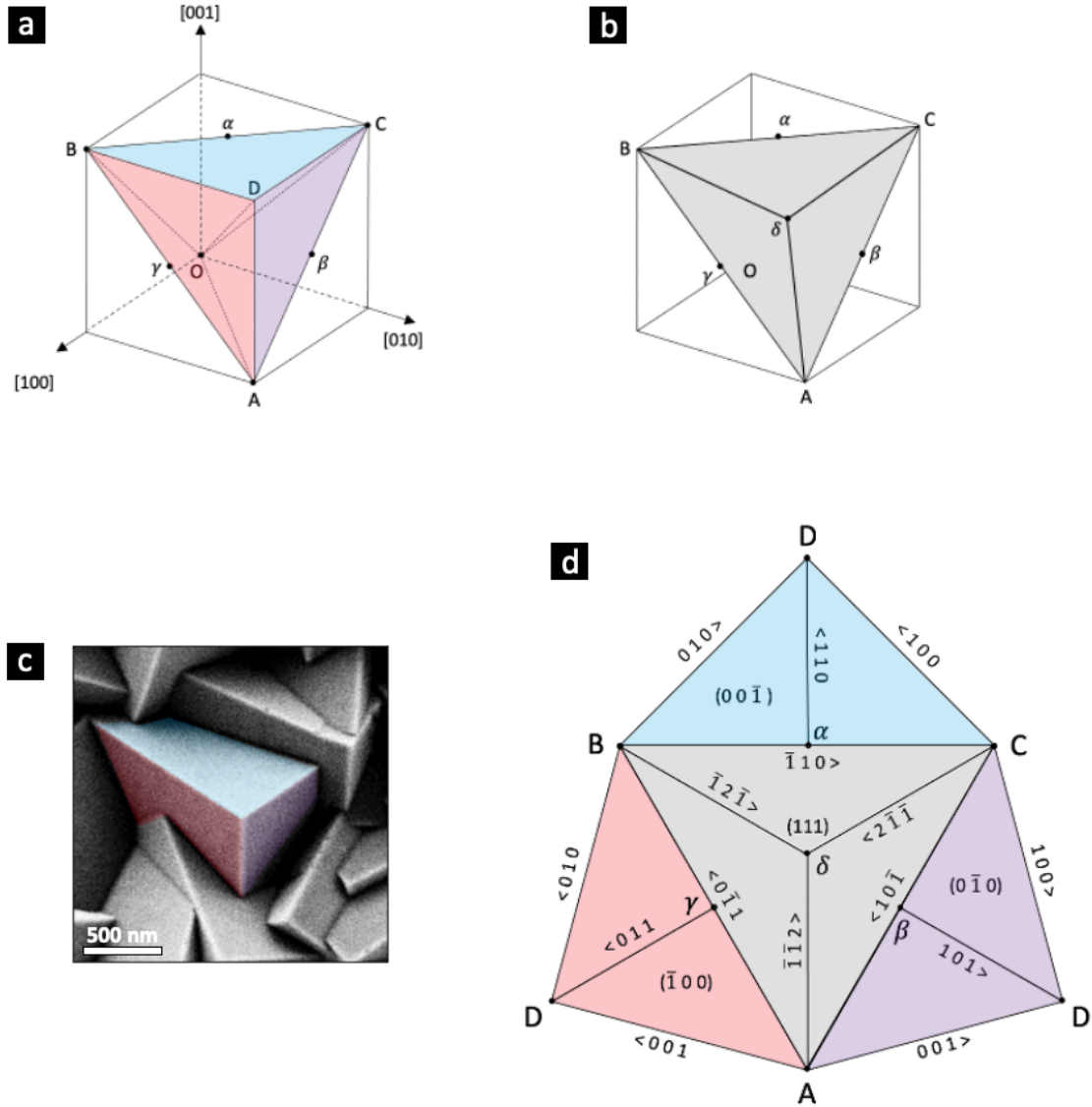
Figure 6.2. Construction of the Q-H pyramid. (a) The three {001} facets are illustrated in the cubic unit cell, and are colored red (ADB), blue (BDC), and purple (ADC), respectively. (b) The (111) plane (ABC) is illustrated in the unit cell, and is colored gray. (c) Plan view SEM micrograph of a pyramidal TiAlN grain, where three {001} facets are colored red, blue and purple. (d) The unfolded Q-H pyramid, where crystallographic directions and planes are illustrated. Reproduced from Paper IV.

### 6.1.3   CVD TiAlN nanolamella structure and rotating gas flow

Detailed microstructural studies revealed a nanolamella structure in the CVD TiAlN coatings, see Figure 6.3. The coating cross-section imaged by SEM with an in-lens SE detector is shown in Figure 6.3 (a), from which the columnar grains of the TiAlN coating were found to consist of periodic nano-structures (nanolamellae). The nanolamella structure was characterized at the atomic scale using HRSTEM HAADF imaging, as

shown in Figure 6.3 (b). According to the Z-contrast in the STEM HAADF image, the nanolamella structure was found to contain two types of lamellae, one with a higher Ti content (Ti(Al)N) that appears with brighter contrast, and one with a higher Al content (Al(Ti)N) that appears with darker contrast. The crystallographic orientation between the two types of nanolamella was revealed by fast Fourier transforms (FFTs) (see appended Papers I and II) of the high-resolution image to be:

$$(001)_{Ti(Al)N} \mathbin{//} (001)_{Al(Ti)N}, \; [010]_{Ti(Al)N} \mathbin{//} [010]_{Al(Ti)N}.$$

This shows that the Ti(Al)N and the Al(Ti)N nanolamellae grow epitaxially along the <001> direction, and the nanolamella interfaces are {001} planes. The nanolamella planes are the same as the pyramidal facets. The 3D arrangement of the nanolamellae is shown in Figure 6.3 (c). Each domain below the {001} facets of the pyramidal grain corresponds to a series of epitaxially grown nanolamellae. Previously reported density functional theory (DFT) simulations of TiAlN indicate a noticeably lower surface energy of the {001} planes compared to the {111} and {110} planes [136]. This could be (at least partly) responsible for the formation of the nanolamellae and facets on the {001} planes.
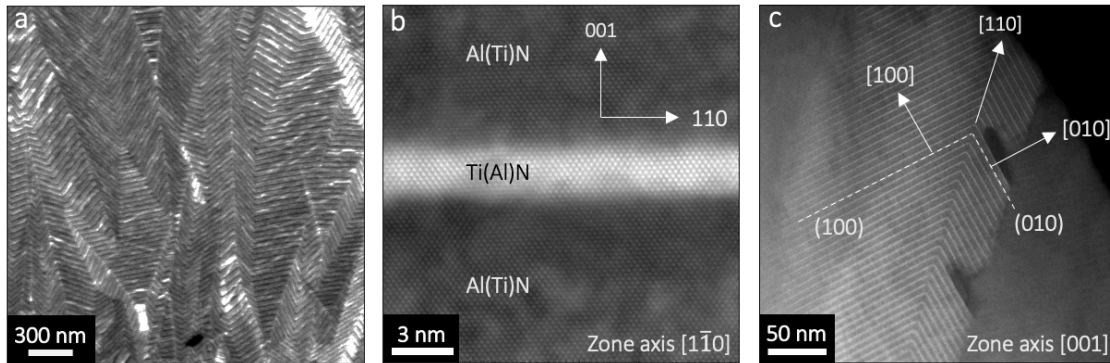


Figure 6.3. Nanolamella structure in the CVD TiAlN coatings. (a) SEM in-lens SE micrograph of the coating cross-section. (b) STEM HAADF micrograph of the coating cross-section, viewed along the $[1\bar{1}0]$ zone axis of the grain. (c) HRSTEM HAADF micrograph showing the interfacial structures between the Ti(Al)N and the Al(Ti)N nanolamellae, viewed along the [001] zone axis. Reproduced from Papers I and III.

As discussed in Paper I, the nanolamella structure is caused by the periodic variation of the local gas environment that is induced by the rotational supply of the precursor gas. As mentioned in Chapter 2, the incorporation of the Ti atoms into the cubic TiAlN phase is mainly controlled by mass transport of the precursors, and the incorporation of the Al atoms is limited by the kinetics of the surface reactions. A varying gas flow would, hence, influence the relative incorporation of Ti and Al into the TiAlN, and this would cause a

variation in the chemical composition. Figure 6.4 illustrates how a periodic variation in the local gas environment would cause the formation of the periodic Ti(Al)N and Al(Ti)N nanolamellae. As illustrated in Figure 6.4 (a), when the gas beam containing precursors is directed towards the samples, the local gas velocity is high. According to Equation 2.4, this improves the growth rate of the mass transport controlled deposition (the incorporation of the Ti atoms into the TiAlN), and thus increases the Ti content and creates a Ti(Al)N nanolamella. When the gas beam rotates away and does not hit the substrate directly, see Figure 6.4 (b), the local gas flow rate becomes lower, and thus an Al(Ti)N nanolamella with a relatively low Ti content forms. In addition, the angle $\beta$ (opening angle of the precursors gas beam) is much smaller than 360°- $\beta$, as indicated in Figures 6.4 (a) and (b). The gas beam will, thus, hit the substrate directly, or be in close enough proximity, to generate a sufficiently high local flow velocity during only a smaller part of each rotation cycle. The rotation cycle will be dominated by a lower local gas flow velocity (when the gas beam rotates away from the substrate). This would then produce the thinner Ti(Al)N nanolamellae and the thicker Al(Ti)N nanolamellae in Figure 6.4 (c).
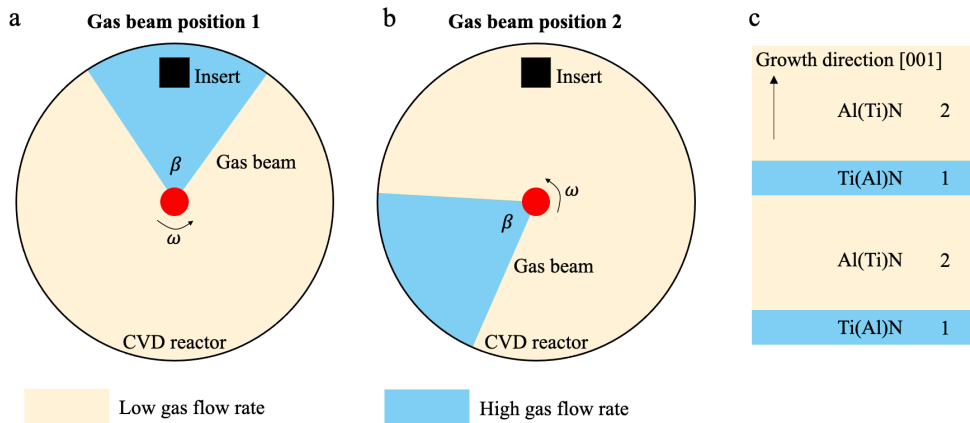


Figure 6.4. Schematics to explain the nanolamellae formation due to the rotational precursor gas supply. (a) Gas beam position 1: the precursor gas beam directly hits the substrate (the cutting tool insert) and causes a high local gas flow, creating a Ti(Al)N nanolamella. The angle $\beta$ is the opening range of the gas beam. (b) Gas beam position 2: the precursor gas beam rotates away and causes a low local gas flow, creating an Al(Ti)N nanolamella. (c) The Ti(Al)N and the Al(Ti)N nanolamellae grow along the [001] direction iteratively, corresponding to the gas beam positions 1 and 2, respectively. Reproduced from Paper I.

As illustrated above, each precursor gas rotation cycle creates one period of the nanolamellae, including one Al(Ti)N and one Ti(Al)N lamella. In addition, the TiAlN grains grow along the [111] direction, which has a given geometrical relationship with respect to the {001} facets (the pyramidal shape) formed by the nanolamellae. As shown in Paper I, one can thus correlate the periodicity of nanolamellae (the distance between

nanolamellae in the normal direction [001], $\lambda$, in $\mu$m) with the rotation frequency of the precursor gas supply $\omega$ (in rpm) and the coating growth rate $v$ (in $\mu$m/minute), as:

$$\frac{1}{\lambda} = \sqrt{3} \cdot \cos\alpha \cdot \frac{\omega}{v} \tag{6.1}$$

In equation 6.1, the factor $1/\sqrt{3}$ is a geometrical constant introduced due to the angle (54.7°) between the normal directions of the nanolamellae/facets (the <001> directions) and the grain growth direction [111]. The correction factor $\cos\alpha$ is introduced because of the inclination of the grain, where $\alpha$ is the angle between the grain growth direction (the [111] direction) and the coating growth direction (the normal to the substrate surface). The inclination angle $\alpha$ is usually small (< 20°), because the LPCVD TiAlN coatings have strong 111 texture, as can be measured in EBSD and XRD pole figures.

According to Equation 6.1, one can tune the periodicity of the nanolamella structure by simply varying the rotation speed/frequency of the precursor gas supply. With a higher gas rotation speed, the nanolamella periodicity gets shorter, while a lower gas rotation speed results in a longer periodicity. The periodicity is also influenced by the coating growth rate, which depends on factors such as the deposition temperature, pressure and local gas flow rate. The grain inclination angle ($\alpha$) also influences the nanolamella periodicity, but on a smaller scale, because the variation of the cosine function is negligible for low $\alpha$ values (< 20º).

### 6.1.4  Chemical composition of the nanolamella structured TiAlN

As revealed above, the nanolamella structure contains epitaxially grown Ti(Al)N and Al(Ti)N lamellae, and the separation of the Ti and Al is due to the periodically rotating precursor gas supply. The Ti and the Al contents in the two types of nanolamellae were measured using XEDS in STEM mode. Figure 6.5 shows the variation of the Al and Ti contents along the normal direction (the [001] direction) of the nanolamellae. The Al(Ti)N lamellae have an Al to Ti ratio of around 90/10, and the Ti(Al)N lamellae have an Al to Ti ratio of around 50/50. However, the STEM XEDS has some disadvantages when determining chemical contents. First, the N content cannot be determined due to the overlap of the N $K_\alpha$ (392 eV) peak with the Ti $L_\alpha$ (452 eV) peak and the limited energy resolution of XEDS (~ 130 eV). Second, the chemical content determined by STEM XEDS is influenced by the beam broadening effect (see Section 4.6.7).
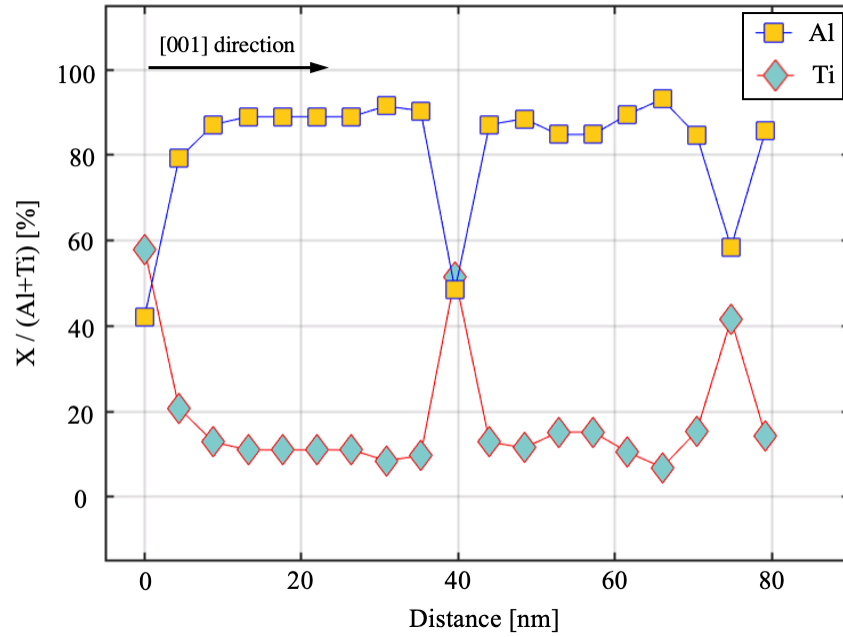
Figure 6.5. STEM XEDS results showing the variation of the Al and Ti content along the normal direction of the nanolamella structure (the [001] direction). The Al and the Ti values are in at.%. Reproduced from Paper I.

As shown in Paper III, APT was used to study the 3D variation in the chemical content of all major elements (Al, Ti and N) in the nanolamella TiAlN. Figures 6.6 (a) and (b) are 3D reconstructions of the Al atoms (red) overlaid with Ti iso-concentration (15 at.%) surfaces (black). Figure 6.6 (a) is viewed along the [110] direction, and Figure 6.6 (b) is rotated by 90° and is viewed along the [001] direction. Figure 6.6 (c) is 1D concentration profiles of Al, Ti and N, determined from the data points within a cylinder that has a diameter of 10 nm, as indicated in Figures 6.6 (a) and (b).

The average chemical composition of the TiAlN coating was determined from the APT data, and corresponds to the chemical formula $(Ti_{0.17}Al_{0.83})N_{0.94}$, where the Al to Ti ratio is close to that determined by XEDS (Paper I). In addition, N is under-stoichiometric by 6 at.%. A variation of the N content is correlated to the Ti and Al contents. The chemical formula of the Al(Ti)N lamellae is $Ti_{0.12}Al_{0.88}N_{0.90}$, corresponding to a N under-stoichiometry of 10 at.% N vacancies (see Table 6.1). The Al to Ti ratio is 12/88, close to the 10/90 determined by STEM XEDS (see Figure 6.5). The chemical formula of the Ti(Al)N lamellae is $(Ti_{0.30}Al_{0.70})_{0.97}N$, corresponding to a N over-stoichiometry (under-stoichiometry of metals) with 3 at.% metal (Al and Ti) vacancies (see Table 6.1). The Al to Ti ratio of the Ti(Al)N lamellae is 30/70, which is lower than 50/50 as determined by STEM XEDS (see Figure 6.5). It is worth noting that an accurate determination of the chemical composition of the thin Ti(Al)N lamellae by STEM XEDS is difficult because of beam broadening (see Section 4.6.7). In addition, the chemical contents may also

fluctuate within the Ti(Al)N and Al(Ti)N nanolamellae, as seen in the discontinuous iso-concentration surfaces in Figures 6.6 (a) and (b).
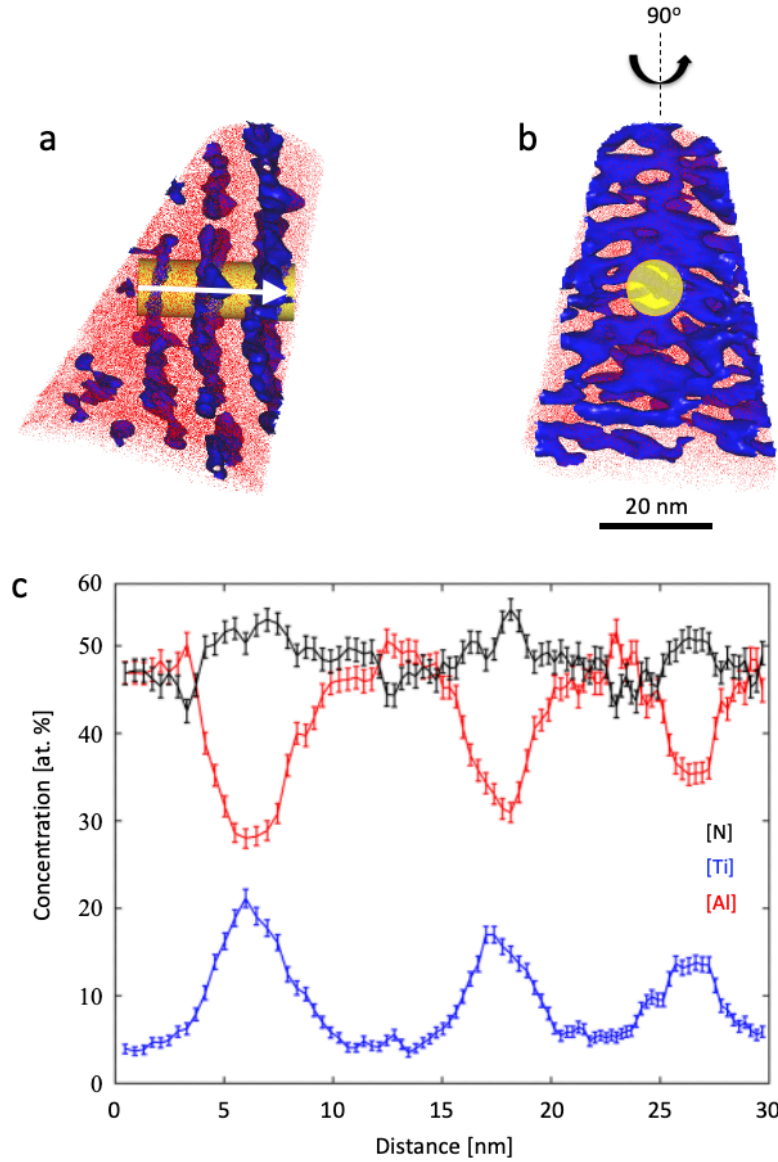


Figure 6.6. APT reconstruction of CVD TiAlN and the corresponding chemical composition analysis. (a) and (b) are 3D reconstruction by Al atoms (red dots) and the Ti iso-concentration surfaces (15 at.%) viewed along orientations (out of paper) that are perpendicular (a) and parallel (b) to the [001] direction, respectively. The cylinder used for calculating the 1D concentration profiles is shown in (a) and (b). (c) 1D concentration profiles of Ti, Al and N (along the direction marked by arrow in (a)). Reproduced from Paper III.

Table 6.1. Summary of chemical compositions obtained by APT. Reproduced from Paper III.

|  | Al (at.%) | Ti (at.%) | N (at.%) | Formula |
|---|---|---|---|---|
| Bulk TiAlN | 42.6 | 8.90 | 48.5 | $(Ti_{0.17}Al_{0.83})N_{0.94}$ |
| Al(Ti)N | 46.3 | 6.3 | 47.4 | $Ti_{0.12}Al_{0.88}N_{0.90}$ |
| Ti(Al)N | 34.8 | 14.4 | 50.7 | $(Ti_{0.30}Al_{0.70})_{0.97}N$ |
| Al-richest | 57.0 | 4.0 | 39.0 | $Ti_{0.07}Al_{0.93}N_{0.64}$ |
| Ti-richest | 34.0 | 13.0 | 53.0 | $(Ti_{0.72}Al_{0.28})_{0.88}N$ |
| Stoichiometric | 40.8 | 9.2 | 50 | $Ti_{0.18}Al_{0.82}N$ |

Due to the indicated fluctuation in the chemical composition within the Ti(Al)N and Al(Ti)N nanolamellae, it may not be accurate to evaluate the varying composition in the 3D structure by 1D concentration profiles (see Figure 6.6). In addition, statistical errors may affect the determined 1D profile because of low ion counts, due to the limited detection efficiency of the APT technique (~ 37 %), and the small cylinder volume (e.g. 10 nm in diameter) that is introduced in the reconstruction in order to create a 1D profile [137]. Complementary to the 1D concentration profiles, the chemical compositions were also analyzed using proximity histograms (proxigrams). A proxigram calculates the composition as a function of distance from an iso-concentration surface of a given chemical content. The advantages of proxigrams include independence of the complex interfacial morphology, and a lower statistical error due to a larger analysis volume [137].

Figures 6.7 shows two proxigrams across iso-concentration surfaces with chemical compositions of 50 at.% Al (a) and 15 at.% Ti (b). As shown in Figure 6.7 (a), the Al content increases (the Ti content decreases correspondingly) towards the centre of the Al(Ti)N lamellae (marked by red background and referred to as the Al richest area). The chemical content of the Al richest areas corresponds to the chemical formula $(Ti_{0.07}Al_{0.93})N_{0.64}$ (see Table 6.1), which means an N under-stoichiometry of 34 %. As shown in Figure 6.7 (b), the Ti content increases (the Al content decreases) towards the center of the Ti(Al)N lamellae (marked by blue background and referred to as the Ti richest area). The chemical content of the Ti-richest areas corresponds to the chemical formula $(Ti_{0.72}Al_{0.28})_{0.88}N$ (see Table 6.1), which agrees with 12 % vacancies on the metal (Al and Ti) sites. It is apparent, particularly in Figure 6.7 (a), that the N concentration increases with a higher Ti content (and a lower Al content). The N stoichiometric region is marked by the gray background (referred to as Stoichiometric) in Figure 6.7 (a), and corresponds to the chemical formula $(Ti_{0.18}Al_{0.82})N$ (Table 6.1). This formula is close to the average TiAlN composition (denoted as 'Bulk TiAlN' in Table 6.1). More details on the analysis of chemical composition are presented in Paper III.
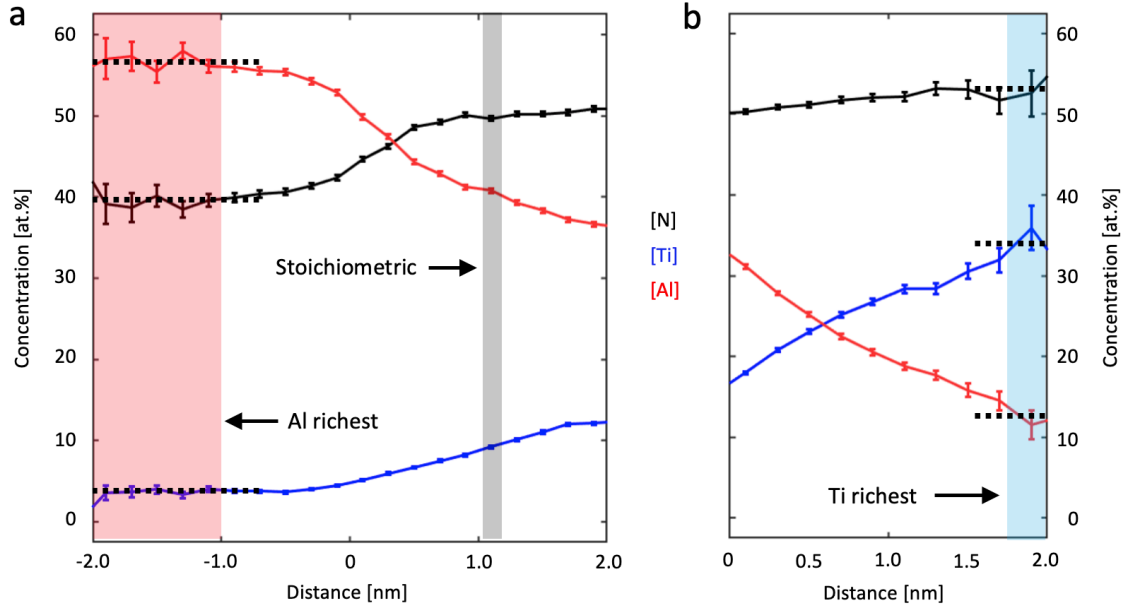
Figure 6.7. (a) Proxigram calculated across the 50 at.% Al iso-concentration surfaces. (b) Proxigram calculated across the 15 at. % Ti iso-concentration surfaces. "Distance" is the distance from the iso-concentration surface. The Al-richest and Ti-richest volumes are marked with red and blue background in (a) and (b), respectively. The chemical compositions of the Ti-richest and Al-riches regions are approximated by the heights of plateaus marked by dotted lines. The N stoichiometric region is marked by the gray background in (a). Redrawn from data from Paper III.

### *6.1.5   Co-growth of the h-AlN and cubic TiAlN phases*

There is a co-growth of h-AlN and cubic TiAlN in the investigated CVD TiAlN coatings. The h-AlN phase is found to exist in two different types of grain/crystal boundaries, see Figure 6.8 (a): *(i)* as thin films in the grain boundaries between TiAlN grains; *(ii)* as thin films in the boundaries between the three {001} faceted domains within a TiAlN grain (the {1$\bar{1}$0} planes). The h-AlN phase is also found to exist as domains within the TiAlN grains, see Figures 6.8 (b) and (c). It is worth noting that the intra-grain h-AlN domains start to grow on the (001) plane of the Ti(Al)N lamellae. The orientation relationship between the intra-grain h-AlN domain and the cubic TiAlN phases were studied via HRSTEM HAADF imaging, see Figure 6.8 (c), and associated 2D FFT, see Figure 6.8 (d).
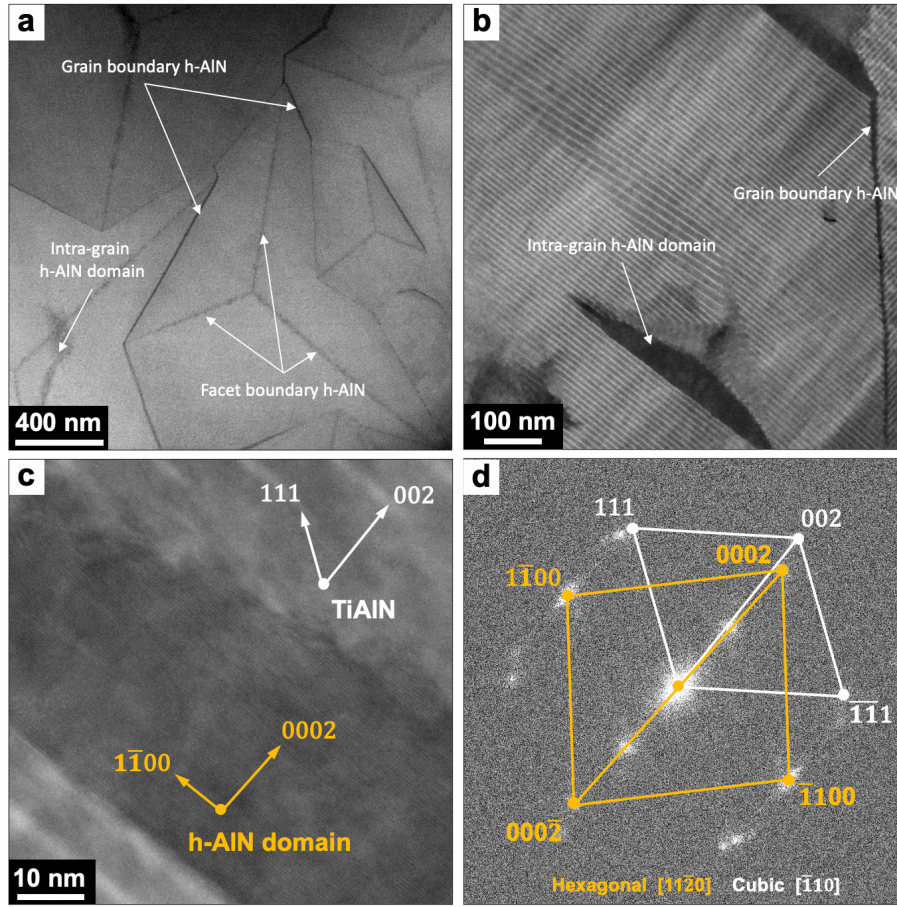
Figure 6.8. Co-growth of h-AlN phase with the cubic TiAlN phase. (a) Plan view STEM HAADF micrograph. (b) Cross-section STEM HAADF micrograph. (c) HRSTEM HAADF micrograph of the intra-grain domain h-AlN phase co-grown with the cubic TiAlN phase. (d) FFT calculated based on (c). Reproduced from Paper II.

The orientation relationship between the intra-grain h-AlN domain and the cubic TiAlN grain is:

$$\{001\}_{TiAlN} \; // \; (0001)_{h\text{-}AlN} \text{ and } <\bar{1}10>_{TiAlN} \; // \; <11\bar{2}0>_{h\text{-}AlN}$$

In addition, h-AlN existing at the grain boundaries (the *(ii)* type) was also found to co-grow with the TiAlN grains with the same orientation relationship as that followed by intra-grain h-AlN domains, as reported in Paper II. However, h-AlN growing along the boundaries between domains of {001} facets (the *(i)* type), which is the ($\bar{1}$10), ($\bar{1}$01) and (0$\bar{1}$1) planes of the TiAlN phase, follows a different orientation relationship with the TiAlN (see Figure 6.9):

$$\{111\}_{TiAlN} \; // \; (0001)_{h\text{-}AlN} \text{ and } <\bar{1}10>_{TiAlN} \; // \; <11\bar{2}0>_{h\text{-}AlN}$$
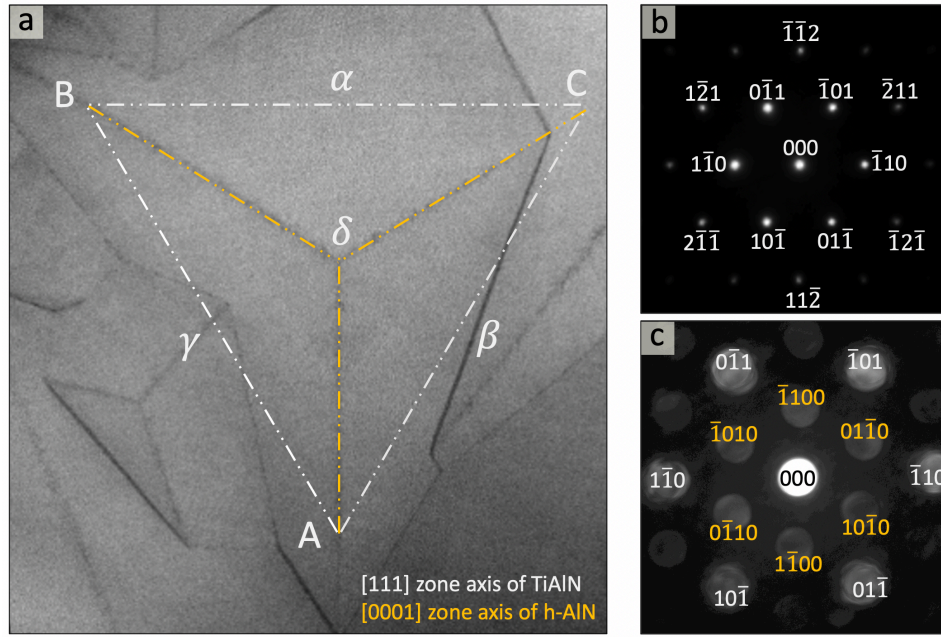
55

Figure 6.9. Crystallographic orientation relationship between the h-AlN phase co-growing on the boundaries between domains of the {001} facets and the cubic TiAlN phase. (a) Plan view STEM HAADF micrograph where the crystal orientation of the TiAlN phase is marked by the (111) plane of the Q-H pyramid. (b) SAED from the TiAlN grain (zone axis is [111]). (c) Convergent beam electron diffraction (CBED) pattern (zone axis is [111] for TiAlN and [0001] for h-AlN) obtained by positioning the electron probe with a small semi-convergence angle (0.5 ~ 1.0 mrad) on the TiAlN domain boundaries. Reproduced from Paper IV.

The mismatch between the TiAlN and the *(i)* type h-AlN was found to form threading dislocations in the three {001} TiAlN domains, as discussed in Paper IV. This will be further discussed in section 6.1.8.

### 6.1.6    Gas flow and microstructural inhomogeneity

As has been discussed in Section 6.1.3, the temporal variation of the local gas environment (induced by the rotating precursor gas supply) causes the nanolamella structure. The influence of a spatial variation of the gas flow rate on the microstructure of the TiAlN coatings is discussed in Paper II.

The local gas flow rates near a cutting tool insert placed in the CVD reactor are schematically illustrated by CFD simulations, as shown in Figure 6.10. Figure 6.10 (a) is a schematic drawing of the insert and an illustration of the geometry used in the CFD map. Figure 6.10 (b) is a snap shot of the simulated local gas flow velocities around the inserts placed at a certain location in the CVD reactor. The relative gas flow rate and the corresponding coating microstructures along the diagonal line of the rake face of the

cutting tool insert were studied in Paper II. The locations of the studied sites are denoted by the distance from the insert corner (along the diagonal line on the rake face), as indicated in Figures 6.10 (a) and (b). According to the CFD simulation, the gas flow rate on the rake face is higher at positions that are closer to the corner of the insert, and lower at positions that are further away from the corner. As has been argued (see Equation 2.4), areas with a higher local gas flow rate have a promoted mass transport compared to areas with a lower local gas flow rate. As reported in Paper II, this difference in the local mass transport causes inhomogeneities of the microstructure at various locations on the cutting tool insert.
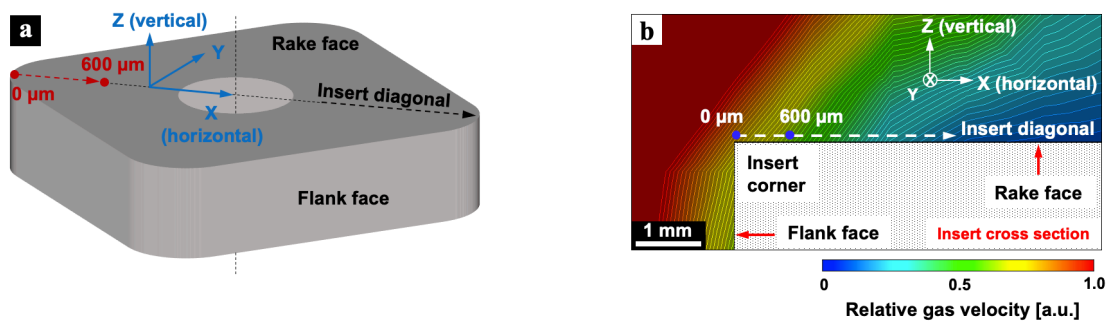


Figure 6.10. (a) Schematic drawing of a cutting tool insert and the coordinates used in the CFD gas flow velocity map in (b). (b) CFD map of relative gas flow velocity around one of the corners of the insert. Direction X is along the diagonal of the rake face. Z is perpendicular to the rake face and X. Y is the viewing direction (into the plane) of the CFD map, and is orthogonal to the X and Z directions. Reproduced from Paper II.

Figure 6.11 shows the spatial variation of the microstructure along the diagonal direction on the rake face, from the 0 $\mu m$ position to the 600 $\mu m$ position, as indicated in Figure 6.10. As shown in the cross-sectional SEM micrographs in Figure 6.11 (a), at positions away from the insert corner (500 µm), the coating contains columnar grains. However, the distortion of the grain structure increases towards the corner (250 µm and 100 µm) where the columnar grain morphology in the bottom of the coating disappears. At the insert corner (0 µm) the structure of the entire TiAlN coating cross-section is distorted and nearly no columnar grains can be identified. The spatial variation in the coating structure was found to be correlated to a spatial variation in the chemical composition of the coating, see Figure 6.11 (b). Near the coating bottom (the 250 nm height), the Al content is 82 at.% at positions away from the corner (600 $\mu m$), and the Ti content is 18 at.%, which is close to the average composition of the nanolamella structured TiAlN determined by APT (see Table 6.1). However, the Ti content increases towards the insert corner and reaches 42 at.% (with a corresponding 58 at.% Ti content). In addition, the chemical composition also varies along the coating growth direction (at different heights). At the insert corner, the Al content increases from 58 at.% at the 250 nm height to 76 at.%

(and the Ti content decreases from 42 at.% to 24 at.%) at the 3000 nm (3 µm) height. At positions away from the corner (with lower gas flow), the gradient of the chemical content decreases, and the entire coating have 82 at.% Al and 18 at.% Ti at the position that is 600 $\mu$m away from the corner.
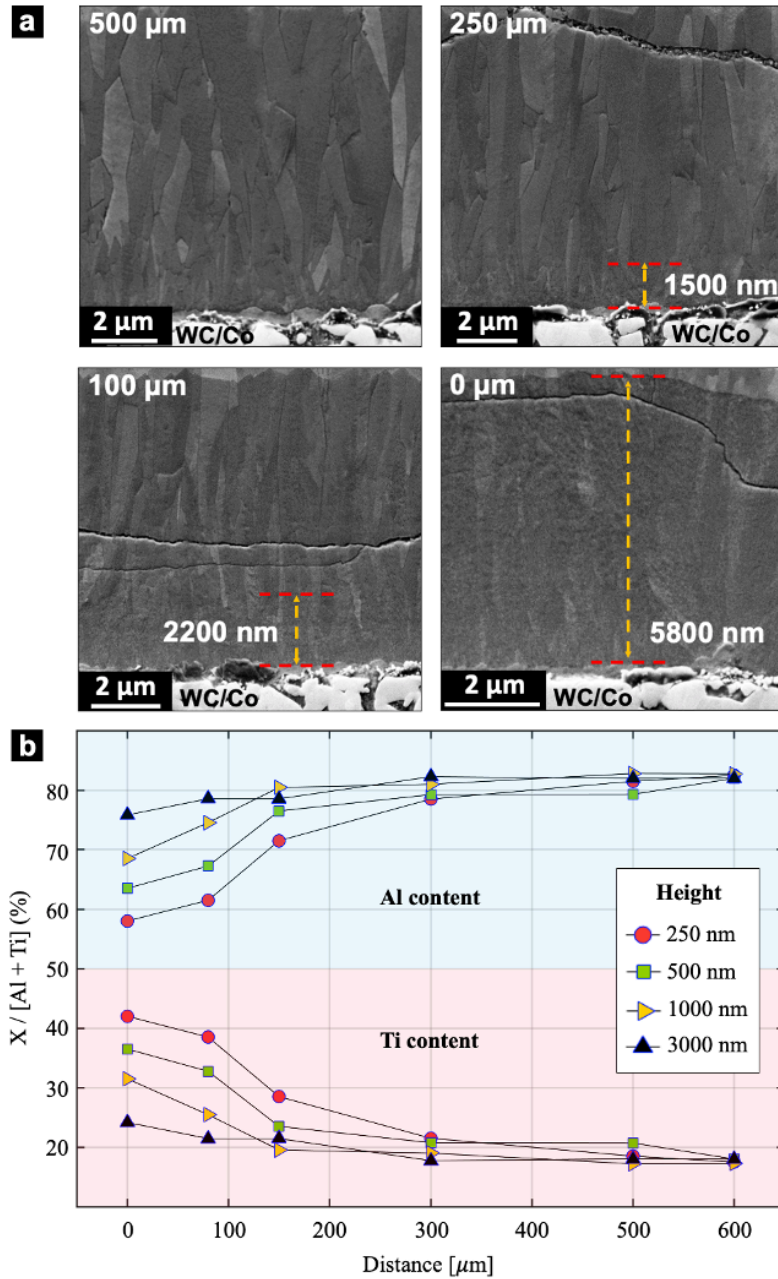


Figure 6.11. Microstructural inhomogeneity of the CVD TiAlN coatings. (a) Cross-sectional SEM SE micrographs acquired at places that are 500 $\mu$m, 250 $\mu$m, 100 $\mu$m and 0 $\mu$m from the insert corner where the gas flow velocities are simulated by CFD, as shown in Figure 6.9. (b) Variation of the Al to Ti ratio (in at.%) along the diagonal line of the rake face, at different hight of the TiAlN coating. Reproduced from Paper II.

To summarize, at positions with lower gas flow, the Ti content is lower (and the Al content is higher); at positions with higher gas flow, the Ti content is higher (and the Al content is lower). This compositional inhomogeneity is caused by differences in mass transport due to differences in local gas flow rate. When the local gas flow is low, a balance between the mass transport and the surface reaction kinetics creates an Al/Ti ratio close to 82/18. When the gas flow rate is higher, the mass transport of precursors increases, and thus the Ti deposition is promoted and creates a higher Ti content (and a lower Al content). In addition, the structural inhomogeneity is also correlated to the chemical content variation. With a high Al content (the Al/Ti ratio is 82/18), the coating has standard columnar grains and no structural distortions. With a low Al content and a high Ti content, the coating structure becomes distorted and the columnar grain morphology disappears. A possible reason for this is that a too high Ti content in the TiAlN phase promotes the formation of the h-AlN phase (due to the tendency of forming h-AlN on the Ti(Al)N lamellae, see Section 6.1.4), and thus distorts the microstructure of the nanolamella structured TiAlN.

### 6.1.7   Rotational growth of the TiAlN grains

The development of the misorientation angle in the CVD TiAlN grains is illustrated by the cross-sectional EBSD data shown in Figure 6.12. Figure 6.12 (a) is a misorientation map, where the value at each pixel is calculated with respect to the lowest pixel of the grain (reference pixel A). From the misorientation map and the corresponding scale bar, one can identify a uniform and continuous rotation along the grain growth direction (AB), presented in Figure 6.12 (b), measured along AB in Figure 6.12 (a). From the profile, one can identify an almost linear increase of the misorientation angle with the distance, which is found to be around $1°/\mu$m.

The rotation axis is determined from the EBSD pole figures, as illustrated in Figure 6.13. Figure 6.13 (a) is an inverse pole figure (IPF) map along the coating growth direction (Y direction). Figure 6.13 (b) is the colour legend for the IPF map, according to which the grain shown in Figure 6.13 (a) is 111 textured (blue). Figure 6.13 (c) shows the specimen coordinate system. Figure 6.13 (d) shows pole figures of the 001, 011, 111 and 112 reflections, viewed along the Y direction in the specimen frame. For crystals without any misorientation, all pixels in the EBSD map should be identical and correspond to a spot in the pole figures. However, the pole figures from the CVD TiAlN grains indicate a continuous rotation of the crystal. The rotation axis could be identified as one of the <011> directions that points close to the Z direction in the specimen frame (as marked by a red circle in the 011 pole figure in Figure 6.13 (d)). For this crystal orientation, all pixels in the grain correspond to a same orientation in the specimen frame. However, for other crystal orientations, there is a spread of corresponding orientations in the specimen frame.
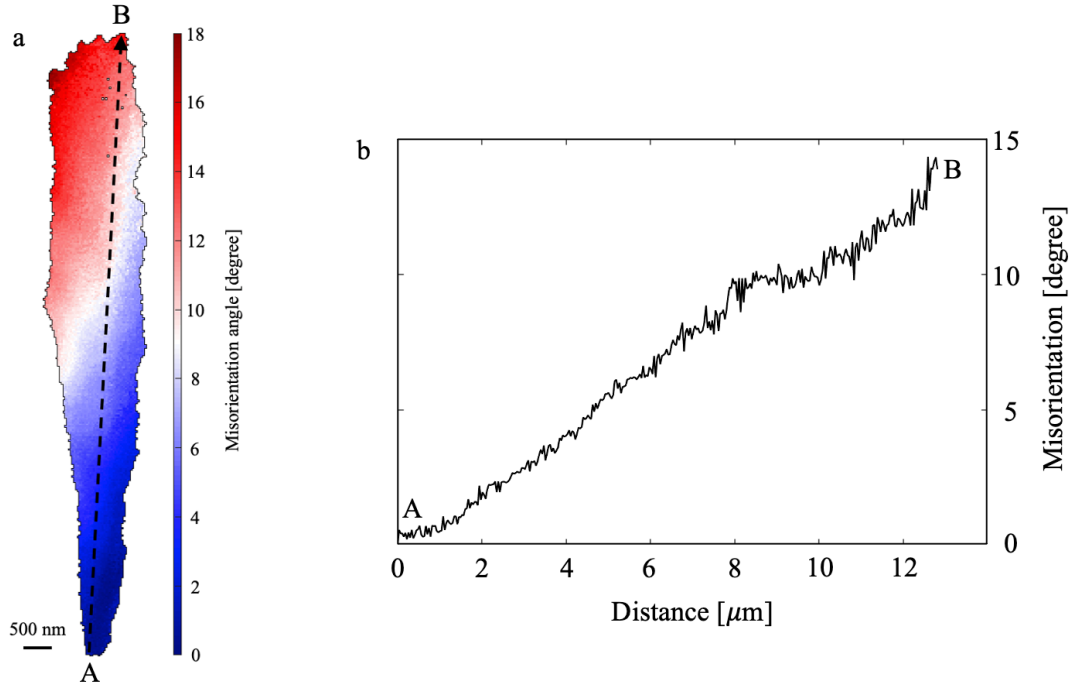
Figure 6.12. Intra-grain misorientation determined from a cross-sectional EBSD map of a CVD TiAlN grain. (a) The EBSD misorientation map. The misorientation value of each pixel is calculated with respect to the reference pixel A. (b) The misorientation profile along AB (indicated in (a)). Reproduced from Paper IV.

The crystal bending in 3D is also revealed by doing EBSD on a plan view section (the (111) plane) of the TiAlN grain, see Figure 6.14. According to the misorientation angle map shown in the Figure 6.14 (a), the misorientation develops from the centre of the TiAlN grain ($\delta$) towards its periphery, especially to the three corners (A, B and C), exhibiting a character of three-fold rotational symmetry around an axis parallel to the [111] direction. Figure 6.14 (b) is an IPF map of the grain cross-section for the coating growth direction (out of plane). Figure 6.14 (c) shows a 111 pole figure, and the vertical axis (out of paper) is aligned with the [111] direction. The $\delta$A, $\delta$B, $\delta$C, $\delta\alpha$, $\delta\beta$ and $\delta\gamma$ directions in the pole figure are aligned with respect to those in Figures 6.14 (a) and (b). Details of the vertical (111) reflection is shown in a magnified plot. The (111) reflection has a three-pointed star (the 'Mercedes star') shape, and the pixels at the three corners (A, B and C) have orientations that deviate the most, away from that of the center pixel ($\delta$). This is consistent with the results shown by the misorientation angle map. To analyze the misorientation as a function of positions in the plan view section, pixels in the pole figure corresponding to the positions A, B, C, $\alpha$, $\beta$, $\gamma$ and $\delta$ are marked as $P_A$, $P_B$, $P_C$, $P_\alpha$, $P_\beta$, $P_\gamma$ and $\delta$, respectively. Take the line $\delta$A as an example, the crystal orientation varies in the pole figure along a line $\delta P_A$ that is anti-parallel to $\delta$A. This means: when walking along the line $\delta$A, the (111) plane gradually rotates towards the centre of the plan view section ($\delta$), around an axis perpendicular to $\delta$A, within the (111) plane (the rotation axis is BC

60

for the line $\delta$A). The same phenomenon happens for all other lines from the cross-section centre ($\delta$) to its periphery, including the lines $\delta$B, $\delta$C, $\delta\alpha$, $\delta\beta$ and $\delta\gamma$, and is most obvious for the three corners (A, B and C).
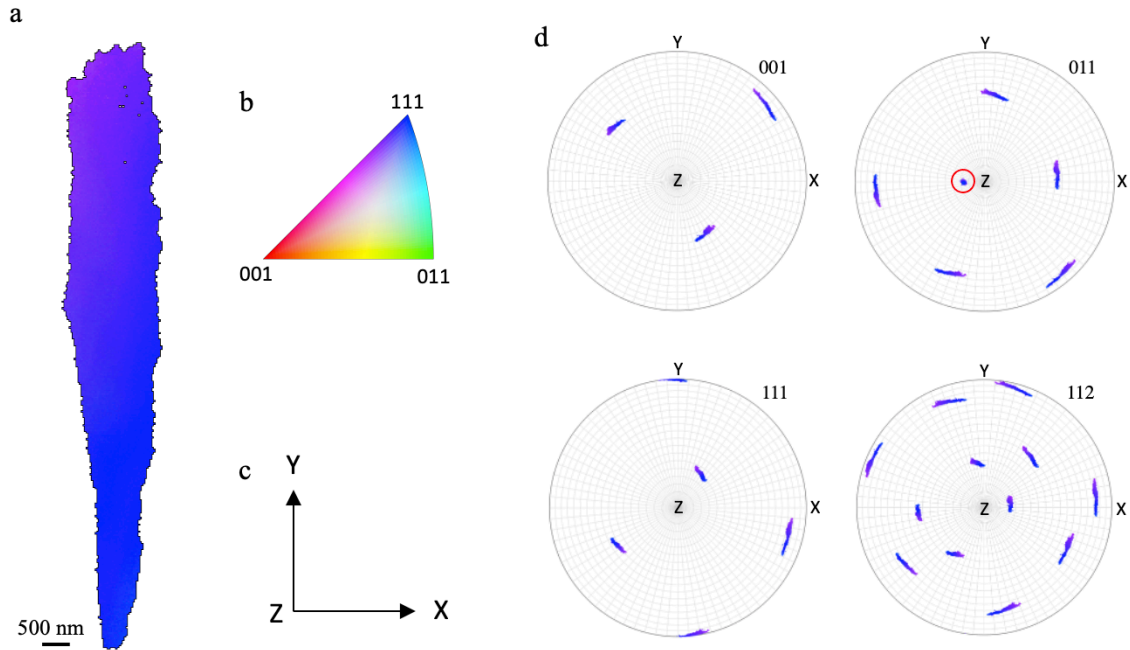


Figure 6.13. Analysis of the rotation axis of the intra-grain misorientation from a cross-sectional EBSD map of a CVD TiAlN grain. (a) The EBSD IPF map along the coating growth direction (Y). (b) Colour legend for the IPF map. (c) Axes of specimen frame. (d) Pole figures according to the 001, 011, 111 and 112 reflections, viewed along the Z direction in specimen frame. The rotation axis is marked by the red circle in (d). Reproduced from Paper IV.

The misorientation directions are shown in Figure 6.15. Figure 6.15 (a) is a map of the rotation axes causing the misorientation. It is obvious that the rotation axes at points on the lines from the grain centre to the three corners ($\delta$A, $\delta$B, and $\delta$C) are parallel to the BC, CA and AB directions, respectively, see Figure 6.15 (b). The $\delta$A, $\delta$B and $\delta$C lines thus appear green (the <110> orientations) in the rotation map. This is consistent with the phenomenon that the crystal rotates towards its opposite direction along these three lines as shown in Figure 6.14. This phenomenon also happens for the lines $\delta\alpha$, $\delta\beta$ and $\delta\gamma$. The rotation axes at points on the lines starting from the grain centre ($\delta$) running perpendicular to the $\delta$A, $\delta$B and $\delta$C directions, are parallel to the lines $\delta$A, $\delta$B and $\delta$C, respectively, and thus appear purple (the <112> orientations) in the rotation axis map. To summarize, along any line starting from the grain center and pointing to the grain periphery, the crystal rotates towards its opposite direction (towards the grain centre), with a rotation axis perpendicular to the line. This is illustrated in Figure 6.15 (b). The Figure 6.15 (c) is a notation to indicate the rotation axis and is used in Figure 6.15 (b).
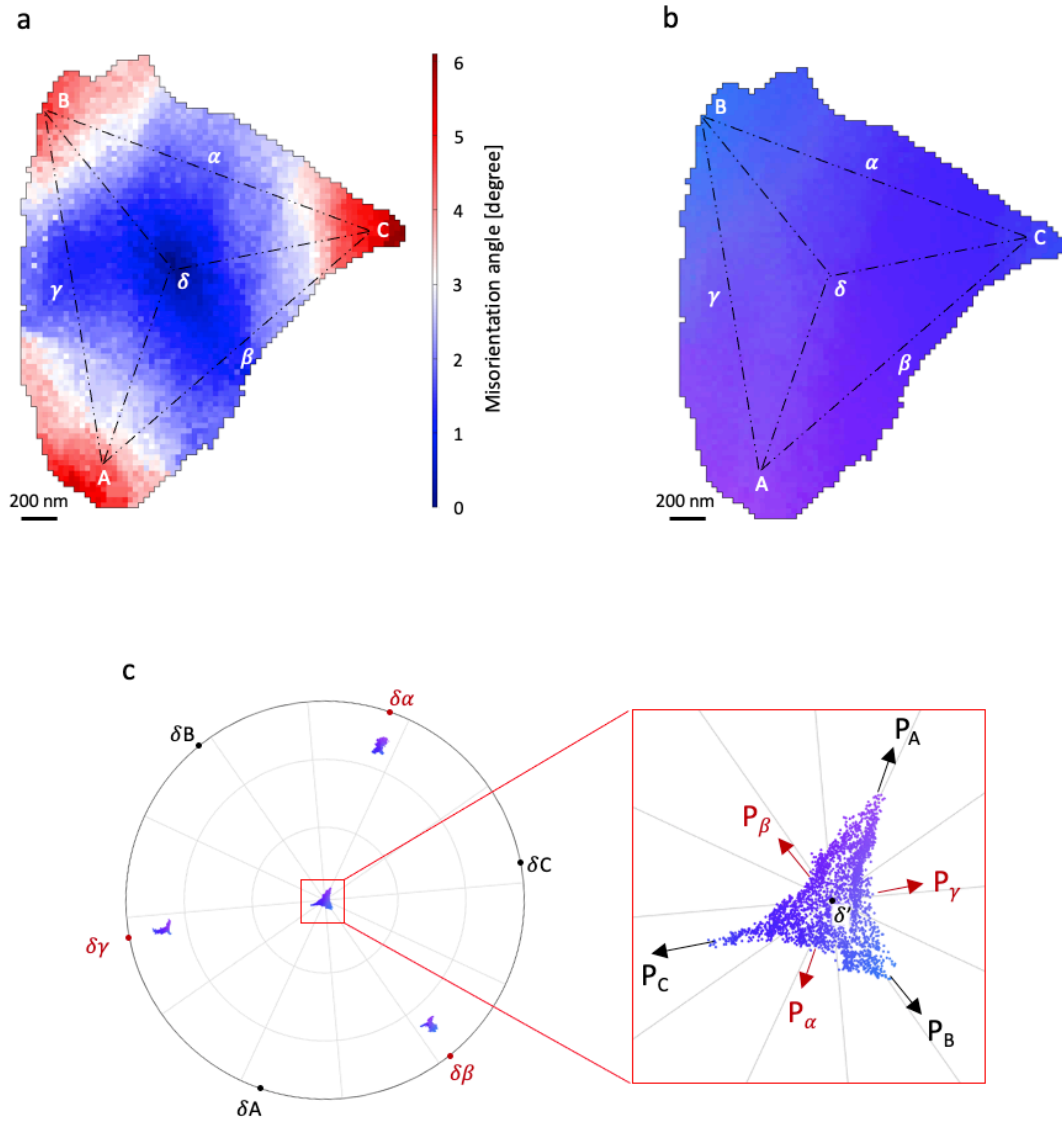
Figure 6.14. Plan view EBSD of the 111 textured TiAlN grain. (a) EBSD misorientation angle map, where the misorientation angle values are calculated with respect to the reference pixel in the center of the map, indicated by $\delta$ in the Q-H pyramid. (b) IPF map for the direction of coating growth (out of plane). The colour legend is the same as the one shown in Figure 6.13 (b). (c) 111 pole figure viewed along the [111] direction. The $\delta A$, $\delta B$ and $\delta C$ (in black), and $\delta\alpha$, $\delta\beta$ and $\delta\gamma$ (in red) directions are marked on the great circle of the [111] projection (left). The central {111} reflection is shown in the magnified plot (right). Pixels in the plan view EBSD map corresponding to the spots A, B, C, $\alpha$, $\beta$, $\gamma$ and $\delta$ in the Q-H pyramid (in real space), as shown in (a) and (b), are marked as $P_A$, $P_B$, $P_C$, $P_\alpha$, $P_\beta$, $P_\gamma$ and $\delta$, respectively. Reproduced from Paper IV.
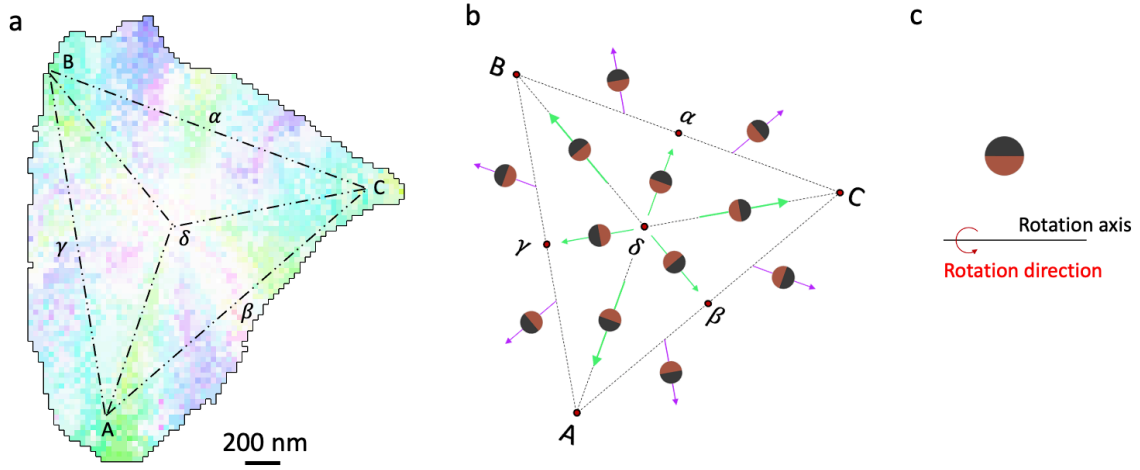
Figure 6.15. Crystal bending direction in plan view. (a) Misorientation rotation axis map from plan view EBSD. The colour legend is the same as that shown in Figure 6.13 (b). (b) Schematic of the rotation directions of the TiAlN grain, viewed along the [111] direction (out of paper). (c) Notation used in (b), indicating the axes of the grain rotation. Reproduced from Paper IV.

### 6.1.8    Threading dislocations in the TiAlN grains

The bending of the TiAlN crystal is caused by threading dislocations with high density that originate from the co-growing h-AlN phase (the *(ii)* type) in the boundaries between the domains below the {001} facets. As shown in Figure 6.16, in each of the {001} facet domains, there are four types of dislocation line directions (I, II, III and IV). In each facet, the dislocation lines keep a four-fold rotational symmetry around the facet normal, following directions of the <114> type that are close to, but tilted away from the normal by approximately 20º. Take the (001) facet (BδC) as an example, the four dislocation line directions (I, II, III and IV) are parallel to the [114], [$\bar{1}\bar{1}4$], [$\bar{1}14$] and [$1\bar{1}4$], respectively, although it is worth noting that from the [111] zone axis dislocation lines of types I and II are projected on top of each other and cannot be distinguished, see Figure 6.16 (a). For the other two domains (the (010) and (100) faceted domains), the orientation relationship between the dislocation lines and the corresponding facet normal is same as that of the (001) faceted domain. Figure 6.16 (b) is a 111 stereographic projection that illustrates the dislocation line directions in 3D with respect to the facet normal in each of the three {001} faceted domains.
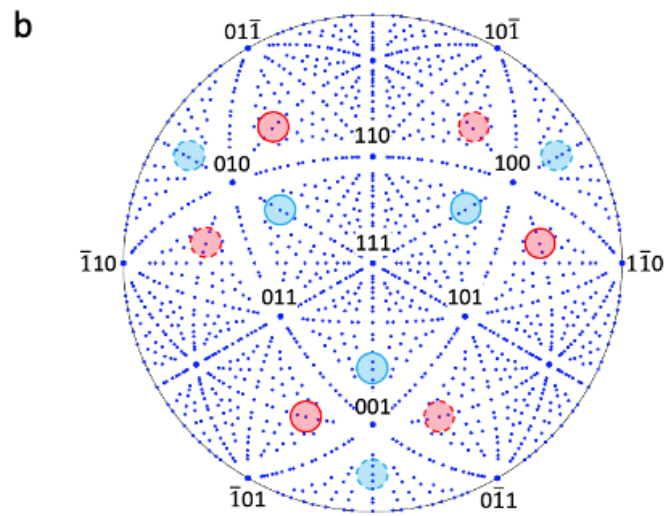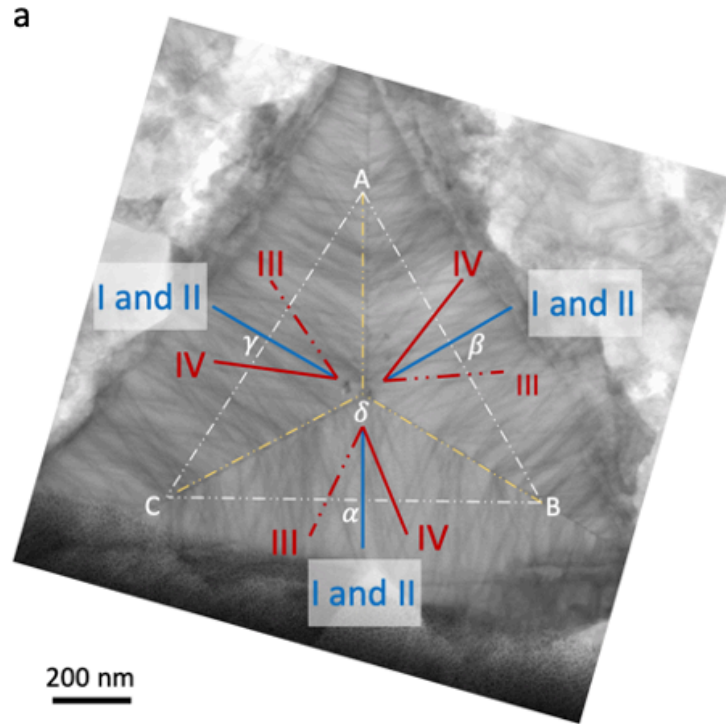
Figure 6.16. Threading dislocations in a TiAlN grain. (a) STEM BF plan view micrograph showing the projection of the dislocation lines (I, II, III and IV), viewed along the [111] direction. (b) The 111 stereographic projection, where the dislocation line directions in each of the {001} faceted domains are marked. Possible Burgers vectors are also given.

Burgers vectors in materials with the rock salt structure are of the **a**/2<110> type, where **a** is the lattice parameter of the crystal [138]. The orientation of possible Burgers vectors is shown in Figure 6.16 (b). Ignoring the sign of the **b**:s, there are six possible unique <110> directions. For simplicity, we take the (001) faceted domain (B$\delta$C) as an example to analyze the correlation between dislocation lines and **b**:s. In this domain, the six unique Burgers vectors are numbered as i ([$\bar{1}$10] (BC)), ii ([$\bar{1}$01] (AC)), iii ([0$\bar{1}$1] (AB)), iv ([110] ($\alpha$D)), v ([011] ($\gamma$D)) and vi ([101] ($\beta$D)). The types i, ii and iii Burgers vectors are within the (111) plane, while the types iv, v and vi stick out of this plane. The line directions and Burgers vectors of the threading dislocations in the (001) faceted domain are summarized in the list shown in Figure 6.16 (b). Based on a statistical analysis of the dislocations (in the (001) faceted domain), correlations between the dislocation line directions and the Burgers vectors were found:

- Most of the dislocations (more than 95%) have Burgers vectors within the (111) planes, and thus we focus on dislocations with Burgers vectors belonging to types i, ii and iii.

- The dislocations with lines of types I and II have almost the same amount of **b**:s belonging to each of the types i, ii and iii. For the types I and II dislocations, those with type i Burgers vectors are pure edge dislocations, and the rest (with type ii and iii Burgers vectors) are mixed dislocations, with both screw and edge components.

- The dislocations with lines of types III and IV only have Burgers vectors of types ii and iii, respectively. All of these dislocations are mixed dislocations.

The rotation of the LPCVD TiAlN grains can be linked to the high density of threading dislocations formed during growth. The pure edge threading dislocations (the types I-i and II-i) and the edge components of other dislocations can be considered to form a series of low angle grain boundaries that rotate the crystal continuously. In addition, two sets of perpendicular screw dislocations can cause a rotation of the crystal, resulting in a twist boundary. However, in the TiAlN case, considering the screw components of the types III and IV dislocations that form a 40° angle with respect to each other would cause both a crystal rotation and shearing. Combining the results for all edge and screw components of the observed dislocations, a model for the grain rotation phenomenon could be constructed, linking matrices of dislocations to a continuous lattice rotation, similar to rows of several low-angle grain boundaries. More details on the dislocation analysis and the model correlating the crystal bending to the threading dislocations are given in Paper IV.

## 6.2 *Microstructure of CVD TiN coatings on a FeCrCoNi substrate*

The microstructures of TiN coatings deposited on a CoCrFeNi MPEA substrate were studied in order to evaluate the possibility of coating such substrates by CVD at high temperatures and in a corrosive environment. This is discussed in the appended Paper V. Figure 6.17 shows cross-sections of TiN coatings deposited on CoCrFeNi MPEA substrates at 950 °C. Figures 6.17 (a) and (b) show the coating microstructure in the vicinity of the interface between the TiN coating and the substrate. There is no severe etching of the CoCrFeNi substrate, although 950 °C was the highest deposition temperature in this study. This indicates that the CoCrFeNi MPEA is capable to withstand the corrosive gas environment during the CVD process. Mainly equiaxed grains are present in the bottom part of the coating. However, as shown in Figure 6.17 (c), columnar grains develop and become dominant when the coating thickness increases.
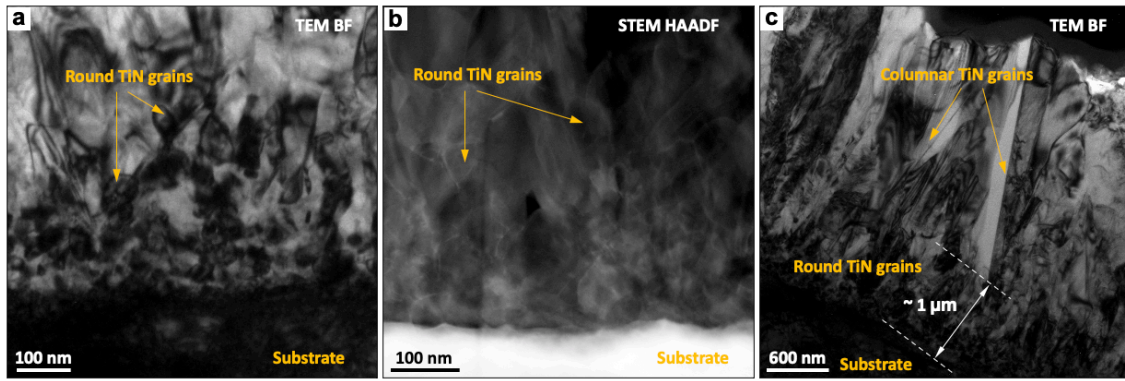


Figure. 6.17. TEM BF imaging from CVD TiN coatings deposited on the CoCrFeNi MPEA at 950 °C. (a) Bottom of the coating. (b) The whole cross-section of the coating. Reproduced from Paper V.

Possible etching effects of the CoCrFeNi substrate was further studied by STEM XEDS, as shown in Figure 6.18. According to the STEM HAADF micrograph in Figure 6.17 (a) and (b), the boundaries between the TiN grains have a brighter Z-contrast, which implies an aggregation of heavier elements in these boundaries. This is confirmed by STEM XEDS analysis, see inserted XEDS map of Cr in Figure 6.18 (a), and a STEM XEDS linescan along a TiN/TiN grain boundary shown in Figures 6.18 (b) and (c). These observations show that there was a transport of Cr from the MPEA substrate into the TiN coating, and that this transport took place through diffusion via the TiN/TiN grain boundaries. As a result, the substrate became depleted in Cr.

A driving force for the observed Cr diffusion was suggested by thermodynamic calculations in Paper V. Cr containing nitride phases may form due to the N-rich gas

environment during the CVD process. As shown in Figures 6.18 (d) and (e), the diffusing Cr aggregated on the surface of the TiN coating. In paper V, this Cr enrichment was suggested to be due to a continuous accumulation of Cr at the coating surface in the N-rich gas environment, during cooling from the process temperature after CVD synthesis.
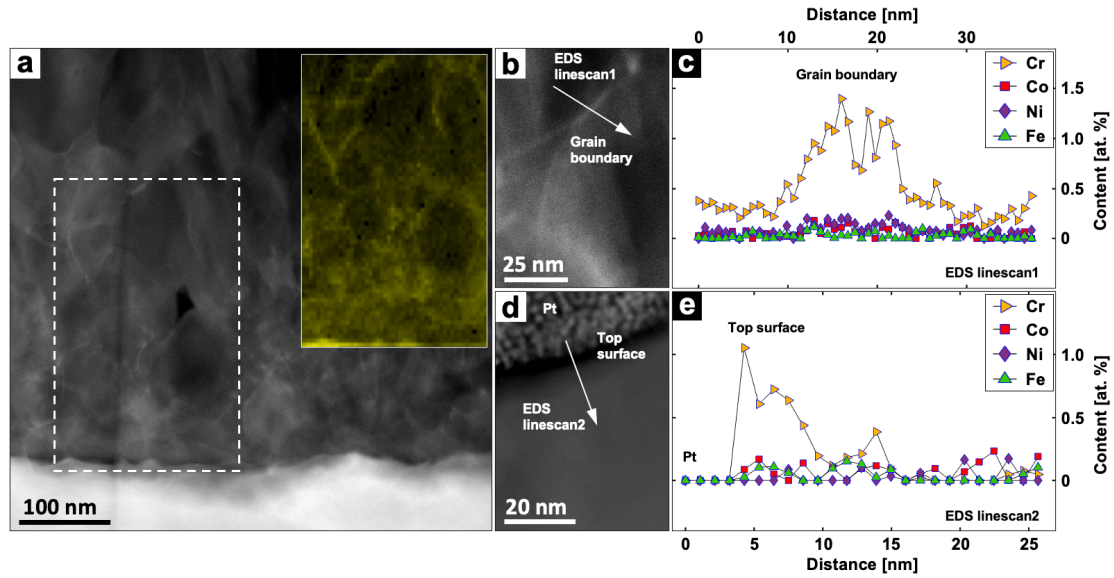


Figure 6.18. STEM XEDS analysis of a TiN coating deposited on a CoCrFeNi MPEA substrate at 950 ºC. (a) STEM HAADF imaging of the coating cross-section close to the interface with the substrate. The inserted XEDS map of Cr comes from the dashed area. (b) and (c) STEM HAADF imaging and XEDS analysis of boundaries between TiN grains. (d) and (e) STEM HAADF imaging and XEDS analysis of the upper part of the TiN coating. Reproduced from Paper V.

To summarize, the CoCrFeNi MPEA substrate could withstand the corrosive gas environment during the CVD process, and severe etching of the substrate was not observed. The substrate was, however, slightly depleted in Cr, which diffused through the TiN grain boundaries towards the coating surface.

## 6.3 Microstructure of LPCVD WN coatings

The microstructures of WN coatings, produced by LPCVD at different temperatures (592 K, 740 K, 789 K and 887 K) and with an excess amount of $NH_3$ with respect to the $WF_6$, were studied in Paper VI.

The WN coating deposited at 592 K had an amorphous structure. The coatings deposited at temperatures above the 740 K contained mainly the crystalline $\beta$-$WN_x$ rock salt phase, although the grain morphology depended on the deposition temperature.

The $\beta$-$WN_x$ grains were polycrystalline and of nanometer size in the WN coating deposited at 740 K. The grain size increased with elevated deposition temperature. A columnar morphology, following a 211 growth texture, appeared at 887 K.

The chemical compositions of the crystalline WN coatings were studied, and the determined atomic ratio between N and W varied between 1.6 to 1.8. This ratio was not clearly influenced by the deposition temperature, or by the partial pressures of $NH_3$ or $WF_6$. This implies that instead of forming an FCC sublattice of N atoms with 50% vacant sites, as suggested by references [77,80,81], the LPCVD $\beta$-$WN_x$ phase forms a sublattice of W atoms with metal vacancies. This would be a more stable $\beta$-$WN_x$ structure as proposed by DFT simulations by Mehl *et al.* [86].

# 7 Outlook

Based on the results from the microstructural studies of the CVD TiN, TiAlN and WN coatings obtained in this work, there are some research topics that would be of interest to address in future investigations.

## 7.1 The nanolamella structure and properties of the TiAlN coatings

The influence of a rotating precursor gas flow on the nanolamella structure of LPCVD TiAlN coatings has been studied in the present work. A gas rotating cycle was found to produce one nanolamella period, containing one Al(Ti)N lamella and one Ti(Al)N lamella. A lower gas rotating speed resulted in an increased nanolamella spacing. However, it was mainly the thickness of the Al(Ti)N lamellae that increased, while the thickness of the Ti(Al)N lamella did not. Thus, research remains to be done in order to explore how to vary the thickness of the Ti(Al)N lamellae through different precursor supply strategies, such as varying the opening angle of the precursor gas beam ejected from the gas inlet.

The chemical compositions of the TiAlN coatings were studied systematically in this work using XEDS and APT. However, considering the limitations of these methods, it would be worth trying to validate the results using other techniques, such as time of flight (TOF) – elastic recoil detection analysis (ERDA), at least on a macroscopic scale. The Al and Ti contents of both the Ti(Al)N and Al(Ti)N lamellae were not influenced by the nanolamella periodicity, according to our XEDS results. However, the influence of the nanolamella structure on the N content was studied. This may be done by APT measurements on TiAlN coatings with different nanolamella periodicities.

In addition, knowledge of the influence of the nanolamella periodicity on the properties of the TiAlN coatings, such as the mechanical properties (e.g. elastic modulus, hardness and hot hardness), thermal stability and residual stress, would be useful in optimizing the coating performance, and should be investigated systematically. The residual stress in the TiAlN coatings can be studied using synchrotron XRD, where the lattice straining at different heights of the coating can be analyzed using the obtained diffraction patterns. The phase transformation during annealing (decomposition of TiAlN into TiN and AlN) is expected to vary with the height in the coating, and can also be influenced by composition gradients and stress levels. The phase transformation after annealing can also be studied by synchrotron XRD, where the phase content can be analyzed according to the diffraction patterns.

## 7.2 Dislocations in CVD grown grains

In this work, threading dislocations in the pyramidal TiAlN grains were studied. The dislocation line directions and the Burgers vectors were determined. However, the Burgers vectors of these threading dislocation mainly have orientations in the base (111) plane of the TiAlN grain. This could be due to a specific mismatch between h-AlN and

TiAlN at the domain boundaries, which would be worth studying in more detail in the future. In addition, there are four sets of dislocation lines in each TiAlN domain, and a correlation between dislocation line direction and the Burgers vectors was identified. The underlying reasons for these phenomena are still unclear, and more research would be needed to better understand these observations.

In addition, it would be interesting to study the dislocations, especially the threading dislocations, in other types of CVD coatings that have a certain growth texture (such as TiN, WN, TiCN and alumina). The influence of the dislocations on coating growth, especially on a possible crystal bending phenomenon, as observed in the investigated LPCVD TiAlN coatings, would be interesting.

## 7.3 Facets of CVD grains

The growth facets of the 111 textured LPCVD TiAlN grains were determined to be three {001} planes, according to the special geometries of the internal nanolamella structure with known normal directions (the <001> directions) and the pyramidal shape of the TiAlN grain. However, the growth facets of other types of coatings, such as TiCN, TiN, WN and alumina, are difficult to determine. Knowing these facets would help to understand the growth of the CVD coatings. Therefore, a general method to determine the facets of grains in CVD thin films (with or without growth texture) should be developed.

A possible solution is to combine EBSD with SEM imaging from different angles. First, EBSD can be used to determine the growth direction of the grain of interest with respect to the specimen coordinate. Second, a stereographic imaging method can be used to build a 3D shape of the grain, including the angles between the facets. Thus, the crystal planes of the facets can be solved mathematically using EBSD and the results from stereographic imaging.

# Acknowledgements

# References

[1] J.M. Rodríguez, P. Jonsén, A. Svoboda, Simulation of metal cutting using the particle finite-element method and a physically based plasticity model, Comput. Part. Mech. 4 (2017) 35–51.

[2] I. El Azhari, J. Barrirero, J. García, F. Soldera, L. Llanes, F. Mücklich, Atom probe tomography investigations on grain boundary segregation in polycrystalline Ti(C,N) and Zr(C,N) CVD coatings, Scr. Mater. 162 (2019) 335–340.

[3] Cutting tool materials - Mitsubishi Materials Metalworkings Solutions Company. Retrieved 2021-03-19, (n.d.).
http://www.mitsubishicarbide.com/en/technical_information/tec_other_data/tec_other_data_top/tec_other_data_technical/tec_cutting_tool_materials.

[4] J.J. Gracio, Q.H. Fan, J.C. Madaleno, Diamond growth by chemical vapour deposition, J. Phys. D. Appl. Phys. 43 (2010) 374017.

[5] J. Sheikh-Ahmad, J.P. Davim, Tool wear in machining processes for composites, in: Mach. Technol. Compos. Mater. - Princ. Pract., Woodhead Publishing Limited, Cambridge, 2012: pp. 116–153.

[6] S. Canovic, B. Ljungberg, C. Björmander, M. Halvarsson, CVD TiC/alumina and TiN/alumina multilayer coatings grown on sapphire single crystals, Int. J. Refract. Met. Hard Mater. 28 (2010) 163–173.

[7] M.H. Staia, E.S. Puchi, D.B. Lewis, J. Cawley, D. Morel, Microstructural characterization of chemically vapor deposited TiN coating, Surf. Coatings Technol. 86–87 (1996) 432–437.

[8] L. von Fieandt, K. Johansson, T. Larsson, M. Boman, E. Lindahl, On the growth, orientation and hardness of chemical vapor deposited Ti(C,N), Thin Solid Films. 645 (2018) 19–26.

[9] J. Zalesak, D. Holec, I. Matko, M. Petrenec, B. Sartory, N. Koutná, R. Daniel, R. Pitonak, J. Keckes, Peculiarity of self-assembled cubic nanolamellae in the TiN/AlN system: Epitaxial self-stabilization by element deficiency/excess, Acta Mater. 131 (2017) 391–399.

[10] I. Yonenaga, A. Nikolaev, Y. Melnik, V. Dmitriev, High-temperature hardness of bulk single-crystal AlN, Jpn. J. Appl. Phys. 40 (2001) L426–L427.

[11] X.H. Ji, S.P. Lau, G.Q. Yu, W.H. Zhong, B.K. Tay, Structural properties and nanoindentation of AlN films by a filtered cathodic vacuum arc at low temperature, J. Phys. D. Appl. Phys. 37 (2004) 1472–1477.

[12] M. Lee, High temperature hardness of tungsten carbide, Metall. Trans. A. 14 (1983) 1625–1629.

[13]  C.P. Alpert, H.M. Chan, S.J. Bennison, B. Lawn, Temperature dependence of hardness of alumina-based ceramics, J. Am. Ceram. Soc. 71 (1988) C-371-C-373.

[14]  S. PalDey, S.C. Deevi, Single layer and multilayer wear resistant coatings of (Ti,Al)N: a review, Mater. Sci. Eng. A. 342 (2003) 58–79.

[15]  D.-Y. Wang, C.-L. Chang, K.-W. Wong, Y.-W. Li, W.-Y. Ho, Improvement of the interfacial integrity of (Ti,Al)N hard coatings deposited on high speed steel cutting tools, Surf. Coatings Technol. 120–121 (1999) 388–394.

[16]  X. Jiang, J. Philip, W.J. Zhang, P. Hess, S. Matsumoto, Hardness and Young's modulus of high-quality cubic boron nitride films grown by chemical vapor deposition, J. Appl. Phys. 93 (2003) 1515–1519.

[17]  M. Ahlgren, H. Blomqvist, Influence of bias variation on residual stress and texture in TiAlN PVD coatings, Surf. Coatings Technol. 200 (2005) 157–160.

[18]  S. Ruppi, Influence of process conditions on the growth and texture of CVD alpha-alumina, Coatings. 10 (2020) 158.

[19]  S.J. Bull, A.M. Jones, Multilayer coatings for improved performance, Surf. Coatings Technol. 78 (1996) 173–184.

[20]  R. Qiu, Electron Microscopy Investigation of Detailed Microstructures of CVD TiAlN and TiN Coatings - Effects of Gas Flow and Substrate on Coating Microstructure, Licentiate thesis, Chalmers University of Technology, 2020.

[21]  W.A. Bryant, The fundamentals of chemical vapour deposition, J. Mater. Sci. 12 (1977) 1285–1306.

[22]  J. -E. Sundgren, H.T.G. Hentzell, A review of the present state of art in hard coatings grown from the vapor phase, J. Vac. Sci. Technol. A. 4 (1986) 2259–2279.

[23]  U. König, R. Tabersky, H. van den Berg, Research, development and performance of cemented carbide tools coated by plasma-activated chemical vapour deposition, Surf. Coatings Technol. 50 (1991) 57–62.

[24]  D.T. Quinto, A.T. Santhanam, P.C. Jindal, Mechanical properties, structure and performance of chemically vapor-deposited and physically vapor-deposited coated carbide tools, Mater. Sci. Eng. A. 105–106 (1988) 443–452.

[25]  H.E. Hintermann, Tribological and protective coatings by chemical vapour deposition, Thin Solid Films. 84 (1981) 215–243.

[26]  K.-H. Habig, G.M. zu Köcker, Possibilities of model wear testing for the preselection of hard coatings for cutting tools, Surf. Coatings Technol. 62 (1993) 428–437.

[27]  W. Schintlmeister, O. Pacher, Preparation and properties of hard-material layers for metal machining and jewelry, J. Vac. Sci. Technol. 12 (1975) 743–748.

[28] J.P. Chubb, J. Billingham, D.D. Hall, J.M. Walls, Comparison of wear behaviour of single- and multilayer coated carbide cutting tools, Met. Technol. 7 (1980) 293–299.

[29] K.K. Yee, Protective coatings for metals by chemical vapour deposition, Int. Met. Rev. 23 (1978) 19–42.

[30] B. Lux, R. Haubner, C. Wohlrab, Chemically vapour-deposited hard coatings: Applications and selection guidelines, Surf. Coatings Technol. 38 (1989) 267–280.

[31] H.O. Pierson, Fundamentals of Chemical Vapor Deposition, in: H.O.B.T.-H. of C.V.D. (CVD) (Second E. Pierson (Ed.), Handb. Chem. Vap. Depos., Elsevier, Norwich, NY, 1999.

[32] L. von Fieandt, Cutting edge titanium-based CVD hard coatings, Doctoral Thesis, Uppsala University, Sweden, 2018.

[33] M.C.V. Y. Hamedani, P. Macha, T. J. Bunning, R. R. Naik, Plasma-enhanced chemical vapor deposition: Where we are and the outlook for the future, Chem. Vap. Depos. Adv. Appl. Opt. Sol. Cells Solid State Devices, InTech. (2016).

[34] A. Kar, J. Mazumder, Laser chemical vapor deposition of thin films, Mater. Sci. Eng. B. 41 (1996) 368–373.

[35] J.-O. Carlsson, U. Jansson, Progress in chemical vapor deposition, Prog. Solid State Chem. 22 (1993) 237–292.

[36] B.E. Deal, A.S. Grove, General Relationship for the Thermal Oxidation of Silicon, J. Appl. Phys. 36 (1965) 3770–3778.

[37] Y. Song, S. Dhar, L.C. Feldman, G. Chung, J.R. Williams, Modified Deal Grove model for the thermal oxidation of silicon carbide, J. Appl. Phys. 95 (2004) 4953–4957.

[38] M. Rieutord, Fluid dynamics - An introduction, Springer International Publishing, Cham, 2015.

[39] N. Sharma, M. Hooda, S.K. Sharma, Synthesis and Characterization of LPCVD Polysilicon and Silicon Nitride Thin Films for MEMS Applications, J. Mater. 2014 (2014) 954618.

[40] K. Hochberg, D.A. Roberts, The Deposition of Silicon Oxide Films by LPCVD at Temperatures as Low as 100°C from a New Liquid Source, MRS Proc. 282 (1992) 569.

[41] C. Yang, J. Pham, Characteristic Study of Silicon Nitride Films Deposited by LPCVD and PECVD, Silicon. 10 (2018) 2561–2567.

[42] D. Stiens, T. Manns, S. Ruppi, TiAlCN layers with lamellae structure, US patent 10,214,810 B2, 2019.

[43] M. Pons, R. Boichot, N. Coudurier, A. Claudel, E. Blanquet, S. Lay, F. Mercier, D. Pique, High temperature chemical vapor deposition of aluminum nitride, growth and evaluation, Surf. Coatings Technol. 230 (2013) 111–118.

[44] L. von Fieandt, T. Larsson, E. Lindahl, O. Bäcke, M. Boman, Chemical vapor deposition of TiN on transition metal substrates, Surf. Coatings Technol. 334 (2018) 373–383.

[45] C. V Thompson, Structure Evolution During Processing of Polycrystalline Films, Annu. Rev. Mater. Sci. 30 (2000) 159–190.

[46] A. van der Drift, Evolutional selection, a principle governing growth orientation in vapour deposition layers, Philips Res. Repts. 22 (1967) 267–288.

[47] X.J. Ning, F.R. Chien, P. Pirouz, J.W. Yang, M.A. Khan, Growth defects in GaN films on sapphire: The probable origin of threading dislocations, J. Mater. Res. 11 (1996) 580–592.

[48] C. Wild, R. Kohl, N. Herres, W. Müller-Sebert, P. Koidl, Oriented CVD diamond films: twin formation, structure and morphology, Diam. Relat. Mater. 3 (1994) 373–381.

[49] M. Halvarsson, S. Vuorinen, Epitaxy in multilayer coatings of k-Al2O3, Surf. Coatings Technol. 80 (1996) 80–88.

[50] S. Canovic, S. Ruppi, J. Rohrer, A. Vojvodic, C. Ruberto, P. Hyldgaard, M. Halvarsson, TEM and DFT investigation of CVD TiN/κ–Al2O3 multilayer coatings, Surf. Coatings Technol. 202 (2007) 522–531.

[51] P. Smereka, X. Li, G. Russo, D.J. Srolovitz, Simulation of faceted film growth in three dimensions: microstructure, morphology and texture, Acta Mater. 53 (2005) 1191–1204.

[52] C. Wild, N. Herres, P. Koidl, Texture formation in polycrystalline diamond films, J. Appl. Phys. 68 (1990) 973–978.

[53] A. Sherman, Growth and properties of LPCVD titanium nitride as a diffusion barrier for silicon device technology, J. Electrochem. Soc. 137 (1990) 1892/1897.

[54] H. Holleck, Material selection for hard coatings, J. Vac. Sci. Technol. A. 4 (1986) 2661–2669.

[55] S. Schiller, G. Beister, J. Reschke, G. Hoetzsch, TiN hard coatings deposited on high-speed steel substrates by reactive direct current magnetron sputtering, J. Vac. Sci. Technol. A Vacuum, Surfaces, Film. 5 (1987) 2180–2183.

[56] M. Griepentrog, B. Mackrodt, G. Mark, T. Linz, Properties of TiN hard coatings prepared by unbalanced magnetron sputtering and cathodic arc deposition using a uni- and bipolar pulsed bias voltage, Surf. Coatings Technol. 74–75 (1995) 326–332.

[57] L. von Fieandt, T. Larsson, E. Lindahl, O. Bäcke, M. Boman, Chemical vapor deposition of TiN on transition metal substrates, Surf. Coatings Technol. 334 (2018) 373–383.

[58] H. Jeon, J.-H. Koo, J.-W. Lee, Y.-S. Kim, K.M. Kang, Y. Do Kim, Y. Do Kim, Atomic layer deposition of TiN on Si (100) and (111) Substrates, MRS Proc. 616 (2000) 211.

[59] H. Vollstädt, E. Ito, M. Akaishi, S. Akimoto, O. Fukunaga, High pressure synthesis of rocksalt type of AlN, Proc. Japan Acad. Ser. B Phys. Biol. Sci. 66 (1990) 7–9.

[60] A.R. Denton, N.W. Ashcroft, Vegard's law, Phys. Rev. A. 43 (1991) 3161–3164.

[61] I. Endler, M. Höhn, M. Herrmann, R. Pitonak, S. Ruppi, M. Schneider, H. van den Berg, H. Westphal, Novel aluminum-rich $Ti_{1-x}Al_xN$ coatings by LPCVD, Surf. Coatings Technol. 203 (2008) 530–533.

[62] K.M. Calamba, Phase stability and defect structures in (Ti,Al)N hard coatings, Linköping University, 2019.

[63] N. Shulumba, O. Hellman, Z. Raza, B. Alling, J. Barrirero, F. Mücklich, I.A. Abrikosov, M. Odén, Lattice vibrations change the solid solubility of an alloy at high temperatures, Phys. Rev. Lett. 117 (2016) 205502.

[64] B. Alling, A. V Ruban, A. Karimi, O.E. Peil, S.I. Simak, L. Hultman, I.A. Abrikosov, Mixing and decomposition thermodynamics of $Ti_{1-x}Al_xN$ from first-principles calculations, Phys. Rev. B. 75 (2007) 45123.

[65] I.A. Abrikosov, A. Knutsson, B. Alling, F. Tasnádi, H. Lind, L. Hultman, M. Odén, Phase stability and elasticity of TiAlN, Mater. . 4 (2011).

[66] A. Knutsson, M.P. Johansson, L. Karlsson, M. Odén, Thermally enhanced mechanical properties of arc evaporated $Ti_{0.34}Al_{0.66}N$/TiN multilayer coatings, J. Appl. Phys. 108 (2010) 44312.

[67] A. Hörling, L. Hultman, M. Odén, J. Sjölén, L. Karlsson, Thermal stability of arc evaporated high aluminum-content $Ti_{1-x}Al_xN$ thin films, J. Vac. Sci. Technol. A. 20 (2002) 1815–1823.

[68] A. Hörling, L. Hultman, M. Odén, J. Sjölén, L. Karlsson, Mechanical properties and machining performance of $Ti_{1-x}Al_xN$-coated cutting tools, Surf. Coatings Technol. 191 (2005) 384–392.

[69] P.H. Mayrhofer, A. Hörling, L. Karlsson, J. Sjölén, T. Larsson, C. Mitterer, L. Hultman, Self-organized nanostructures in the Ti–Al–N system, Appl. Phys. Lett. 83 (2003) 2049–2051.

[70] A. Kimura, H. Hasegawa, K. Yamada, T. Suzuki, Metastable $Ti_{1-x}Al_xN$ films with different Al content, J. Mater. Sci. Lett. 19 (2000) 601–602.

[71] M. Zhou, Y. Makino, M. Nose, K. Nogi, Phase transition and properties of Ti–Al–N thin films prepared by r.f.-plasma assisted magnetron sputtering, Thin Solid Films. 339 (1999) 203–208.

[72] J. Todt, J. Zalesak, R. Daniel, R. Pitonak, A. Köpf, R. Weißenbacher, B. Sartory, C. Mitterer, J. Keckes, Al-rich cubic $Al_{0.8}Ti_{0.2}N$ coating with self-organized nano-lamellar microstructure: Thermal and mechanical properties, Surf. Coatings Technol. 291 (2016) 89–93.

[73] Q. Guo, A. Yoshida, Temperature dependence of band gap change in InN and AlN, Jpn. J. Appl. Phys. 33 (1994) 2453–2456.

[74] D.W. Palmer, 4.12 - Electronic energy levels in group-III nitrides, in: P. Bhattacharya, R. Fornari, H.B.T.-C.S.S. and T. Kamimura (Eds.), Elsevier, Amsterdam, 2011: pp. 390–447.

[75] A. Elshabini, F. Barlow, Semiconductor packages, in: Encycl. Mater. Sci. Technol., Second Edi, Elsevier, Amsterdam, 2001: pp. 8339–8356.

[76] U. Wahlström, L. Hultman, J.E. Sundgren, F. Adibi, I. Petrov, J.E. Greene, Crystal growth and microstructure of polycrystalline $Ti_{1-x}Al_xN$ alloy films deposited by ultra-high-vacuum dual-target magnetron sputtering, Thin Solid Films. 235 (1993) 62–70.

[77] B.D. Ozsdolay, C.P. Mulligan, K. Balasubramanian, L. Huang, S. V Khare, D. Gall, Cubic β-$WN_x$ layers: Growth and properties vs N-to-W ratio, Surf. Coatings Technol. 304 (2016) 98–107.

[78] O. Knotek, F. Löftier, A. Barimani, Interface stabilization of W-N coatings by chromium alloying, MRS Proc. 237 (1991) 673.

[79] S. Wang, X. Yu, Z. Lin, R. Zhang, D. He, J. Qin, J. Zhu, J. Han, L. Wang, H. Mao, J. Zhang, Y. Zhao, Synthesis, crystal structure, and elastic properties of novel tungsten nitrides, Chem. Mater. 24 (2012) 3023–3028.

[80] L.E. Toth, Transition metal carbides and nitrides, Academic Press, New Yourk and London, 1971.

[81] N. Schonberg, Contributions to the knowledge of the molybdenum–nitrogen and the tungsten–nitrogen systems, Acta Chem. Scand. 8 (1954) 1947–1999.

[82] M.L. Addonizio, A. Castaldo, A. Antonaia, E. Gambale, L. Iemmo, Influence of process parameters on properties of reactively sputtered tungsten nitride thin films, J. Vac. Sci. Technol. A. 30 (2012) 31506.

[83] M. Wen, Q.N. Meng, W.X. Yu, W.T. Zheng, S.X. Mao, M.J. Hua, Growth, stress and hardness of reactively sputtered tungsten nitride thin films, Surf. Coatings Technol. 205 (2010) 1953–1961.

[84] O.J. Bchir, S.W. Johnston, A.C. Cuadra, T.J. Anderson, C.G. Ortiz, B.C. Brooks, D.H. Powell, L. McElwee-White, MOCVD of tungsten nitride ($WN_x$) thin films from the imido complex $Cl_4(CH_3CN)W(NiPr)$, J. Cryst. Growth. 249 (2003) 262–274.

[85] C.C. Baker, S.I. Shah, Reactive sputter deposition of tungsten nitride thin films, J. Vac. Sci. Technol. A. 20 (2002) 1699–1703.

[86] M.J. Mehl, D. Finkenstadt, C. Dane, G.L.W. Hart, S. Curtarolo, Finding the stable structures of $N_{1-x}W_x$ with an ab initio high-throughput approach, Phys. Rev. B. 91 (2015) 184110.

[87] M. Vaidya, K. Guruvidyathri, B.S. Murty, Phase formation and thermal stability of CoCrFeNi and CoCrFeMnNi equiatomic high entropy alloys, J. Alloys Compd. 774 (2019) 856–864.

[88] Z. Wu, H. Bei, F. Otto, G.M. Pharr, E.P. George, Recovery, recrystallization, grain growth and phase stability of a family of FCC-structured multi-component equiatomic solid solution alloys, Intermetallics. 46 (2014) 131–140.

[89] T. Nakajima, K. Watanabe, N. Watanabe, Preparation of tungsten nitride film by CVD method using $WF_6$, J. Electrochem. Soc. 134 (1987) 3175.

[90] Introduction to X-ray powder diffractometry, John Wiley & Sons, Inc., Hoboken, NJ, USA, 2012.

[91] H.-R. Wenk, P. Van Houtte, Texture and anisotropy, Reports Prog. Phys. 67 (2004) 1367–1428.

[92] Y. Homma, S. Suzuki, Y. Kobayashi, M. Nagase, D. Takagi, Mechanism of bright selective imaging of single-walled carbon nanotubes on insulators by scanning electron microscopy, Appl. Phys. Lett. 84 (2004) 1750–1752.

[93] D.B. Williams, C.B. Carter, Transmission electron microscopy: A textbook for materials science, in: D.B. Williams, C.B. Carter (Eds.), Springer US, Boston, MA, 2009.

[94] R.A. Schwarzer, D.P. Field, B.L. Adams, M. Kumar, A.J. Schwartz, Present state of electron backscatter diffraction and prospective developments, in: Electron backscatter diffraction in materials science, Springer US, Boston, MA, 2009.

[95] N. Mortazavi, Novel insights into the oxidation of high temperature alloys - the role of environment, microstructure and reactive elements, doctoral thesis, Chalmers University of Technology, 2017.

[96] R.R. Keller, R.H. Geiss, Transmission EBSD from 10 nm domains in a scanning electron microscope, J. Microsc. 245 (2012) 245–251.

[97] F. Bachmann, R. Hielscher, H. Schaeben, Texture Analysis with MTEX – Free and Open Source Software Toolbox, Solid State Phenom. 160 (2010) 63–68.

[98]   F.A. Stevie, L.A. Giannuzzi, B.I. Prenitzer, The focused ion beam instrument, in: L.A. Giannuzzi, F.A. Stevie (Eds.), Introd. to Focus. Ion Beams, Springer US, Boston, MA, 2005: pp. 1–12.

[99]   D. Tomus, H.P. Ng, In situ lift-out dedicated techniques using FIB–SEM system for TEM specimen preparation, Micron. 44 (2013) 115–119.

[100]  M. Schaffer, B. Schaffer, Q. Ramasse, Sample preparation for atomic-resolution STEM at low voltages by FIB, Ultramicroscopy. 114 (2012) 62–71.

[101]  R. Erni, Aberration-corrected imaging in transmission electron microscopy - An introduction, World Scientific Publishing, Singapore, 2015.

[102]  R.F. Egerton, Electron energy-loss spectroscopy in the TEM, Reports Prog. Phys. 72 (2009) 16502.

[103]  H. Inada, L. Wu, J. Wall, D. Su, Y. Zhu, Performance and image analysis of the aberration-corrected Hitachi HD-2700C STEM, Microscopy. 58 (2009) 111–122.

[104]  P. Hartel, H. Rose, C. Dinges, Conditions and reasons for incoherent imaging in STEM, Ultramicroscopy. 63 (1996) 93–114.

[105]  B. Gault, A.J. Breen, Y. Chang, J. He, E.A. Jägle, P. Kontis, P. Kürnsteiner, A. Kwiatkowski da Silva, S.K. Makineni, I. Mouton, Z. Peng, D. Ponge, T. Schwarz, L.T. Stephenson, A. Szczepaniak, H. Zhao, D. Raabe, Interfaces and defect composition at the near-atomic scale through atom probe tomography investigations, J. Mater. Res. 33 (2018) 4018–4030.

[106]  A. Sobachkin, G. Dumnov, Numerical basis of CAD-embedded CFD, in: Proc. NAFEMS World Congr., 2013.

[107]  G. Velo, A.S. Wightman, Rigorous atomic and molecular physics, US, Springer, Boston, MA, 1981.

[108]  V. Sahni, Quantal density functional theory, Springer Berlin Heidelberg, Berlin, Heidelberg, 2004.

[109]  G. Kresse, J. Furthmüller, Efficient iterative schemes for ab initio total-energy calculations using a plane-wave basis set, Phys. Rev. B. 54 (1996) 11169–11186.

[110]  H. Lukas, S.G. Fries, B. Sundman, Computational thermodynamics: The Calphad method, Cambridge University Press, Cambridge, 2007.

[111]  J.-O. Andersson, T. Helander, L. Höglund, P. Shi, B. Sundman, Thermo-Calc & DICTRA, computational tools for materials science, Calphad. 26 (2002) 273–312.

[112]  J.W. Matthews, J.L. Crawford, Accomodation of misfit between single-crystal films of nickel and copper, Thin Solid Films. 5 (1970) 187–198.

[113] L. Morresi, Basics of Molecular Beam Epitaxy (MBE) technique, Bentham Science Publishers, Sharjah, 2013.

[114] J.H. van der Merwe, J. Woltersdorf, W.A. Jesser, Low energy dislocation structures in epitaxy, Mater. Sci. Eng. 81 (1986) 1–33.

[115] J.W. Matthews, A.E. Blakeslee, Defects in epitaxial multilayers: I. Misfit dislocations, J. Cryst. Growth. 27 (1974) 118–125.

[116] E.R. Thompson, K.R. Lawless, Observation of interfacial dislocations in thin (100) and (111) electrodeposits of nickel on copper, Appl. Phys. Lett. 9 (1966) 138–140.

[117] C.A.B. Ball, On bonding and structure of epitaxial bicrystals. II. Thin films, Phys. Status Solidi. 42 (1970) 357–368.

[118] W.A. Jesser, D. Kuhlmann-Wilsdorf, On the theory of interfacial energy and elastic strain of epitaxial overgrowths in parallel alignment on single crystal Substrates, Phys. Status Solidi. 19 (1967) 95–105.

[119] L.B. Freund, Dislocation mechanisms of relaxation in strained epitaxial films, MRS Bull. 17 (1992) 52–60.

[120] H. Brune, H. Röder, C. Boragno, K. Kern, Strain relief at hexagonal-close-packed interfaces, Phys. Rev. B. 49 (1994) 2997–3000.

[121] C. Günther, J. Vrijmoeth, R.Q. Hwang, R.J. Behm, Strain relaxation in hexagonally close-packed metal-metal interfaces, Phys. Rev. Lett. 74 (1995) 754–757.

[122] J.A. Meyer, P. Schmid, R.J. Behm, Effect of layer-dependent adatom mobilities in heteroepitaxial metal film growth: Ni/Ru(0001), Phys. Rev. Lett. 74 (1995) 3864–3867.

[123] V. Fournée, J. Ledieu, T. Cai, P.A. Thiel, Influence of strain in Ag on Al(111) and Al on Ag(100) thin film growth, Phys. Rev. B. 67 (2003) 155401.

[124] W. Qian, M. Skowronski, R. Kaspi, Dislocation density reduction in GaSb films grown on GaAs substrates by molecular beam epitaxy, J. Electrochem. Soc. 144 (1997) 1430–1434.

[125] A. Mogilatenko, A. Knauer, U. Zeimer, C. Netzel, J. Jeschke, R.-S. Unger, C. Hartmann, J. Wollweber, A. Dittmar, U. Juda, M. Weyers, M. Bickermann, Crystal defect analysis in AlN layers grown by MOVPE on bulk AlN, J. Cryst. Growth. 505 (2019) 69–73.

[126] V. Narayanan, K. Lorenz, W. Kim, S. Mahajan, Gallium nitride epitaxy on (0001) sapphire, Philos. Mag. A. 82 (2002) 885–912.

[127] F.Y. Meng, I. Han, H. McFelea, E. Lindow, R. Bertram, C. Werkhoven, C. Arena, S. Mahajan, Direct observation of formation of threading dislocations from stacking faults in GaN layer grown on (0001) sapphire, Scr. Mater. 64 (2011) 93–96.

[128] F.Y. Meng, I. Han, H. McFelea, E. Lindow, R. Bertram, C. Werkhoven, C. Arena, S. Mahajan, Sapphire surface pits as sources of threading dislocations in hetero-epitaxial GaN layers, Scr. Mater. 65 (2011) 257–260.

[129] W.K. Burton, N. Cabrera, F.C. Frank, N.F. Mott, The growth of crystals and the equilibrium structure of their surfaces, Philos. Trans. R. Soc. London. Ser. A, Math. Phys. Sci. 243 (1951) 299–358.

[130] F. Meng, S.A. Morin, S. Jin, Growth of nanomaterials by screw dislocation, Springer handbook of nanomaterials, Springer, Berlin, Heidelberg, 2013: pp. 639–664.

[131] F. Meng, S.A. Morin, A. Forticaux, S. Jin, Screw dislocation driven growth of nanomaterials, Acc. Chem. Res. 46 (2013) 1616–1626.

[132] M.J. Shearer, L. Samad, Y. Zhang, Y. Zhao, A. Puretzky, K.W. Eliceiri, J.C. Wright, R.J. Hamers, S. Jin, Complex and noncentrosymmetric stacking of layered metal dichalcogenide materials created by screw dislocations, J. Am. Chem. Soc. 139 (2017) 3496–3504.

[133] E. Rahimi, A. Davoodi, A.R. Kiani Rashid, Characterization of screw dislocation-driven growth in nickel micro-nanostructure electrodeposition process by AFM, Mater. Lett. 210 (2018) 341–344.

[134] I. V Markov, Crystal growth for beginners, World Scientific, 2003.

[135] F.C. Frank, Crystal growth and dislocations, Adv. Phys. 1 (1952) 91–109.

[136] A. Forslund, A. Ruban, Surface energetics of $Al_xTi_{1-x}N$ alloys, Comput. Mater. Sci. 183 (2020) 109813.

[137] B. Gault, M.P. Moody, J.M. Cairney, S.P. Ringer, Atom probe microscopy, Springer, New York, NY, 2012.

[138] H.B. Huntington, J.E. Dickey, R. Thomson, Dislocation energies in NaCl, Phys. Rev. 100 (1955) 1117–1128.